Publications

Publication I

Gomez, V., Hernando, M., Aguado, E., Sanz, R., Rossi, C., *"ROBOMINER: Development of a Highly Configurable and Modular Scaled-Down Prototype of a Mining Robot.,"* Machines. 2023, 11, 809. doi:10.3390/machines11080809

machines

Article

ROBOMINER: Development of a Highly Configurable and Modular Scaled-Down Prototype of a Mining Robot

Virgilio Gomez [1,*], Miguel Hernando [1], Esther Aguado [1,2], Ricardo Sanz [2] and Claudio Rossi [1]

[1] Centre for Automation and Robotics, Universidad Politécnica de Madrid-CSIC, 28006 Madrid, Spain; miguel.hernando@upm.es (M.H.); e.aguado@upm.es (E.A.); claudio.rossi@upm.es (C.R.)
[2] Autonomous Systems Laboratory, Universidad Politécnica de Madrid, 28006 Madrid, Spain; ricardo.sanz@upm.es
* Correspondence: virgilio.gomez.lambo@upm.es

Abstract: Historically, mining operations have faced numerous challenges, including safety hazards, inefficiencies, and environmental concerns. However, recent advances in robotics, automation, and artificial intelligence have presented opportunities for the mining industry. The ROBOMINERS project, a Horizon 2020 European Union initiative, aims to revolutionize the mining ecosystem by implementing disruptive robotic concepts. One such concept is resilience, which involves enabling mining robots to reconfigure morphologically during operation. This article presents the development of a modular robotic system that focuses on modularity and self-assembly to provide insight into developing a highly adaptable and compact solution for future mining robots. The robotic system is composed of a set of highly configurable modular robotic platforms that can be reconfigured with other robotic modules or submodules to form more complex systems to perform different tasks. Several module configurations are presented, and different locomotion experiments were carried out to test the ability of the modules to navigate unstructured environments. The modules exhibited great maneuverability in unstructured terrain and demonstrated self-assembly and reconfiguration capabilities during operation. This is a foundational step towards the long-term goal of developing compact autonomous agents capable of self-assembly and mining task execution.

Keywords: modular robots; reconfigurable robots; robotic systems; mining robots

Citation: Gomez, V.; Hernando, M.; Aguado, E.; Sanz, R.; Rossi, C. ROBOMINER: Development of a Highly Configurable and Modular Scaled-Down Prototype of a Mining Robot. *Machines* **2023**, *11*, 809. https://doi.org/10.3390/machines11080809

Academic Editor: Dan Zhang

Received: 6 July 2023
Revised: 4 August 2023
Accepted: 5 August 2023
Published: 7 August 2023

1. Introduction

Mining operations are crucial for meeting growing global demand for natural resources. However, traditional industry mining methods in are often associated with significant challenges, such as safety hazards, inefficiencies, and environmental concerns [1]. In recent years, remarkable progress [2–5] has emerged in robotics, automation, and artificial intelligence that offer the potential to address these challenges and unlock new possibilities. While these advances have shown considerable potential, there is still room for improvement in adaptability, scalability, and overall performance. One approach with great potential is the implementation of modular robotic systems [6]. Consisting of individual robot modules that can be interconnected and reconfigured, these systems provide inherent flexibility and versatility to allow robots to adapt to changing conditions, perform complex tasks, and achieve different goals.

The ROBOMINERS project (https://robominers.eu), [Accessed date 6 July 2023] funded under the European Union's Horizon 2020 research and innovation program, is strategically focused on introducing disruptive robotic concepts to facilitate access to minerals in Europe, thereby shaping a new mining ecosystem. Among its key aspects is resilience, which entails providing mining robots with the ability to complete tasks when new situations or disturbances arise. One of the main objectives of the project is to provide resilience towards autonomous operation, where robotic modules are sent down in pieces to the mine through a large diameter borehole and self-assembled to form a fully functional mining robot that can be reconfigured during operation to cope with failures or adapt to different scenarios. For instance, Figure 1 shows a situation where robotic modules perform this function during a mining task: the robot changes its cutting head according to the material it is extracting, attaches special sensing devices, and connects several modules to increase its strength or replaces failed modules with new ones. This adaptability allows on-the-job reconfiguration.

The concepts of reconfiguration, self-assembly, and self-repair have been extensively explored in recent years with several works [7–10] compiling the most relevant developments. Within the broad spectrum of reconfigurable modular robots, this study focuses on reconfigurable, mobile platforms that can operate in rough environments. These platforms interact with the environment independently and can generate larger and more complex robotic systems by connecting several modules through various docking mechanisms. In this group, we found platforms like Milibot [11]: a set of semi-autonomous, tracked mobile platforms is arranged into a train configuration to cross relatively large obstacles. The platforms are equipped with a set of coupler pins that allow the modules to engage and disengage under computer control. Another remarkable development is the S-bots [12–14] system: autonomous, tracked-and-wheeled, reconfigurable mobile robots. The reconfiguration is achieved either by a robotic gripper or a manipulator arm integrated into the structure of the robot to allows for rigid and semi-flexible connections. The rigid gripper permits the lifting of another module while the arm allows for flexible connections where the modules retain relative freedom of movement with respect to each other. Other examples include the modular JL-I,2 platforms [15,16]. In this case, the first version of the system was composed of a series of tracked mobile robots equipped with a cone-shaped connector and a parallel manipulator that resulted in an active spherical joint that allowed the modules to rotate in three dimensions. Therefore, different 3D configurations can be achieved. For the second version, the docking interface was modified to include a gripper, allowing the modules to achieve basic manipulation as well as locomotion. Additional developments like AMOEBA-I and the different versions of the platform [17] present a reconfigurable, modular, tracked robot structure capable of docking from all sides, and generating chain, triangular and row formations depending on the specific terrain condition. The docking interface is based on a set of links that connect to other tracks and can change position and orientation with respect to the central structure.

Previous research efforts have indeed made significant progress, but certain limitations persist concerning the configurability and adaptability of self-assembly systems, particularly in unstructured environments. Commonly used docking mechanisms, such as latches, mechanical links, and rigid grippers face vulnerabilities when confronted with uneven terrain, limited visibility, and unpredictable objects.

To address these challenges and align with the project’s long-term vision, this study introduced a versatile and configurable modular robotic system with a novel docking mechanism. The system comprises robotic modules capable of self-assembly and reconfiguration during operation, along with manually assembled and self-assembled submodules that extend the resulting robotic systems’ functionalities. A significant innovation is the seamless integration of a compact, soft robotic arm into the robot structure. Unlike other reconfigurable platforms, our arm remains protected within the robot when not used. Additionally, integrating soft arms as coupling mechanisms enhances adaptability and performance during docking maneuvers, especially in unstructured environments. The soft robotic arm operates like a car crane during docking or undocking, effortlessly guiding itself to another module or submodule’s docking port, securing it in place, and then retracting to complete the process.

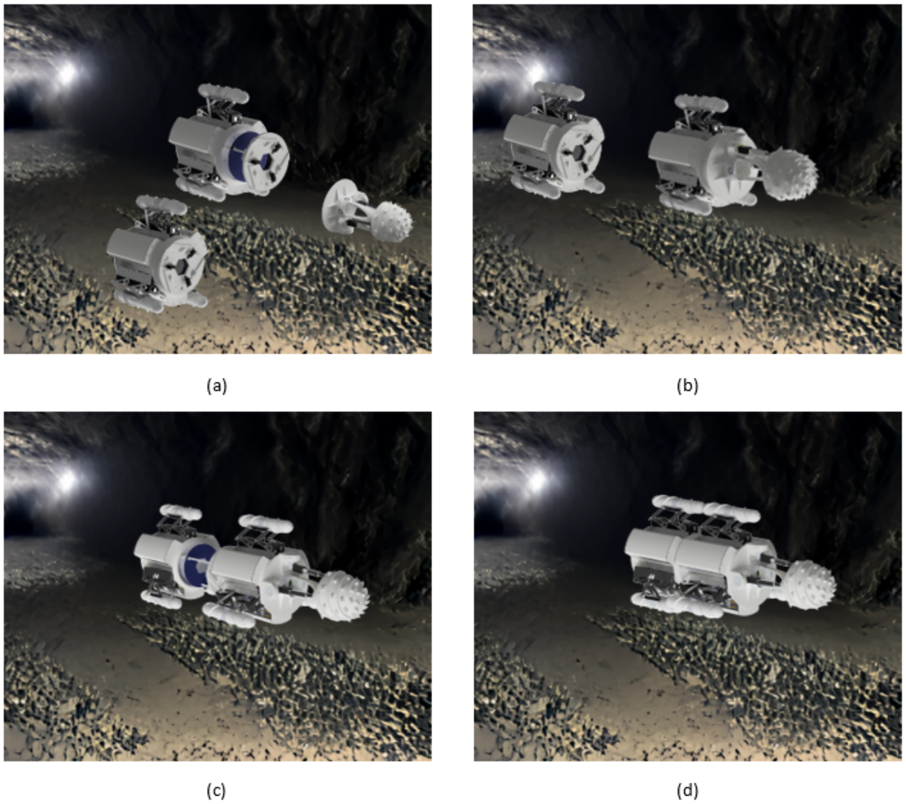

Figure 1. Concept of a set of highly configurable modular robotic miners that work together to perform a complex task. (**a**) Modular prototypes and tools are deployed in the mine environment. (**b**) The first robotic module assembles a cutting head on its front. (**c**) The second module is at the back of the first module and begins to assemble to create a larger robotic structure. (**d**) Finally, the resulting structure, made up of two modular robots and a robotic submodule, is assembled to perform a complex task: mining.

The article is organized as follows. Section 2 provides a description of the modular robot platform with all the possible locomotion submodules as well as an integrated arm that acts as a coupling interface. In Section 3, we introduce different submodules that can be coupled to the modular robot to perform several tasks. Section 4 solves the kinematics of the robotic platform and the singularities, and presents a workspace analysis for the leg mechanism. In Section 5, we show different configurations of the robotic platform and carry out several locomotion tests and module reconfiguration to demonstrate the functionality of the elements that make up the robotic system. Finally, Section 6 provides the conclusions and summarizes future developments.

2. Robotic Module Description

The presented robotic system is based on highly configurable modules capable of self-assembly and reconfiguration during operation. In our context, the term ”robotic modules” refers to mobile platforms that can operate independently, while submodules are considered add-ons that can be attached to the module to perform a specific task. The concept of self-assembly is the robot’s ability to form larger structures by connecting different modules or submodules during an operation without the need of human intervention. The concept of self-reconfigurability is related to the ability of the robot to reconfigure its control system automatically as larger structures are formed, i.e., introducing new capabilities into the system as modules or submodules are connected.

The main component of the system consists of robotic modules that are composed of a main structure with three compartments and three docking ports, as presented in Figure 2. Electronic components, batteries, and other actuation systems are located in the compartments and in the robot's internal structure. Interchangeable end effectors or additional sensors are assembled in docking ports depending on the task to be performed. To form larger and more complex structures, the module is equipped with a coupling mechanism based on a soft continuum arm with a mechanical coupling interface where the arm is integrated into the structure of the robot.

Modules can be powered by either an external power source or a 3S battery that can be installed in the robot. Inside the module, a power board made up of a set of voltage converters (12, 6, 5) is used to power the robot's different electronic components and motors. A 12 V line is used to supply energy to both the locomotion submodules' motors and the legs' servomotors. The 6 V powers the robot coupling mechanism, and the 5 V supplies energy to different sensors and microcontrollers. The technical specifications of the robot module are presented in Table 1.

The design of the robot module is inspired by a mine-ready robotic system developed within the framework of the project, where each mining robot module is 1.5 m long, approximately 1 m in diameter, and weighs approximately 500 kg. The robot module presented here serves as a scaled-down version of the larger mine-ready robotic system and its primary purpose is to study the concepts of modularity, self-assembly, and reconfiguration during operation to provide insight into different configuration possibilities and emphasizing the importance of adaptability and versatility.

Table 1. Technical specifications of robotic modules.

Specifications	Values	
Power	12–15 V, 300 W (max)	Battery: 3S 2200 mAh 70C
Computing	QTPy-SAMD21—locomotion submodules and robot submodules ESP32-DevKitC V4—Main Board	
Communication	I2C,TTL—internal UART—module intercommunication WiFi/Bluetooth—external	
Sensors	Motor Current (INA 219) Battery Status (MCP3424, INA219) IMU 9-DoF (BNO055) Magnetic Encoders Dynamixel sensors (temp, volt, current, encoder)	
Actuators	DC Motors—Locomotion Submodules and Coupling mechanism Dynamixel Servomotors (XM430-W350-T)—Robot Legs Dynamixel Servomotors (XL330-M288-T)—Coupling Mechanism	
Mass	3.90 kg (module with 3 legs)	0.8 kg (robot structure)
Dimensions	Length: 22 cm	Diameter: 30–40 cm

The connection of the robot components and the communication protocols used are shown in Figure 3, where each component is classified according to its location and functionality. To communicate the different components of the robot, the following protocols were defined:

- Two low-level I2C-based protocols with a cyclic redundancy check (CRC) were implemented. The first I2C protocol communicated both the ESP32 and QtPy boards, as well as the different sensors of the robot. The second one collected sensor data from the locomotion submodule, maintaining the needed modularity to easily change the locomotion submodules.

- One half-duplex universal asynchronous receiver–transmitter (UART) (TTL daisy-chained bus) using the manufacture's protocol Dynamixel protocol 2.0 was used to enable the ESP32 to communicate with the leg-and-coupling mechanism servomotors.
- One custom UART protocol was implemented to communicate with other robotic modules or submodules when they were attached via the robot coupling mechanism.
- A transparent wireless protocol using WiFi or Bluetooth to link the ESP32 to the central control unit (CCU).

To monitor the state of the different modules and to teleoperate the system, a graphical user interface (GUI) based on Qt (Figure 4) was designed. The GUI was organized in a set of windows and tabs where the information of the robot components was presented in a comprehensive manner. Every time a robot established a connection with the CCU, a new tab appeared in the main window of the GUI, allowing the user to decide which robot module to monitor or teleoperate.

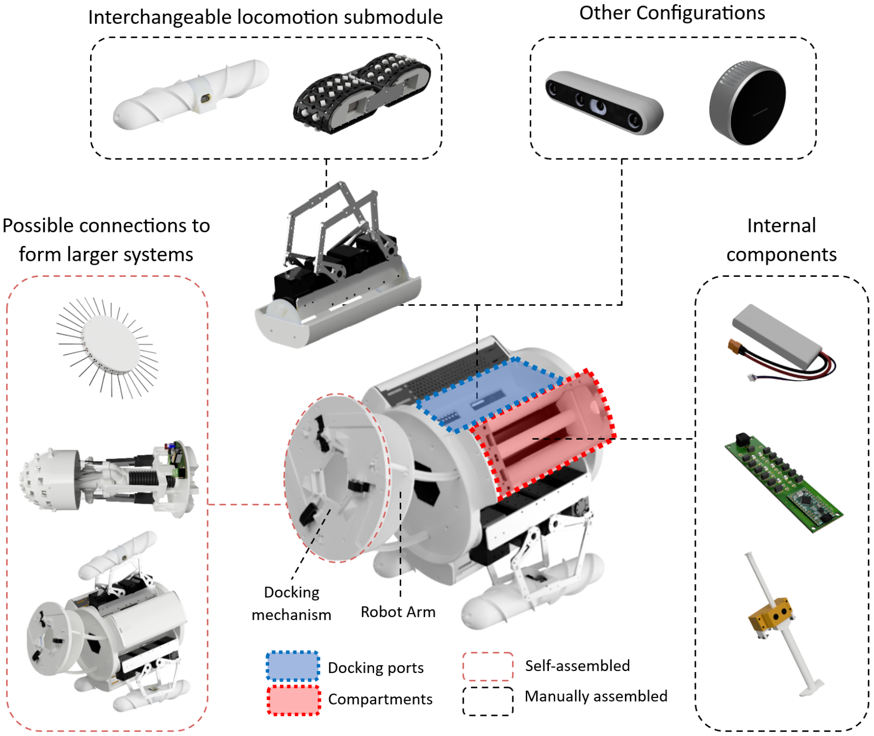

Figure 2. Robotic module description. Each robotic module comprises three compartments and three docking ports. The docking ports serve the purpose of configuring diverse locomotion submodules or additional sensors like cameras or LiDAR. Within the compartments, various internal components are housed. The robot arm allows the autonomous coupling of different modules and robotic submodules to form more complex systems.

2.1. Locomotion Submodules

To provide the modules with the ability to navigate in unstructured environments, different locomotion submodules were developed. These were easily interchangeable due to a standard mounting interface, and each had a different operation principle.

2.1.1. Archimedean Screw

The Archimedean screw locomotion submodule consists of a set of two helical screw-like structures that are strategically designed with interlocking threads, providing a continuous surface for propulsion. When activated, the screw rotates, causing the helical threads to grip the terrain or the surrounding medium. By generating rotational motion, the screw threads created forward or backward movement, propelling the robot through its environment [18]. To achieve omnidirectionality, two screw submodules were arranged in a mirror configuration, as shown in Figure 5.

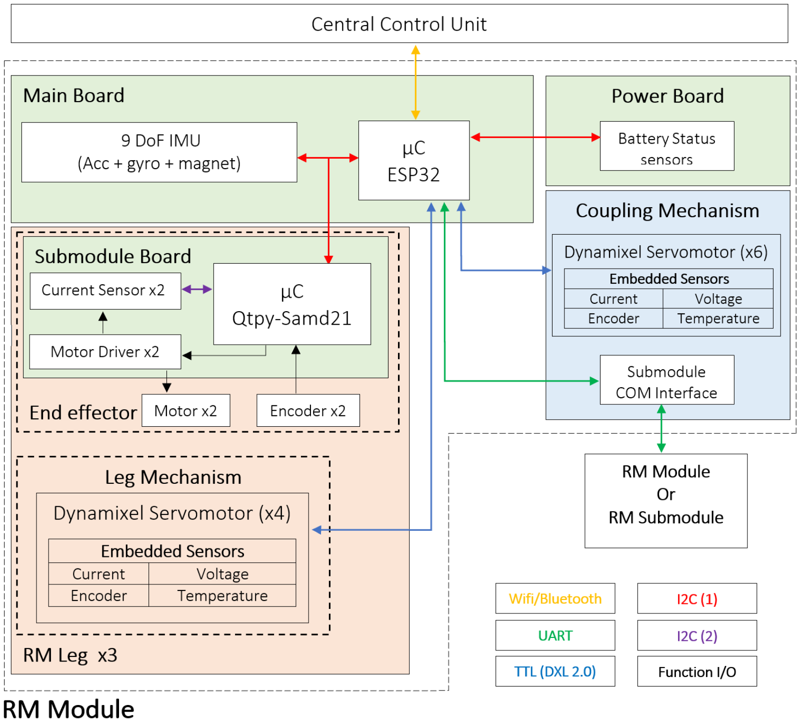

Figure 3. ROBOMINER communication protocol diagram. The green squares represent the PCB boards of the robotic module. The different colored arrows show the different protocols implemented for both intra- and intercommunication.

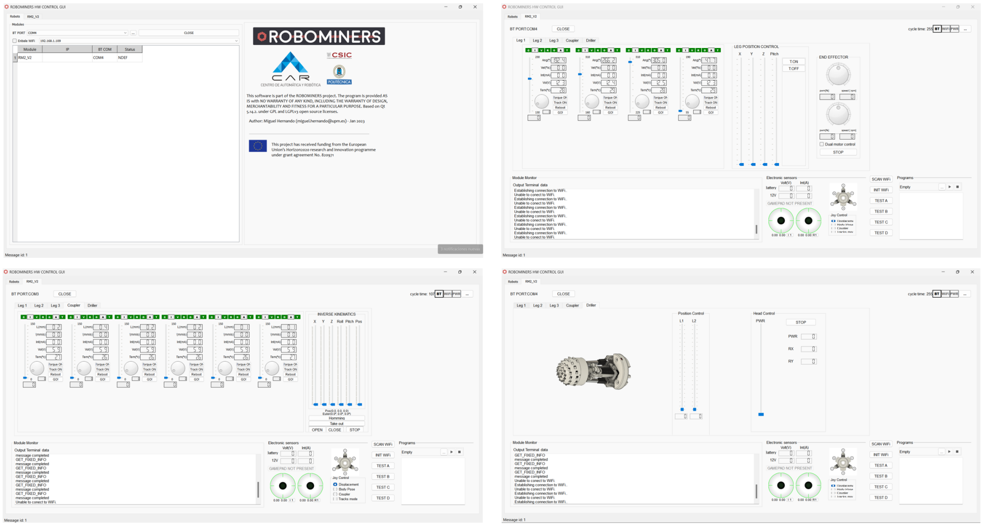

Figure 4. ROBOMINER Qt GUI. The interface is composed of a set of windows and tabs that present information regarding battery status (if connected), Dynamixel sensors, WiFi/Bluetooth connectivity, input, and output messages for debugging purposes, as well as teleoperation and robot configuration features.

One of the key advantages of this submodule is its adaptability to different surfaces and terrains [19]. The Archimedean screw mechanism excels in environments such as loose soil, sandy terrain, or even under water where conventional wheels or legs may struggle to maintain traction. The continuous contact of the screw threads with the ground enables effective propulsion and minimizes slippage, enhancing the robot's mobility. Furthermore, it offers inherent resistance to obstacles encountered during navigation. The screw's helical structure allows it to navigate over small barriers, debris, or uneven terrain, reducing the risk of getting stuck or immobilized.

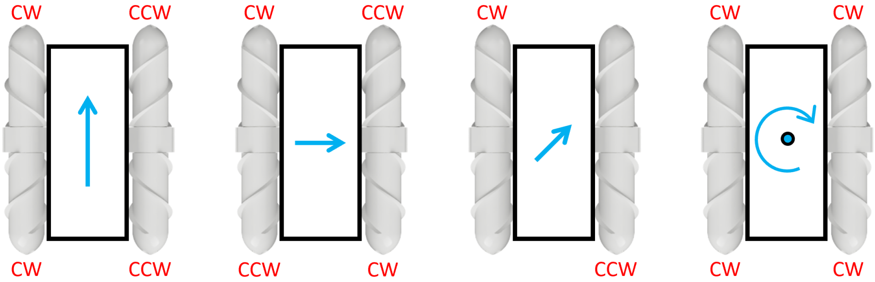

Figure 5. Motor sense combinations to achieve omnidirectional motion for the Archimedean screw locomotion submodule (CW ≡ clockwise rotation, CCW ≡ counter-clockwise rotation).

2.1.2. Omnidirectional Continuous Track

The continuous track locomotion submodule consisted of a continuous track loop made of flexible 3D-printed material with a set of passive urethane wheels embedded in the track loop oriented at a 45° angle with respect to the vertical line. The track loop was carefully designed to ensure great traction, durability, and flexibility, allowing it to conform to the terrain and maintain constant contact for optimal propulsion.

The submodule was composed of two independently actuated omnidirectional tracks with the passive wheels oriented in opposite directions. When activated, the locomotion submodule propelled the robot by rotating the continuous track loop. The robot achieved omnidirectional movement with two submodules in a mirror configuration (Figure 6) by selectively controlling different sections of the track loops.

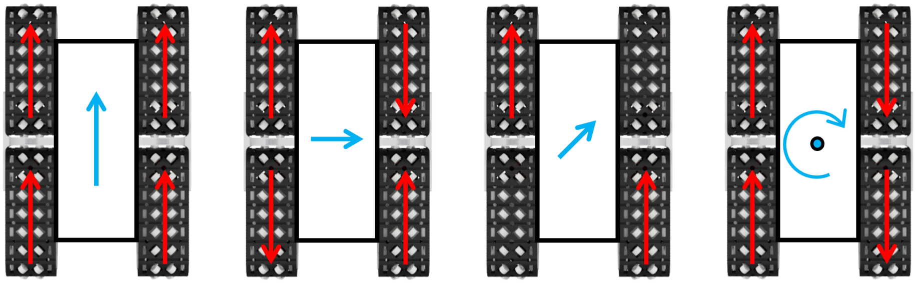

Figure 6. Motor sense combinations to achieve omnidirectional motion for the continuous track locomotion submodule.

2.2. Robot Arm

The robot arm consisted of a soft continuum arm with a mechanical interface embedded at the tip of the arm that acts as a module/submodule coupling interface. The arm was integrated into the module structure and used as a mechanical interface to join two robotic modules or submodules to create more robust or complex systems to perform different tasks. The prototype, presented in Figure 7 was composed of two sections with a set of flexible racks and rigid disks where the endpoints of the rack were attached. The movement of each section was based on the displacement of the racks following the rack and pinion mechanism [20], which gave the arm a high mass-pulling force ability. The extension, retraction, and bending of the racks resulted in the control of three degrees of freedom (DoFs) per section: two for bending and one for extension. Therefore, having two sections, we obtained the final configuration of the arm that gave 5 DoFs for the arm tip position (x, y, z) and orientation (pitch, roll) and an additional DoF to control the bending inflection point.

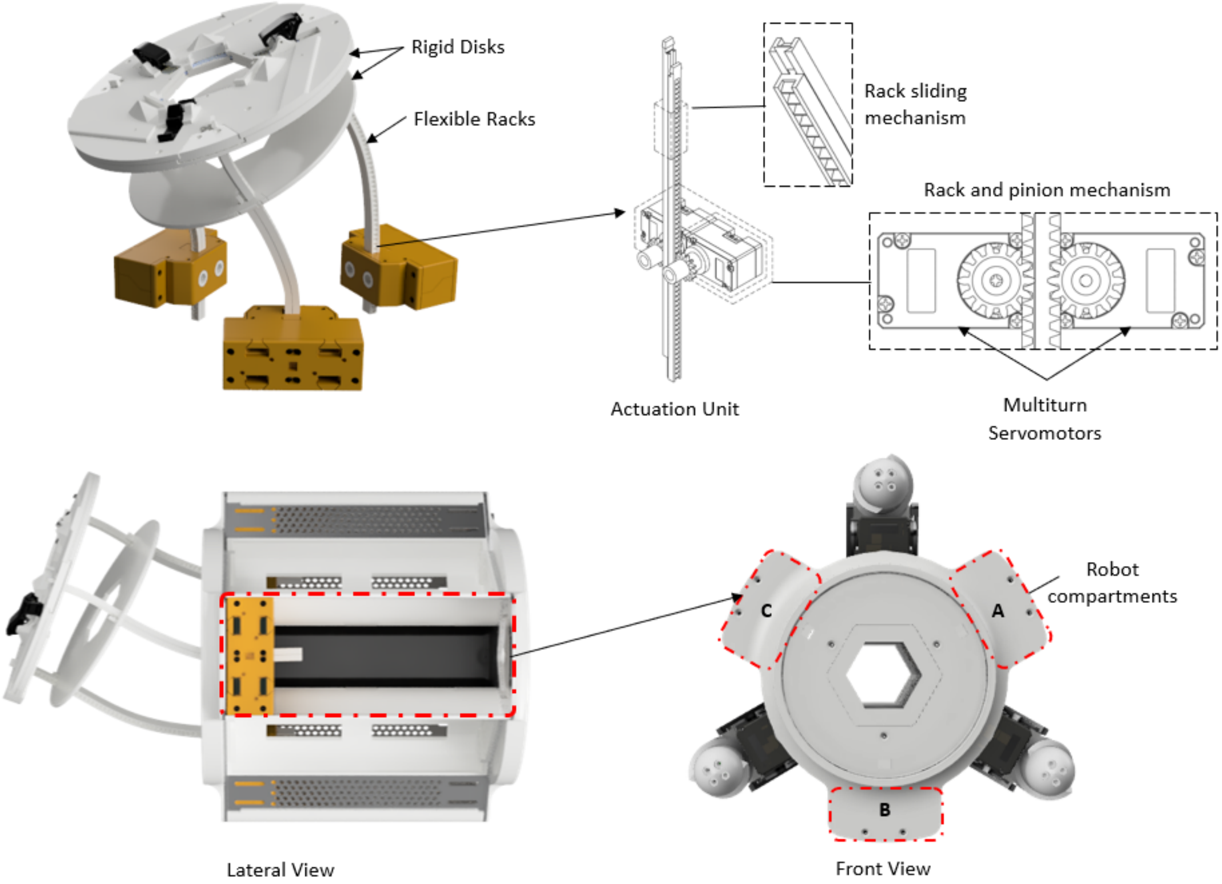

Figure 7. ROBOMINER soft robotic arm description. The arm is integrated into the structure of the modular platform, where a set of servomotors are responsible for actuating each pair of flexible racks following the rack-and-pinion mechanism.

The mechanical interface (Figure 8a) comprises a set of three equally spaced claws driven by a mechanical system composed of a subactuated 4-bar mechanism and a worm-crown gear powered by a small DC motor. The 4-bar mechanism is designed to achieve a wide enveloping movement that helps catch the passive port. Here, the rotational movement of the crown gear translated into the linear motion of the base of the claw that caused the docking maneuver. The maneuver took place when the coupling head was close to a passive coupling port (Figure 8b) following a procedure similar to the one in a car crane. Here the arm reached the docking port, secured the robotic module/submodule, and subsequently retracted, pulling the arm back into the robotic module. Finally, the three magnetic connectors housed inside the arm's tip allowed communication between the modules or module/submodule as well as power-sharing. The remaining pin served as a security check that indicated that the physical connection was correct in all three connectors.

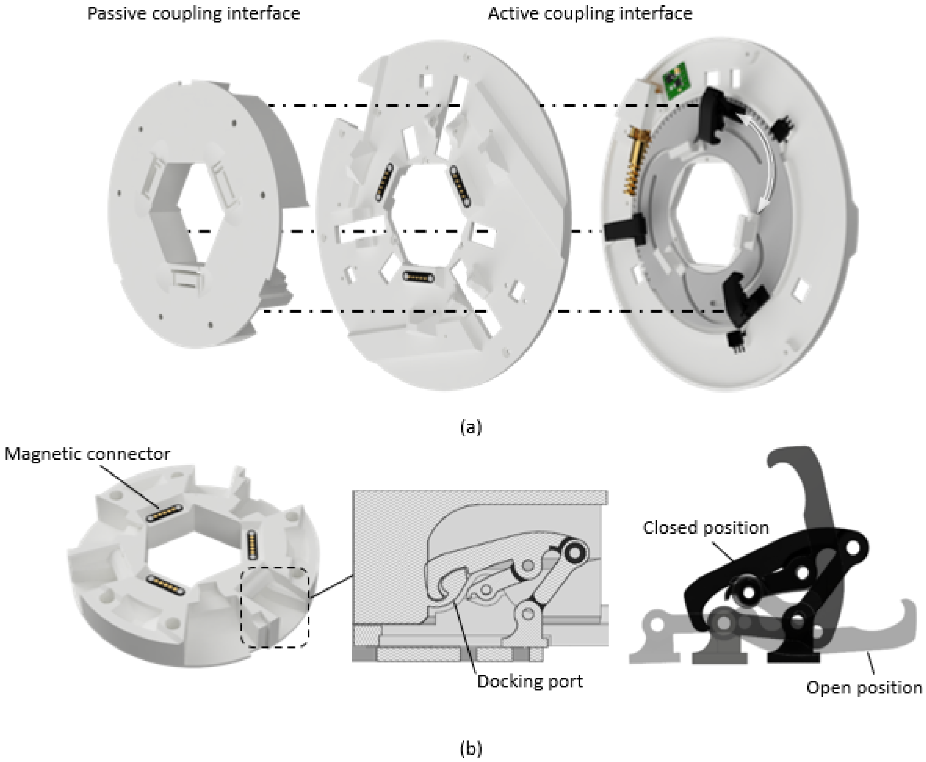

Figure 8. Coupling interfaces for the modular robot. (**a**) process of coupling between the active and passive interfaces where a set of equally distributed claws and profiles secures a passive interface through different docking ports. (**b**) Isometric view of the passive coupling interface with detailed views of the docking port and the enveloping movement of the claw while a docking maneuver is carried out.

3. Robotic Submodules

Because of the coupling mechanism, robotic modules can be configured to form complex systems by connecting to neighboring modules or to specific robotic submodules that perform different tasks. In the following section, we present two robotic submodules that give the system the capability to perform different tasks, like mining or mapping.

3.1. Mining Submodule

Considering that the future robotic miner needs to be able to optimize its path inside the new mine architecture to reach the ore, the correct cutting technology is critical. Roadheaders, traditionally used in tunneling and underground excavation, have demonstrated their efficiency and precision in cutting through rock and other geological formations [21]. By integrating a roadheader into a mining robot, we can envision a versatile and autonomous machine capable of navigating complex underground environments while simultaneously performing accurate and controlled cutting operations. For this reason, we developed a scaled version of a traditional roadheader-cutting head design. The prototype is actuated with a set of linear actuators and an extrinsic universal joint that allows the movement of a cutting head driven by a DC motor (Figure 9a). The actuation mechanism (Figure 9b) generates a circular cutting pattern that covers the area of the robotic miner, allowing it to advance into the mine. Additionally, a suction system is integrated into the submodule to absorb the material to process it later while it passes through the robotic modules, as shown in Figure 9c.

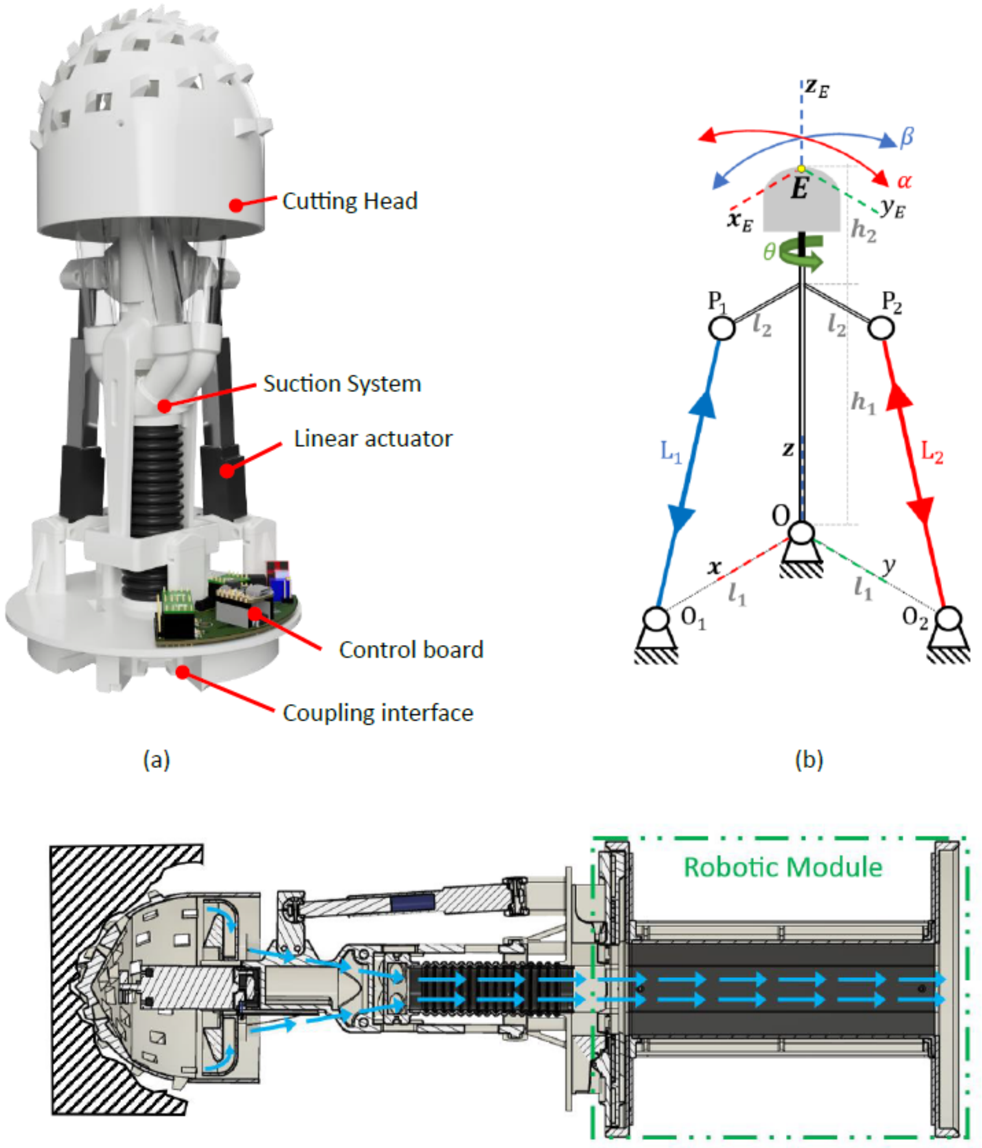

(a)

(b)

(c)

Figure 9. Cutting submodule description. (**a**) Isometric view with component description. (**b**) Model representation of the submodule kinematics. (**c**) Detailed view of the submodule suction system when connected to a modular robot.

3.2. Sensing Submodule

In underground environments where cameras and LiDAR struggle due to low light conditions and dust interference, the preference shifts towards contact-based sensing technology. These advanced systems rely on direct physical contact with objects and surfaces to gather crucial information about the surroundings. By enhancing and expanding the capabilities of contact-based sensing, we can overcome the limitations posed by the absence of light and dust in subterranean environments.

Whiskers are a class of tactile sensors that have recently gained popularity. Inspired by mammals, whiskers display tremendous potential in a variety of applications [22] including robotics. Based on this, we developed a sensing head submodule composed of a circular array of 3D magnetic sensors that translates the magnetic field intensity of a magnet, housed inside a 3D-printed structure resembling a joystick, into a position in space. The magnet holder, presented in Figure 10a is held in place by two silicone rings and allows the structure to move like a joystick (Figure 10b). At the other end of the magnet holder, a rod made of flexible material serves as the point of contact between the geometry that is to be captured and the sensor. When the rod comes in contact with an object, it starts to bend and move the magnet holder. The movement of the magnet is then captured by the sensor, which maps the change of the 3D magnetic field into the resulting bending angle. Finally, considering a model where the rod is rigid and knowing the length of the rod, a point cloud can be generated from the measurements of the sensor array.

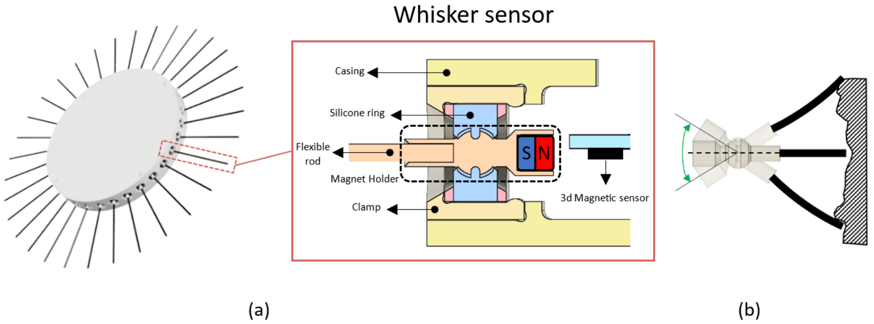

Figure 10. Sensing submodule description. (**a**) The submodule is composed of a circular array of 32 whiskers comprising a magnet holder that has a flexible rod on one end and a magnet on the other. (**b**) The movement of the rod is translated to the magnet which changes the magnetic field measured by the sensor, resulting in the mapping of the point of contact of the flexible rod with a surface.

4. Robotic Module Kinematics

Establishing reference frames is crucial for effective control of the robot since we used these references and the distances between them to determine its position and orientation and main components. Starting with the base reference, we established the robot reference in its geometric center as shown in Figure 11a,b, where the positive x-axis is normal to the front face of the robot. Then, the pivotal point of the leg axis was considered another point of reference, and it was repeated for each leg. The leg reference was considered so that the transformation from the base frame to the leg would be the most convenient. It should be noted that legs 1 and 3 are rotated ±120° with respect to the x-axis of the base reference. Then, for the reference frame of the leg mechanism (Figure 11c) the point resulting from the intersection of the mid-plane of the leg and the second motor axis was considered. This point was set as the origin of the kinematic analysis of the leg mechanism. Finally, the end effector reference frame was set at its center, by which the x-axis coincided with the midpoint of the horizontal bar of the mechanism. The frame's position measured from the robot datum is presented in Table 2.

Table 2. Robominer module reference frames.

Reference Frame	Symbol	Description	$\{x,y,z\}$ with Respect to Base Reference [mm]
Robot Base Datum	O	RM Geometric Center	{0,0,0}
Robot Arm Datum	O_2	Robot Arm Base	{101.87,0,0}
Robot Leg	P_1^1	Leg 1 axis	{0,0,74.653}
	P_1^2	Leg 2 axis	{0,64.95,−37.85}
	P_1^3	Leg 3 axis	{0,−64.95,−37.85}

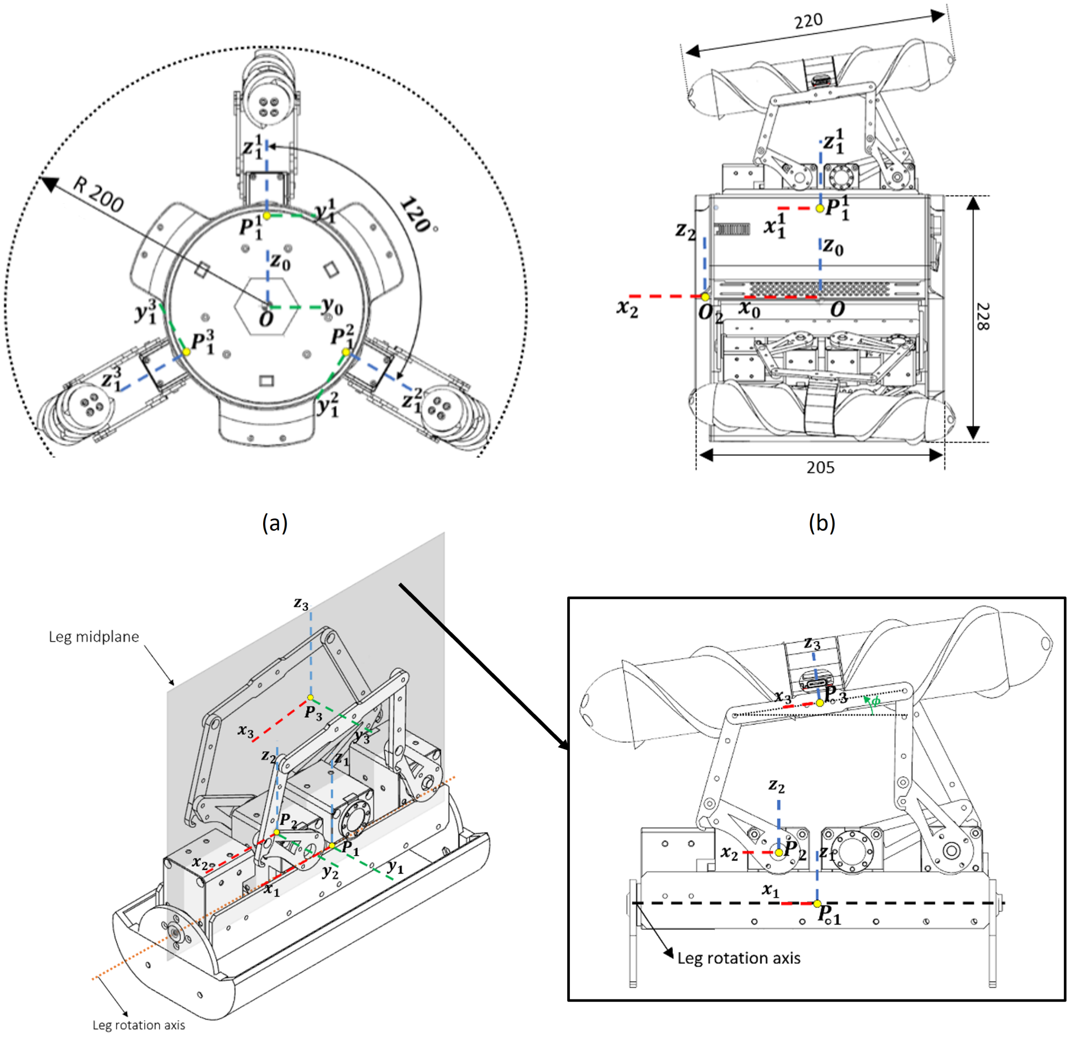

(a) (b)

(c) (d)

Figure 11. Robotic module references frames and transformations to solve the kinematic problem. (**a**) Robot module front view. (**b**) Robot module lateral view. (**c**) Leg mechanism isometric view. (**d**) Midplane view of the leg mechanism equipped with a screw locomotion submodule as an end effector. All measurements are in millimeters.

The robot leg mechanism has 4 DoFs where the motor connected to the docking port acts as a revolute joint that rotates the entire leg. The planar mechanism gives the remaining 3 DoFs, allowing control of the position and orientation of the end effector as shown in Figure 11d. The reference frames for the leg mechanism are shown in Table 3.

Table 3. Leg mechanism reference frame.

Reference Frame	Symbol	Description	$\{x,y,z\}$ with Respect to Leg Axis [mm]
Leg mechanism datum	P_2	Motor_x1	{16.97,0,24.25}
End effector	P_3	End effector joint	See kinematics (Section 4.1)

4.1. Mechanism Description

For the following mechanism, we designed a structure in which the position of point B of the platform (shown in Figure 12) was controlled by a 5-bar planar link ($O_2Q_2BQ_30_3$), and the orientation (ϕ) by a 4-bar link (O_1Q_1FB). Similar to [23], the linear displacements and orientation of the presented structure were decoupled: actuators 2 and 3 (q_2 and q_3) controlled the position of the end effector, and actuator 1 (q_1) controlled its orientation. In addition, the mechanism can rotate on the x-axis, providing the robot with an additional DoF, which was controlled by the front motor.

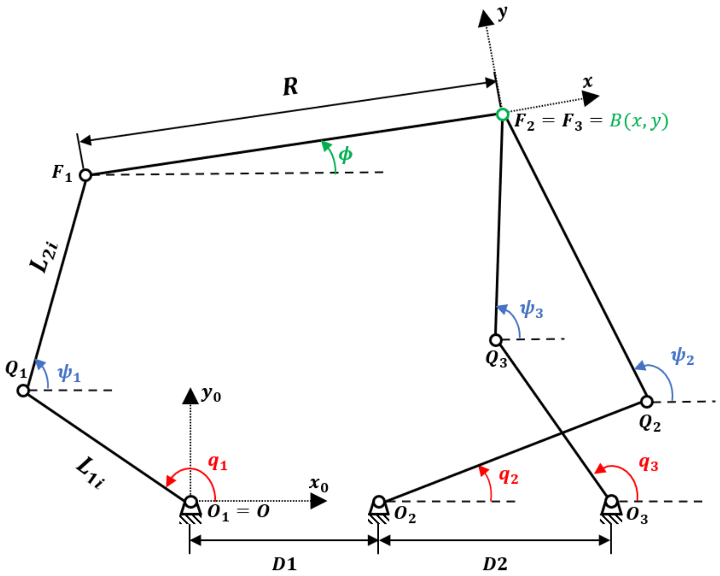

Figure 12. Closed planar kinematic chain analysis of the robot leg. The model represents the simplified version of the leg midplane view (Figure 11d), where O_1 coincides with P_2.

As shown in Figure 12, the axis x_0 is along the vector O_1O_3 and is defined this way for convenience. The lengths of the O_iQ_i and Q_iF_i links are indicated by L_{1i} and L_{2i}, respectively. The dimension of the platform F_1B is indicated by R. The positions of the base axes O_i along the x_0 and y_0 axes are denoted (x_{Oi}, y_{Oi}), with $x_{O1} = y_{O1} = y_{O2} = y_{O3} = 0$. Let us consider the geometric models of the manipulator. From the previous description, one can find the loop–closure equations:

$$\overrightarrow{OB} = [\,\overrightarrow{OO_i} + \overrightarrow{O_iQ_i} + \overrightarrow{Q_iF_i} + \overrightarrow{F_iB}\,] \tag{1}$$

where:

$$\overrightarrow{O_1} = \begin{bmatrix} 0 \\ 0 \end{bmatrix} \tag{2}$$

$$\overrightarrow{O_2} = \begin{bmatrix} D_1 \\ 0 \end{bmatrix} \tag{3}$$

$$\overrightarrow{O_3} = \begin{bmatrix} D_1 + D_2 \\ 0 \end{bmatrix} \tag{4}$$

Developing Equation (1) we obtained the following relationships:

$$\begin{bmatrix} x \\ y \end{bmatrix} = \begin{bmatrix} x_{O_i} + L_{1i}\cos q_i + L_{2i}\cos \psi_i + x_{F_iB} \\ y_{O_i} + L_{1i}\sin q_i + L_{2i}\sin \psi_i + y_{F_iB} \end{bmatrix} \tag{5}$$

Here, $\left[x_{F_iB},\ y_{F_iB}\right]^T$ represents the expression of the vector F_iB in the base frame. For i = 2 and 3, $\left[x_{F_iB},\ y_{F_iB}\right]^T = 0$, and $\left[x_{F_1B},\ y_{F_1B}\right]^T = R[\cos\phi,\ \sin\phi]^T$.

Rearranging Equation (5) and squaring both sides, we obtain the following system.

$$g_1 = (x\ - R\cos\phi - L_{11}\cos q_1)^2 +\ (y - R\sin\phi - L_{11}\sin q_1)^2 -\ {L_{21}}^2 = 0 \tag{6}$$

$$g_2 = \left(x - x_{O_2} - L_{12}\cos q_2\right)^2 +\ (y - L_{12}\sin q_2)^2 -\ {L_{22}}^2 = 0 \tag{7}$$

$$g_3 = \left(x - x_{O_3} - L_{13}\cos q_3\right)^2 +\ (y - L_{13}\sin q_3)^2 -\ {L_{23}}^2 = 0 \tag{8}$$

4.2. Forward Kinematics

The forward kinematics of the robot allows us to determine the position of the end effector given the motor inputs. Due to the decoupling properties of the robot leg, the forward geometric model of the mechanism can be solved in two main steps:

- Find the expression of x and y as a function of q_2 and q_3, using Equations (7) and (8);
- Find the expression of ϕ as a function of q_1, q_2, and q_3 using Equation (6).

Developing Equations (7) and (8) and factorizing with respect to x and y, yields

$$x^2 + d_2 x +\ y^2 + e_2 y + f_2 = 0 \tag{9}$$

$$x^2 + d_3 x +\ y^2 + e_3 y + f_3 = 0 \tag{10}$$

where, for i = 2,3:

$$d_i = -2(x_{Oi} + L_{1i}\cos q_i) \tag{11}$$

$$e_i = -2L_{1i}\sin q_i \tag{12}$$

$$f_i = (x_{Oi} + L_{1i}\cos q_i)^2 + (L_{1i}\sin q_i)^2 - {L_{2i}}^2 \tag{13}$$

From Equations (9) and (10), we obtained the following relation for the horizontal coordinate of B:

$$B_x = \frac{-\left(\ (e_3 - e_2)B_y +\ (f_3 - f_2)\right)}{d_3 - d_2} \tag{14}$$

Introducing it into Equation (9) led to, for $d_3 - d_2\ \neq 0$:

$$u_1 y^2 + v_1 y + w_1 = 0 \tag{15}$$

where

$$u_1 = (d_3 - d_2)^2 + (e_3 - e_2)^2 \tag{16}$$

$$v_1 = 2(f_3 - f_2)(e_3 - e_2) -\ (d_2(d_3 - d_2)(e_3 - e_2)) + e_2(d_3 - d_2)^2 \tag{17}$$

$$w_1 = (f_3 - f_2)^2 - (d_2(f_3 - f_2)(d_3 - d_2)) + f_2(d_3 - d_2)^2 \tag{18}$$

Solving Equation (15) led to the expression for the vertical coordinate of B.

$$B_y = \frac{-v_1 \pm \sqrt{v_1^2 - 4u_1 w_1}}{2u_1} \tag{19}$$

in which the sign ± stands for two possible assembly modes of the system composed of links 1 and 2. In our case, we considered the ″+″ assembly mode according to the mechanism design. Introducing Equation (19) into Equation (14) gave us the position of point *B*. Next, introducing Equations (14) and (19) into Equation (6) led to the following:

$$u_2 \cos\phi \ + v_2 \sin\phi + w_2 = 0 \tag{20}$$

where

$$u_2 = -2R(B_x - L_{11}\cos q_1) \tag{21}$$

$$v_2 = -2R(y - L_{11}\sin q_1) \tag{22}$$

$$w_2 = (x - L_{11}\cos q_1)^2 + (y - L_{11}\sin q_1)^2 - {L_{21}}^2 + R^2 \tag{23}$$

Using the following relationships:

$$\cos\phi = \frac{1-t^2}{1+t^2};\ \sin\phi = \frac{2t}{1+t^2};\ t = \tan\left(\frac{\phi}{2}\right) \tag{24}$$

Equation (20) can be rewritten as the following polynomial equation:

$$(w_2 - u_2)t^2 + 2v_2 t + w_2 + u_2 = 0 \tag{25}$$

Thus, the solutions of Equation (25) can be found as follows.

$$t = \frac{-v_2 \pm \sqrt{v_2^2 - w_2^2 + u_2^2}}{w_2 - u_2} \tag{26}$$

$$\phi = 2\tan^{-1}\left(\frac{-v_2 \pm \sqrt{v_2^2 - w_2^2 + u_2^2}}{w_2 - u_2}\right) \tag{27}$$

Therefore, given the motor input, the orientation of the end effector was determined by solving Equation (27) in which the sign ± stood for the two possible modes of mechanism assembly. In our case, the ″$-$″ solution was the one used since the mechanism was used in this assembly mode.

4.3. Inverse Kinematics

On the other hand, determining the inverse kinematics model, we determined the motor angles that gave a known position and orientation of the end effector.

Rewriting Equations (6)–(8) in a more general way, we obtained

$$g_i = \left(x \ - x_{F_iB} - x_{O_i} - L_{1i}\cos q_i\right)^2 + \ \left(y - y_{F_iB} - y_{O_i} - L_{1i}\sin q_i\right)^2 - \ {L_{2i}}^2 = 0 \tag{28}$$

Developing (28) and factoring with respect to $\cos q_i$ and $\sin q_i$:

$$a_i \cos q_i + b_i \sin q_i + c_i = 0 \tag{29}$$

where

$$a_i = -2\left(x \ - x_{F_iB} - x_{O_i}\right)L_{1i} \tag{30}$$

$$b_i = -2\left(y \ - y_{F_iB} - y_{O_i}\right)L_{1i} \tag{31}$$

$$c_i = \left(x \ - x_{F_iB} - x_{O_i}\right)^2 + \left(y \ - y_{F_iB} - y_{O_i}\right)^2 + {L_{1i}}^2 - {L_{2i}}^2 \tag{32}$$

Using the relations in Equation (24), Equation (29) became

$$(c_i - a_i)t_i^2 + 2b_i t_i + c_i + a_i = 0 \tag{33}$$

Thus, by solving Equation (33), we obtained the following expressions:

$$t_i = \frac{-b_i \pm \sqrt{b_i^2 - c_i^2 + a_i^2}}{c_i - a_i} \tag{34}$$

$$q_i = 2\tan^{-1}\left(\frac{-b_i \pm \sqrt{b_i^2 - c_i^2 + a_i^2}}{c_i - a_i}\right) \tag{35}$$

Therefore, for a given position and orientation of the end effector, the motor input was determined by solving Equation (35). There were two possible solutions that changed consideration of how the mechanism's joints were working. On this occasion, the joints q_1, q_2 considered the ″$-$″ solution, while q_3 considered the ″$+$″ solution.

4.4. Singularity Analysis and Mechanism Workspace

To determine the singular points of the mechanism, we first need to define an implicit function $G_{q_i,x}$ of the set of actuated joints q_i and the Cartesian coordinates x of the end effector. In this case looking at Equations (6)–(8) we wrote the relationship between the input and output coordinates as

$$G(q,x) = \begin{Bmatrix} g1 \\ g2 \\ g3 \end{Bmatrix} = 0 \tag{36}$$

Differentiating (36) with respect to time led to the relationship between the input and output speeds.

$$A\dot{x} + E\dot{q} = 0 \tag{37}$$

where $\dot{x} = [\dot{x}, \dot{y}, \dot{\phi}]^T$is the platform twist; $\dot{q} = [\dot{q_1}, \dot{q_2}, \dot{q_3}]^T$ is the vector of the articular velocities; and A and E are Jacobian matrices of n x n, of which the expressions are

$$A = \left[\begin{bmatrix}\frac{\partial g_i}{\partial x}\end{bmatrix} \quad \begin{bmatrix}\frac{\partial g_i}{\partial y}\end{bmatrix} \quad \begin{bmatrix}\frac{\partial g_i}{\partial \phi}\end{bmatrix}\right] = \begin{bmatrix} \cos\psi_1 & \sin\psi_1 & R\sin(\phi - \psi_1) \\ \cos\psi_2 & \sin\psi_2 & 0 \\ \cos\psi_3 & \sin\psi_3 & 0 \end{bmatrix} \tag{38}$$

$$E = \begin{bmatrix}\frac{\partial g_i}{\partial q_i}\end{bmatrix} = \begin{bmatrix} lL\sin(\psi_1 - q_1) & 0 & 0 \\ 0 & lL\sin(\psi_2 - q_2) & 0 \\ 0 & 0 & lL\sin(\psi_3 - q_3) \end{bmatrix} \tag{39}$$

Singularities occur in configurations where A or E become singular. For this to happen, there are three types that have different physical interpretations and appear when the following conditions are met:

1. Type 1 singularity ($\det(E) = 0$) appears when the segments O_iQ_i and Q_iF_i are located on the same line (Figure 13a)
2. Type 2 singularity ($\det(A) = 0$) appears in two separate cases:
    - when the segments F_1B and Q_1F_1 are collinear (Figure 13b).
    - when the segments Q_2F_2 and Q_3F_3 are located on the same line (Figure 13c).
3. Type 3 singularities ($\det(E)$ and $\det(A) = 0$) are based on the construction of the mechanism. On this occasion, no special singularity was detected based on the mechanism shape.

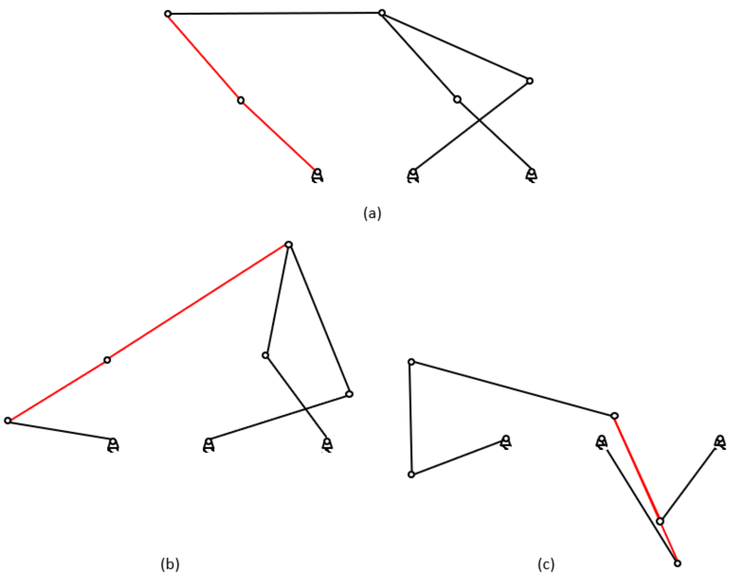

Figure 13. Singular configurations of the robot leg mechanism. (**a**) Singularity type 1. (**b**) Singularity type 2a. (**c**) Singularity type 2b.

Therefore, considering the range for each actuator for the given mechanism (q_1, q_2, q_3) and excluding singular positions, the mechanism workspace was obtained in Figure 14. It should be noted that the mechanism workspace was reduced once a locomotion submodule was installed since the geometry of the submodule reduced the maneuverability of the mechanism.

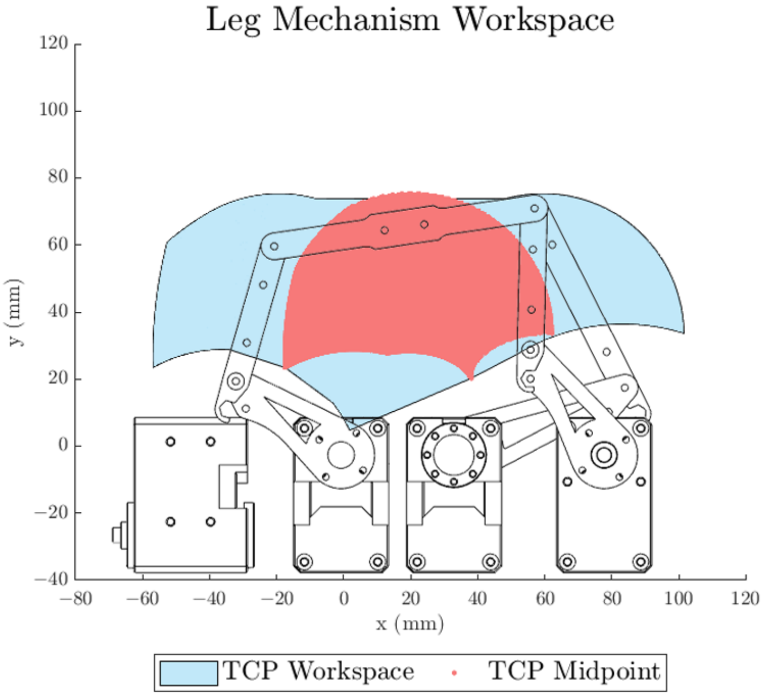

Figure 14. Leg mechanism-resulting workspace. The blue region represents the workspace of the mechanism for the final link represented as a horizontal line in the stored configuration. The red area represents the midpoint position of the final link where the interchangeable end effectors are mounted.

5. Experiments

To assess the abilities of the robotic system, we fabricated two modules with different locomotion configurations along with prototypes of the mining and sensing submodules. The materials chosen for the main structure of the robotic modules included aluminum laser-cut profiles, ABS, and ASA 3D-printed parts. The leg mechanism was also constructed from aluminum. Additionally, the majority of components in the locomotion, mining, and sensing submodules were 3D-printed using ABS.

For the soft robotic arm, the racks were made from a flexible 3D-print material called TPU95A while the rigid disks are made from ABS. These material selections were specifically tailored to suit the size and requirements of the demonstrator. However, it is important to emphasize that for a mine-ready platform, careful consideration and adaptation of materials was necessary. The materials had to withstand the increased stresses and harsh conditions associated with larger sizes and heavier loads in a practical mining environment.

5.1. Module Configurability Test

Several tests were carried out to try different robotic-module setups and achievable robotic systems. Since the module can be configured with different components based on the task to be performed, we present in Figure 15 a set of achievable configurations that could have been adopted by the robotic module.

In standby mode, the robotic modules consume an average of 0.7A. However, during operation with a configuration featuring 3 robot legs, their power demand can increase to 4A.

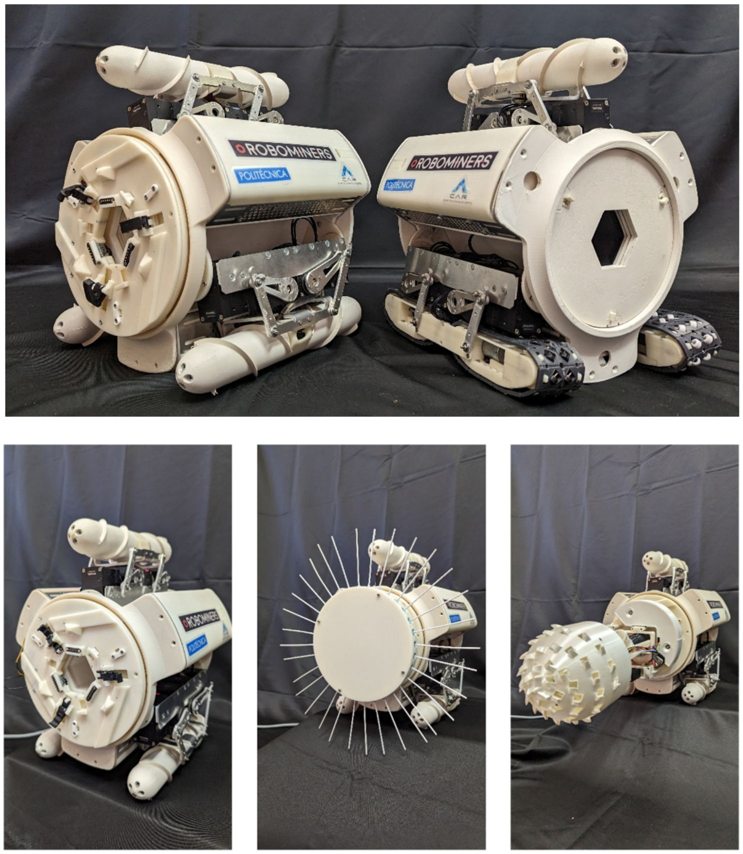

Figure 15. Different possible configurations for ROBOMINER platform. Different locomotion submodules can be easily installed into the robot structure. In addition, other submodules for sensing and mining can be installed when the module has integrated a soft robotic arm.

For the robotic system, two docking experiments were performed where the soft continuum arm coupled two robotic modules together and attached a tool to the robot front. Figure 16 presents a sequence of both experiments. The first experiment consisted of demonstrating the car crane principle by connecting two robotic modules. First, the module arm was teleoperated into the rear port of the second robot module. When the arm docking interface was near the passive interface, a command was sent to the robot to perform the closing maneuver of the claws and profiles into the passive port. Upon completion of this maneuver, the module read the safety check-pin status of the magnetic connectors to ensure that the module was properly connected. Once the module had been secured, the racks were retracted to complete the docking maneuver. Inversely, for the undocking process, a command was first sent to the robot to undock the claws and profiles to the open position. Once this had been completed, the robot sent a message to the CCU confirming that the docking mechanism was in the open position. Next, the robot was commanded to retract the arm into the robot structure to protect it from the environment until a new docking maneuver with a module or submodule is required. While performing the coupling maneuver, the current draw of the module increased up to 1.5A as the second module was pulled into the robot module.

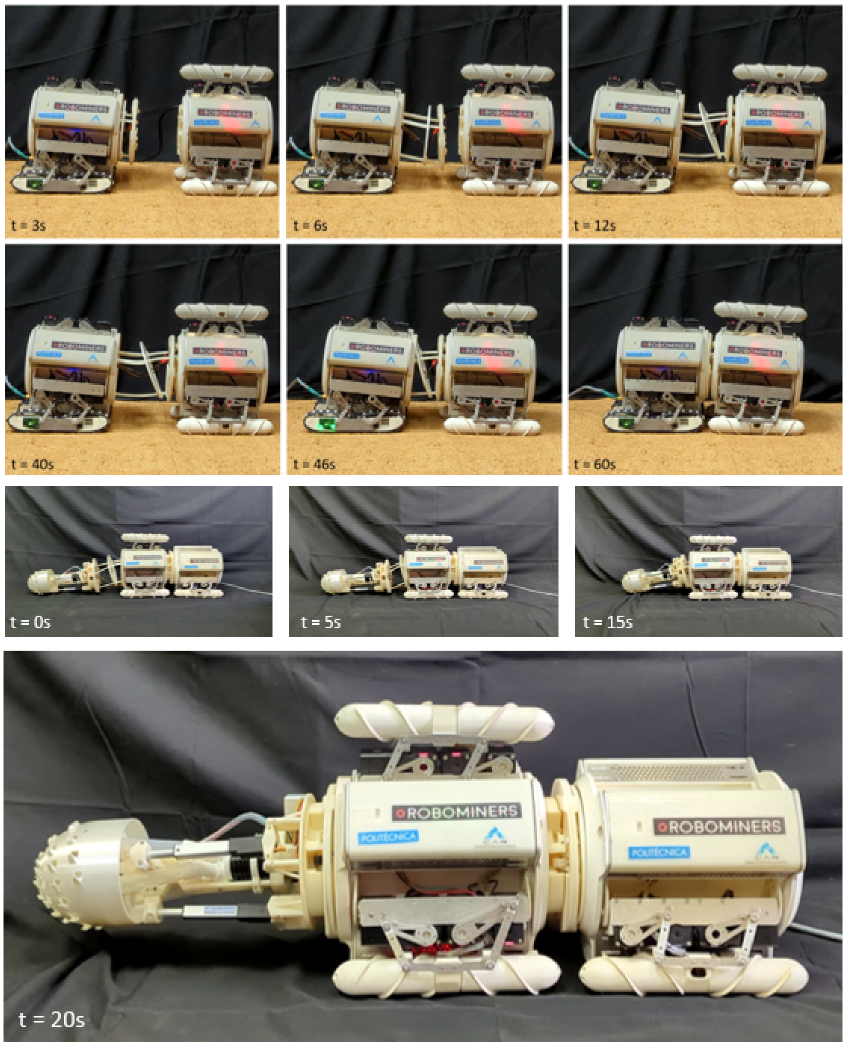

Figure 16. Robotic system reconfiguration test.

For the second experiment, a pre-installed mining submodule was attached to the robotic arm and a retraction of the arm to lift the mining submodule into the robotic system was performed. After the submodule was secured and connected to the robotic module, a new window appeared (Figure 17) in the Qt GUI that allowed the user to control the mining submodule by commanding the linear actuator angles as well as the cutting head speed. The current draw of the resulting system during operation ranged between 3 and 4.5A, with the highest value occurring during the execution of mining tasks. Video S1 from the Supplementary Material shows the coupling maneuvers as well as a mining demo for a robotic system composed of two robotic modules and the mining submodule.

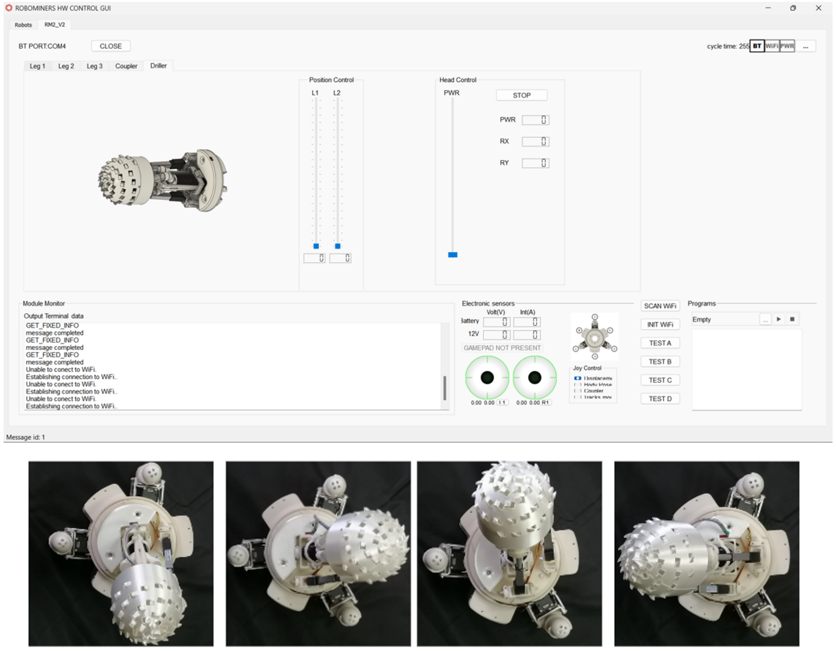

```
GET_FIXED_INFO
message completed
GET_FIXED_INFO
message completed
GET_FIXED_INFO
message completed
Unable to conect to WiFi.
Establishing connection to WiFi..
Unable to conect to WiFi.
Establishing connection to WiFi..
Unable to conect to WiFi.
Establishing connection to WiFi..
```

Figure 17. Mining head connectivity and circular pattern test.

5.2. Locomotion Tests

To validate the design of the locomotion submodules, different tests were carried out. Omnidirectional movement and navigation capabilities of the robotic modules were tested in different scenarios. These included locomotion on inclined and irregular terrain.

The inclined-terrain tests were carried out by varying the slope of a surface where the robot had to climb. Slopes between 10–25° were considered for both robot configurations where the screw module navigated in a lateral fashion while the track wheel advanced straight. The maximum peak current observed was 2A for the Archimedean screw configuration for the 25° slope. Figure 18 shows the sequence for both configurations at different inclinations, where the two modules successfully climbed the four slopes.

To showcase the locomotion capabilities of the module in irregular terrain, various mock-up configurations of unstructured terrain were created and tested. The objective was to assess the ability of the teleoperated module to navigate and exhibit omnidirectional movement. Both screw and track configurations successfully traversed the environment, demonstrating remarkable adaptability and omnidirectional movement within the surroundings. Detailed experiments and visual documentation of these tests can be found in Video S1, available in the Supplementary Materials section.

During the test elaboration, it was observed that the screw structure design exhibited limitations in performing straight movements on smooth terrain. This limitation arose from slippage of the surface and the discontinuity of the screw thread towards the tip of the structure. Similarly, the tracks were unable to execute lateral motion effectively in rough terrain due to improper contact of the passive wheels, which prevented successful maneuvers. However, these issues did not impede the modules' ability to navigate across varied terrain. Future design iterations will address these challenges to enhance the modules' maneuverability in all conditions.

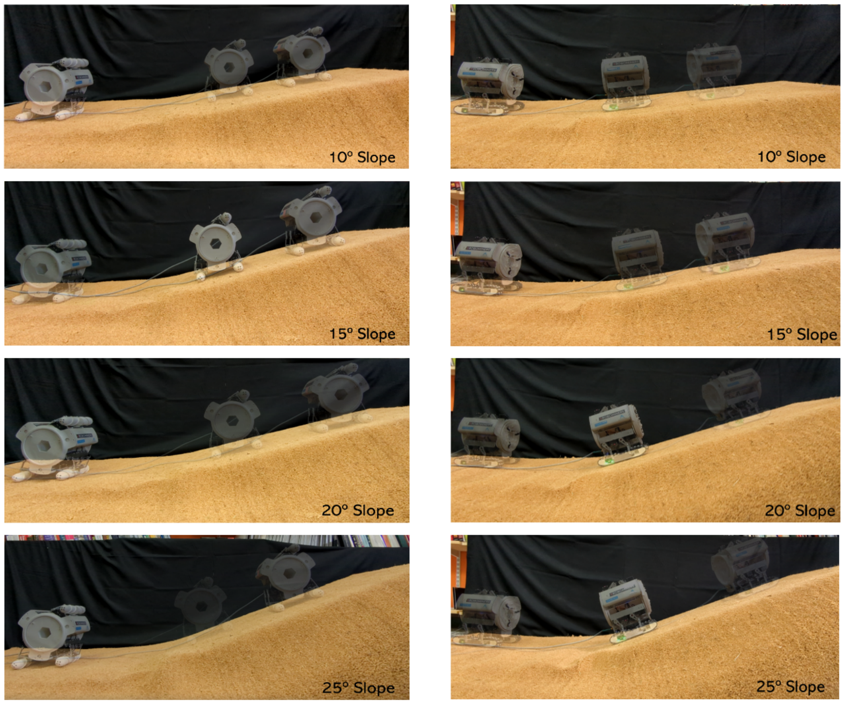

Figure 18. Locomotion capabilities of the robotic module on inclined surfaces. Left, a robotic module with screws; right, the module with omnidirectional tracks.

6. Conclusions

This research paper presented the development of a demonstration modular robotic system to investigate the characteristics of modularity and self-assembly. The article detailed the mechanical and electrical design of the system components, kinematic modeling of the robotic module, and successful tests conducted to assess configurability and locomotion. Through the exploration of various configuration possibilities, the study highlighted the significance of adaptability and versatility in mining operations. This work is a foundational step towards the long-term goal of developing compact autonomous agents capable of self-assembly and completing mining tasks.

The concept of a highly configurable platform was demonstrated by presenting different configurations, with successful coupling maneuvers between robotic modules and submodules using the soft continuum arm. Furthermore, a mining task performed by a system composed of two modules and a mining submodule showcased the potential of applying robotic systems in mining operations.

The locomotion tests yielded satisfactory results for both screw-powered and track-powered submodules. These modules displayed the ability to climb slopes of up to 25° without issue and demonstrated adaptability over rough and irregular terrains. However, some non-critical issues were detected during operation on smooth and irregular terrains for screws and tracks, respectively. On smooth terrain, screws exhibited reduced maneuverability due to limitations in the straight locomotion mode. For tracks, irregular contact of the passive wheels with the terrain affected correct execution of the lateral locomotion mode when traversing irregular terrain. These issues will be addressed in future optimizations of locomotion submodules.

Although the materials and components used in the scaled-down model may not be directly applicable to a real mining system, the underlying concepts validated in this platform can easily be adapted without significant issue. This study serves as proof of concept for a larger, mine-ready robot.

In developing a full-scale mining robotic system, adjustments were essential. The materials needed to be reinforced to withstand the greater stresses and challenges of heavy-duty mining operations. Additionally, the components had to be scaled up to take into account the extreme conditions the platform may encounter within the mine. Moreover, the communication protocols had to be tailored to suit the specific conditions of the mining environment. By addressing these factors, adapting the proven concepts to a real mining system became feasible and practical.

Future research work will focus on enhancing the module's ability to operate in real-world scenarios. This includes developing autonomous self-assembly and collaboration algorithms that enable the robot to adapt to diverse environments. The autonomous self-assembly procedure is currently in development and is based on a computer-vision algorithm where a camera submodule integrated into the module structure captures the position and orientation of a marker located on the coupling interface of a second module or submodule. Then, using the inverse kinematics model, the arm is guided to the captured point. In addition, a set of 3D magnetic Hall-effect sensors assists the arm in aligning the docking interfaces to successfully perform the docking maneuver.

On the other hand, efforts are underway to develop gait methods that allow the robot to adapt to its environment when a locomotion submodule is damaged or encounters an obstacle, thus ensuring robust performance under challenging conditions.

Regarding control strategies, a meta-control model is being developed to improve the robustness and fault tolerance of the robot modules. These strategies, as well as other coordination and configuration algorithms, will be tested on a simulated version of robot modules. Most of these developments are intended to be transferred to a mine-capable robot in real-world scenarios.

Supplementary Materials: The following supporting information can be downloaded at: https://doi.org/10.5281/zenodo.8119182, (accessed on 7 June 2023). Video S1: ROBOMINER_tests.mp4.

Author Contributions: Conceptualization, V.G. and M.H.; Formal analysis, V.G., M.H. and E.A.; Funding acquisition, C.R.; Investigation, V.G. and M.H.; Methodology, V.G.; Project administration, C.R.; Resources, R.S. and C.R.; Software, M.H.; Supervision, M.H.; Validation, V.G. and E.A.; Writing—original draft, V.G.; Writing—review & editing, M.H., E.A., R.S. and C.R. All authors have read and agreed to the published version of the manuscript.

Funding: This research was funded by the European Commission's Horizon 2020 research and innovation program (ROBOMINERS, grant no. 820971) and has received funding from the RoboCity2030-DIH-CM, Centro de Innovación Digital de Robótica de Madrid, S2018/NMT-4331, funded by Programas de Actividades I+D en la Comunidad de Madrid and co-financed by EU Structural Funds.

Acknowledgments: We would like to thank Alvaro Palmero, Daniel Bajo Collados, Oscar Rudek, and Maurizio Lo truglio for their collaboration in the project.

Conflicts of Interest: The authors declare no conflict of interest. Funding institutions had no role in the design of the study; in the collection, analyses, or interpretation of data; in the writing of the manuscript; or in the decision to publish the results

References

1. Rogers, W.P.; Kahraman, M.M.; Drews, F.A.; Powell, K.; Haight, J.M.; Wang, Y.; Baxla, K.; Sobalkar, M. Automation in the mining industry: Review of technology, systems, human factors, and political risk. *Min. Metall. Explor.* **2019**, *36*, 607–631. [CrossRef]
2. Zhang, K.; Kang, L.; Chen, X.; He, M.; Zhu, C.; Li, D. A Review of Intelligent Unmanned Mining Current Situation and Development Trend. *Energies* **2022**, *15*, 513. [CrossRef]
3. Bołoz, L.; Biały, W. Automation and Robotization of Underground Mining in Poland. *Appl. Sci.* **2020**, *10*, 7221. [CrossRef]
4. Wang, M.; Bao, J.; Yuan, X.; Yin, Y.; Khalid, S. Research Status and Development Trend of Unmanned Driving Technology in Coal Mine Transportation. *Energies* **2022**, *15*, 9133. [CrossRef]
5. Shahmoradi, J.; Talebi, E.; Roghanchi, P.; Hassanalian, M. A Comprehensive Review of Applications of Drone Technology in the Mining Industry. *Drones* **2020**, *4*, 34. [CrossRef].

6. Sayed, M.E.; Roberts, J.O.; Donaldson, K.; Mahon, S.T.; Iqbal, F.; Li, B.; Franco Aixela, S.; Mastorakis, G.; Jonasson, E.T.; Nemitz, M.P.; et al. Modular Robots for Enabling Operations in Unstructured Extreme Environments. *Adv. Intell. Syst.* **2022**, *4*, 2000227. [CrossRef].
7. Brunete, A.; Ranganath, A.; Segovia, S.; de Frutos, J.P.; Hernando, M.; Gambao, E. Current trends in reconfigurable modular robots design. *Int. J. Adv. Robot. Syst.* **2017**, *14*. [CrossRef].
8. Dokuyucu, H.I.; Özmen, N.G. Achievements and future directions in self-reconfigurable modular robotic systems. *J. Field Robot.* **2023**, *40*, 701–746. [CrossRef].
9. Liu, J.; Zhang, X.; Hao, G. Survey on research and development of reconfigurable modular robots. *Adv. Mech. Eng.* **2016**, *8*. [CrossRef]
10. Saab, W.; Racioppo, P.; Ben-Tzvi, P. A review of coupling mechanism designs for modular reconfigurable robots. *Robotica* **2019**, *37*, 378–403. [CrossRef]
11. Brown, H.; Vande Weghe, J.; Bererton, C.; Khosla, P. Millibot trains for enhanced mobility. *IEEE/ASME Trans. Mechatronics* **2002**, *7*, 452–461. [CrossRef]
12. Dorigo, M.; Trianni, V.; Sahin, E.; Groß, R.; Labella, T.H.; Baldassarre, G.; Nolfi, S.; Mondada, F.; Deneubourg, J.L.; Floreano, D.; et al. Evolving Self-Organizing Behaviors for a Swarm-bot. *Auton. Robot.* **2004**, *17*, 223–245. [CrossRef]
13. Gross, R.; Bonani, M.; Mondada, F.; Dorigo, M. Autonomous Self-Assembly in Swarm-Bots. *IEEE Trans. Robot.* **2006**, *22*, 1115–1130. [CrossRef]
14. Dorigo, M.; Tuci, E.; Trianni, V.; Groß, R.; Nouyan, S.; Ampatzis, C.; Labella, T.H.; O'Grady, R.; Bonani, M.; Mondada, F. SWARM-BOT: Design and Implementation of Colonies of Self-Assembling Robots. In *Computational Intelligence: Principles and Practice*; Yen, G.Y., Fogel, D.B., Eds.; IEEE Computational Intelligence Society: New York, NY, USA, 2006; pp. 103–136.
15. Guanghua, Z.; Zhicheng, D.; Wei, W. Realization of a Modular Reconfigurable Robot for Rough Terrain. In Proceedings of the 2006 International Conference on Mechatronics and Automation, Luoyang, China, 25–28 June 2006; pp. 289–294. [CrossRef]
16. Wang, W.; Yu, W.; Zhang, H. JL-2: A Mobile Multi-robot System with Docking and Manipulating Capabilities. *Int. J. Adv. Robot. Syst.* **2010**, *7*, 9. [CrossRef]
17. Li, B.; Ma, S.; Liu, J.; Wang, M.; Liu, T.; Wang, Y. AMOEBA-I: A Shape-Shifting Modular Robot for Urban Search and Rescue. *Adv. Robot.* **2009**, *23*, 1057–1083. [CrossRef]
18. Nagaoka, K.; Otsuki, M.; Kubota, T.; Tanaka, S. Terramechanics-based propulsive characteristics of mobile robot driven by Archimedean screw mechanism on soft soil. In Proceedings of the 2010 IEEE/RSJ International Conference on Intelligent Robots and Systems, Taipei, Taiwan, 18–22 October 2010; pp. 4946–4951. [CrossRef]
19. Richter, F.; Gavrilov, P.V.; Lam, H.M.; Degani, A.; Yip, M.C. ARCSnake: Reconfigurable Snakelike Robot With Archimedean Screw Propulsion for Multidomain Mobility. *IEEE Trans. Robot.* **2022**, *38*, 797–809. [CrossRef]
20. Hernando, M.; Bajo, D.; Gomez, V.; Aguado, E.; Rossi, C. Sistema mecáNico de Actuación para un Brazo robóTico Flexible. Spanish Patent No. ES2907801. 2022. Available online: https://es.espacenet.com/publicationDetails/biblio?FT=D&date=20220426&DB=&locale=es_ES&CC=ES&NR=2907801A1&KC=A1&ND=4 (accessed on 6 July 2023).
21. Jun, M.; Jian-gang, L.; Wei-kang, L.; Zhi-yong, H. Kinematics analysis and simulation of profiling memory cutting for tunnel robot in complex environment. *Procedia Earth Planet. Sci.* **2009**, *1*, 1411–1417. [CrossRef]
22. Sayegh, M.A.; Daraghma, H.; Mekid, S.; Bashmal, S. Review of Recent Bio-Inspired Design and Manufacturing of Whisker Tactile Sensors. *Sensors* **2022**, *22*, 2705. [CrossRef] [PubMed]
23. Arakelian, V.; Briot, S.; Jatsun, S.; Jatsun, A. A New 3-DoF Planar Parallel Manipulator with Unlimited Rotation Capability. In Proceedings of the 13th World Congress in Mechanism and Machine Science, Guanajuato, Mexico, 19–23 June 2011.

Publication II

Gomez, V., Hernando, M., Aguado, E., Bajo, D., and Rossi, C., *"Design and Kinematic Modeling of a Soft Continuum Telescopic Arm for the Self-Assembly Mechanism of a Modular Robot"* Soft Robotics, 11(2), 347-360, 2024. doi:10.1089/soro.2023.0020

SOFT ROBOTICS
Volume 00, Number 00, 2023

DOI: 10.1089/soro.2023.0020

Design and Kinematic Modeling of a Soft Continuum Telescopic Arm for the Self-Assembly Mechanism of a Modular Robot

Virgilio Gomez, Miguel Hernando, Esther Aguado, Daniel Bajo, and Claudio Rossi

Abstract

In recent years, the development of mining robots has grown significantly, offering improved efficiency and safety in hazardous environments. However, there is still room for improvement in adaptability, scalability, and overall performance. The ROBOMINERS project, funded by the European Union's Horizon 2020 Research and Innovation Program, aims to facilitate Europe's access to mineral resources applying disruptive robotic concepts. One such concept is resilience, which can be achieved providing modular mining robots with the ability to reconfigure during operation. To address this challenge, this article presents the development and kinematic modeling of a soft, telescopic, continuum arm integrated into a modular robot. The arm serves as a mechanical interface for coupling different robotic modules or tools following the principle of the car crane. With a fully 3D-printed design, the arm features two sections of variable length that are driven by an innovative actuation method based on soft racks. It provides a 6 degrees of freedom (DoF) motion. The arm kinematic models are obtained by backbone parameterization assuming constant curvature and independent bending between sections for forward kinematics and applying a machine learning-based approach for inverse kinematics. The models are validated through the evaluation of two trajectories, measuring the deviation in each DoF and rack extension. Furthermore, a demonstration of the arm's coupling procedure between two robotic modules and one possible configuration of the robotic system showcases its functionality.

Keywords: soft robotics, modular robotics, continuum robot, machine learning, artificial neural networks

Introduction

The application of mining robots has emerged as a promising solution to address the safety hazards, inefficiencies, and environmental concerns associated with traditional mining methods. Equipped with specialized sensors, manipulators, and mobility systems, mining robots have showcased superior endurance, precision, and risk management capabilities, while reducing human exposure to dangerous conditions and minimizing environmental impact.[1]

Despite their potential, mining robots still have room for improvement in terms of adaptability, scalability, and overall performance. One promising approach for achieving these advancements lies in the implementation of modular robot systems. By utilizing interconnected and reconfigurable robotic modules, modular robots offer inherent flexibility and

---

Centre for Automation and Robotics UPM-CSIC, Universidad Politécnica de Madrid, Madrid, Spain.

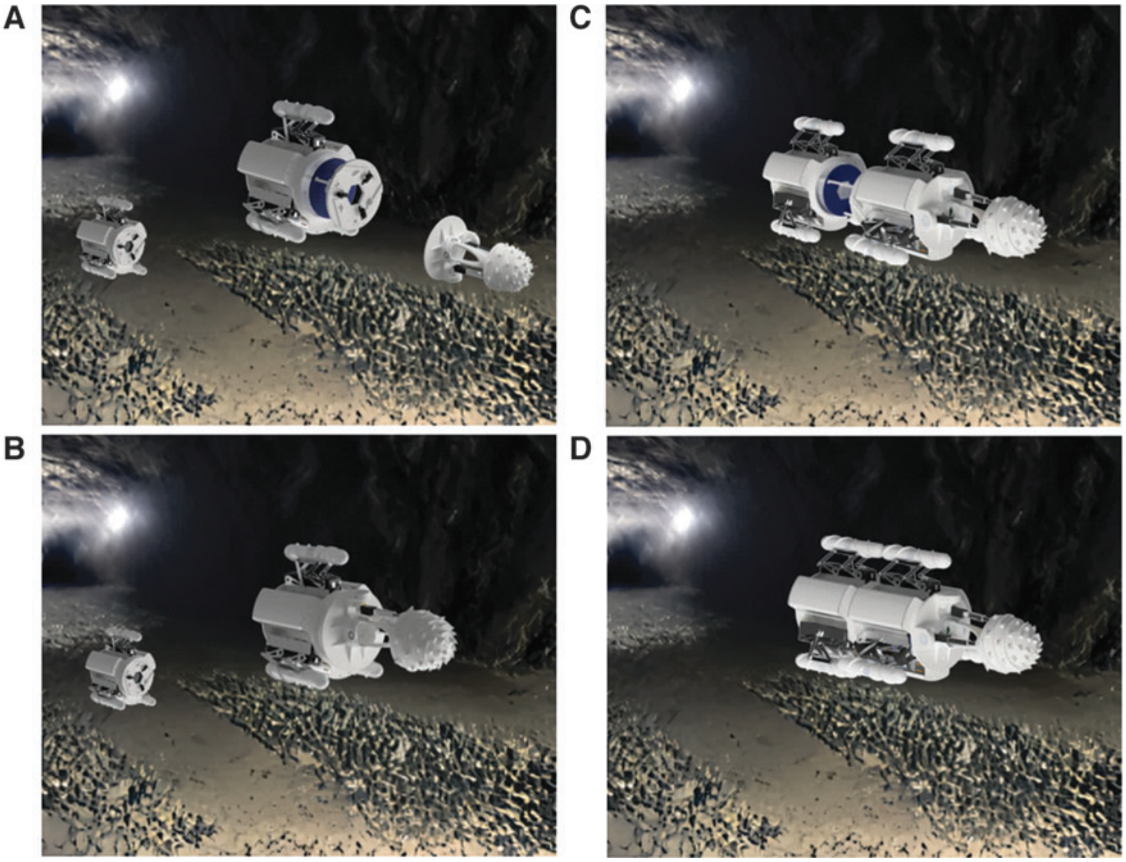

FIG. 1. Robot enhanced autonomy with a continuum arm that acts as a coupling mechanism to support mechanical reconfiguration. **(A)** The robot composed of a single module that detects that it requires a tool to complete the mining task. **(B)** The robot reaches and attaches the extracting tool to the module using the arm. **(C)** In some mine settings, the use of a single module may be not enough to complete the extraction. In this case, the robot detects this situation, reaches a module spare and attaches it. **(D)** The resulting robot comprises two modules and an extracting tool that can operate on hard rock.

versatility, allowing them to adapt to evolving mining conditions, tasks, and objectives.[2] A modular robot is more adaptable and resilient since it can change its morphological reconfiguration or easily replace defective modules during operation.

The ROBOMINERS project,* funded by the European Union's Horizon 2020 Research and Innovation Program, aims to integrate disruptive robotic concepts to facilitate Europe's access to mineral raw materials. As part of this initiative, a technology demonstrator based on a set of modular robots with self-assembly capabilities is currently under development.[3] The demonstrator, serving as a scaled-down model of a robotic miner, focuses on studying the characteristics of modularity and self-assembly, laying the foundation for the future development of a mine-ready robotic platform.

Implementing a robust and efficient coupling mechanism that allows one module to reach other modules or submodules plays a pivotal role in realizing the long-term goal of developing modular mining robots capable of self-assembling and performing mining operations, while adapting to dynamic environments. The usage of traditional robotic arms embedded in the structure of robots is a common practice for extreme environments. However, this solution can result in a more complex and bulky robotic system. In addition, traditional coupling mechanisms, such as mechanical connectors or latches, face notable challenges in the demanding conditions of mining environments. Factors such as uneven terrain, limited visibility, and unpredictable elements often hinder proper module connections, compromising the stability and functionality of the robot system.[4] Other methods, such as electromagnetic couplings, have the disadvantage of continuous power consumption since they must maintain the coupling force.

Continuum robots, characterized by their flexible structures, reduced weight, simplicity, and adaptability, offer significant advantages over traditional rigid-body arms.[5] They have been increasingly utilized in complex scenarios, such as manipulation and locomotion in unstructured environments,[6–8] where bioinspired designs, including snake bodies and tails,[5,9] or tentacles,[10,11] are commonly employed for their dexterity and flexibility. Continuum arms consist of multiple, serially connected sections and can be actuated using different strategies[12] to control the pose of the arm. The main actuation technologies can be classified according to their actuation principles in tendon-driven, fluidic, and smart material actuation.[13] Regarding the arm's construction,

---

*https://robominers.eu

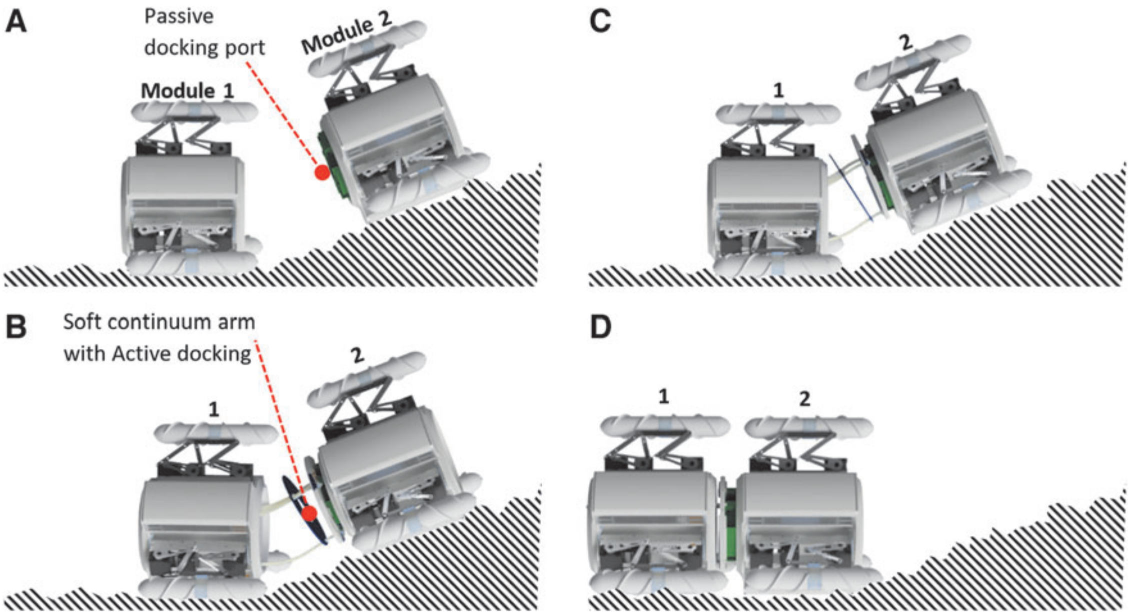

FIG. 2. **(A)** Car crane principle for docking robots or tool modules. **(B)** First, the soft continuum arm is guided to the module/tool docking port. **(C)** Then, the end effector docking mechanism secures the module/tool. **(D)** Finally, the arm is retracted back to the module securing and attaching the desired part.

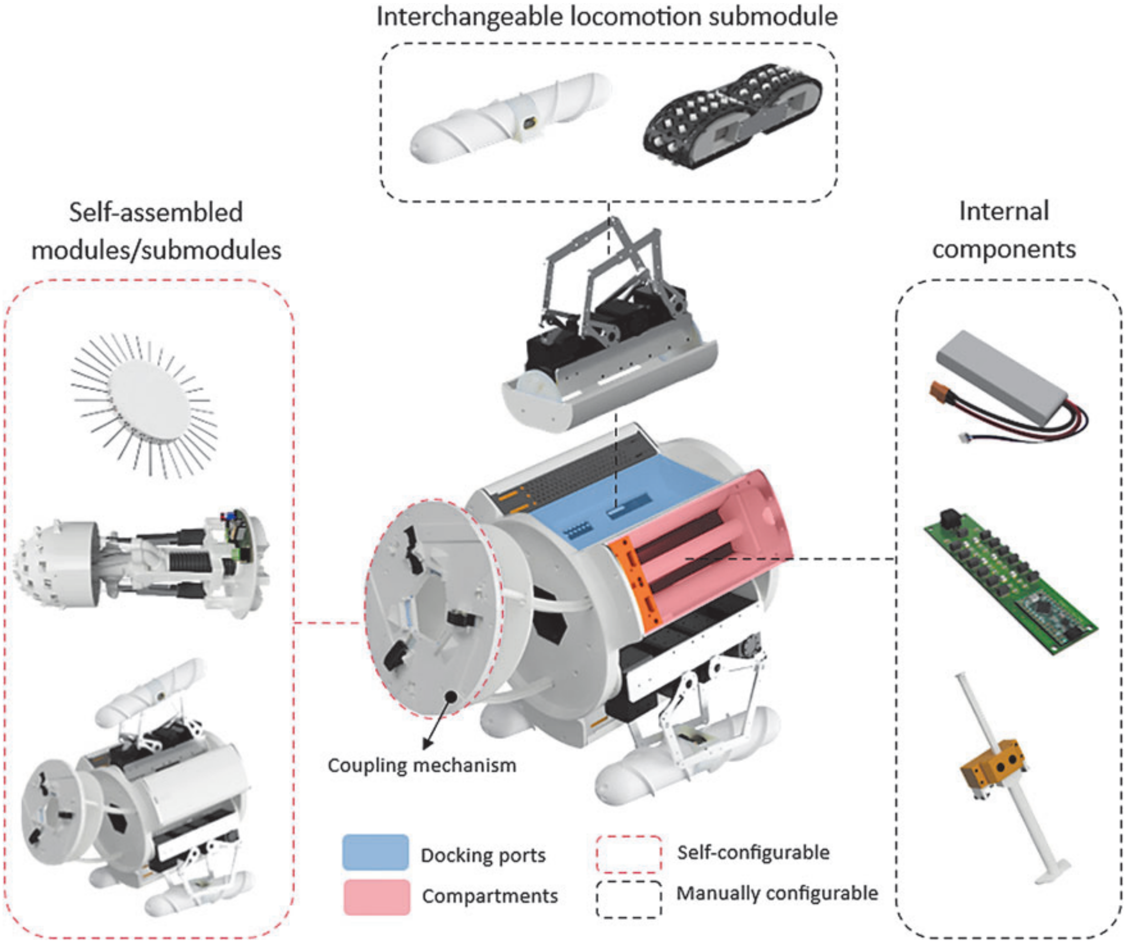

FIG. 3. Robotic module description. Each robotic module comprises three compartments and three docking ports. The compartments house various internal components, whereas the docking ports accommodate interchangeable locomotion submodules. The coupling mechanism allows the autonomous coupling of different robotic modules and submodules for seamless integration and greater versatility.

different types of materials can be used, including silicone rubbers,[14] shape memory alloys and polymers,[15] or 3D-printed flexible filaments.[16]

Integrating continuum arms as coupling mechanisms allows modular mining robots to enhance their adaptability and performance, enabling tool exchange and structural modifications during operation, and addressing the challenges of unstructured mining environments. For instance, Figure 1 depicts a situation where the robotic modules support this capability during a mining task. In this context, the robot may change its cutting heads depending on the concrete material it is extracting, attaches special sensing devices, connects several modules to increase its strength, or replaces failed modules with new ones, thus reconfiguring itself on the job.

To address these challenges, the present study introduces a novel approach in the form of a modular robot coupling mechanism. This mechanism utilizes a 3D-printed soft continuum arm with extensible sections, driven by an innovative actuation method based on the rack and pinion mechanism. The integration of this prototype arm into a modular robot provides a mechanical interface, enabling the robot to effectively reach and attach various tools or additional robotic modules. The arm's end effector consists of a docking mechanism composed of a set of hooks that employ a docking strategy similar to that of a car crane, as presented in Figure 2. The coupling interface integrates a set of magnetic connectors to share data and power between modules. By incorporating two sections, the arm achieves a total of 6 degrees of freedom (DoF), allowing control over the end effector position and bending orientation.

The article is organized as follows. The Robominers Concept section contains a description of the modular robot system and the soft continuum arm design and manufacturing procedure. In the Kinematics Modeling section, both forward and inverse kinematic models of the robot arm are solved using analytical and data-driven approaches, respectively. In the Results and Discussion section, a comparison of the results obtained from both the kinematic models and the experimental data is presented. The Conclusions section provides the conclusions of the results obtained from the analysis and summarizes future developments and improvements to the prototype presented.

Robominers Concept

Robotic module

The proposed robotic system addresses the long-term vision of the project, where robotic modules are sent down to the mine through a borehole and self-assemble to form a fully functional mining robot that can reconfigure on-the-job to cope with failures and/or adapt to different situations. The ability to replace defective modules during operation ensures continuous operation and minimizes downtime.

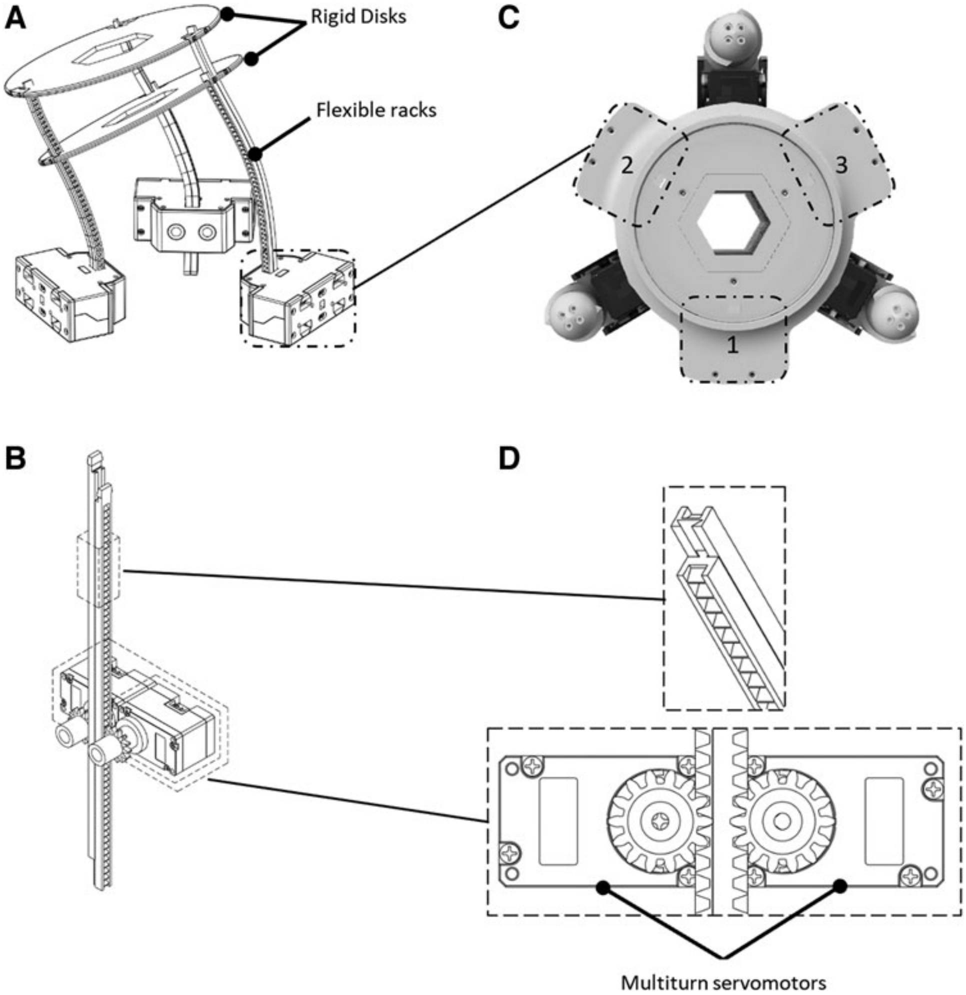

FIG. 4. **(A)** 3D CAD model of the soft continuum arm prototype extended with two sections of variable length. **(B)** 3D CAD model of the prototype AU. **(C)** 3D CAD model of the robotic module where the arm is integrated. **(D)** Detailed view of the rack and pinion and flexible adjacent racks sliding mechanism. AU, actuation unit; CAD, computer-aided design.

Each module of the system consists of a main structure with three compartments and three docking ports, as illustrated in Figure 3. These compartments house electronic components, batteries, and actuators for the coupling arm, while the docking ports allow for the assembly of interchangeable end effectors, such as legs with screws or continuous tracks, based on the specific task requirements. In this study, we focus on the modules' coupling mechanism, but docks can also be used to change the robot's configuration.

The coupling interface enables seamless connections between modules, allowing for the formation of complex structures that are composed of different modules and submodules. In addition, it allows the exchange of data, force, and power among modules. Thus, the proposed soft robotic arm serves as a critical component, providing dexterity, compliance, and adaptability, which are essential for the robot's versatility and effectiveness in different scenarios.

Telescopic soft continuum arm design

The prototype arm, presented in Figure 4A, consists of two sections composed of a set of flexible racks and rigid disks where the rack's endpoints are attached. The movement of each section is based on the displacement of the racks that can extend, retract, and bend, obtaining as a result 3 DoF per section, 2 for bending and 1 for the extension. Therefore, having two sections, we obtain the final configuration of the arm that gives 5 DoF for the arm tip position (X, Y, Z) and orientation (Pitch, Roll) and an additional DoF to control the bending inflection point. To simplify assembly, each pair of racks is fixed in a single piece, which will be referred to as an actuating unit (AU), presented in Figure 4B.

Each AU is driven by two multi-turn servomotors (DYNAMIXEL XL330-M288-T), where each servomotor controls the extension of a single rack using the rack and pinion mechanism, and the two racks that can slide between them (Fig. 4D). The arm is totally integrated into the structure of the robot, as shown in Figure 4C, where the AUs that drive the arm sections are placed inside each of the robot compartments, resulting in an extrinsically actuated arm. Since the proposed actuation mechanism offers a novel driving method for robotic soft continuum arms, a patent has been granted.[17]

The arm is used as a mechanical interface to join two robotic modules or tools to the robot. The docking mechanism (Fig. 5A) comprises a set of three equally spaced claws, T-shaped profiles, and magnetic connectors. The claws are driven by a mechanical system composed of a subactuated 4-bar mechanism and a worm–crown gear powered by a small direct current motor. The 4-bar mechanism is designed to achieve a wide enveloping movement that helps catch the passive port. The T-shaped profiles secure the two pieces together after the claws have captured the passive coupling port (Fig. 5B).

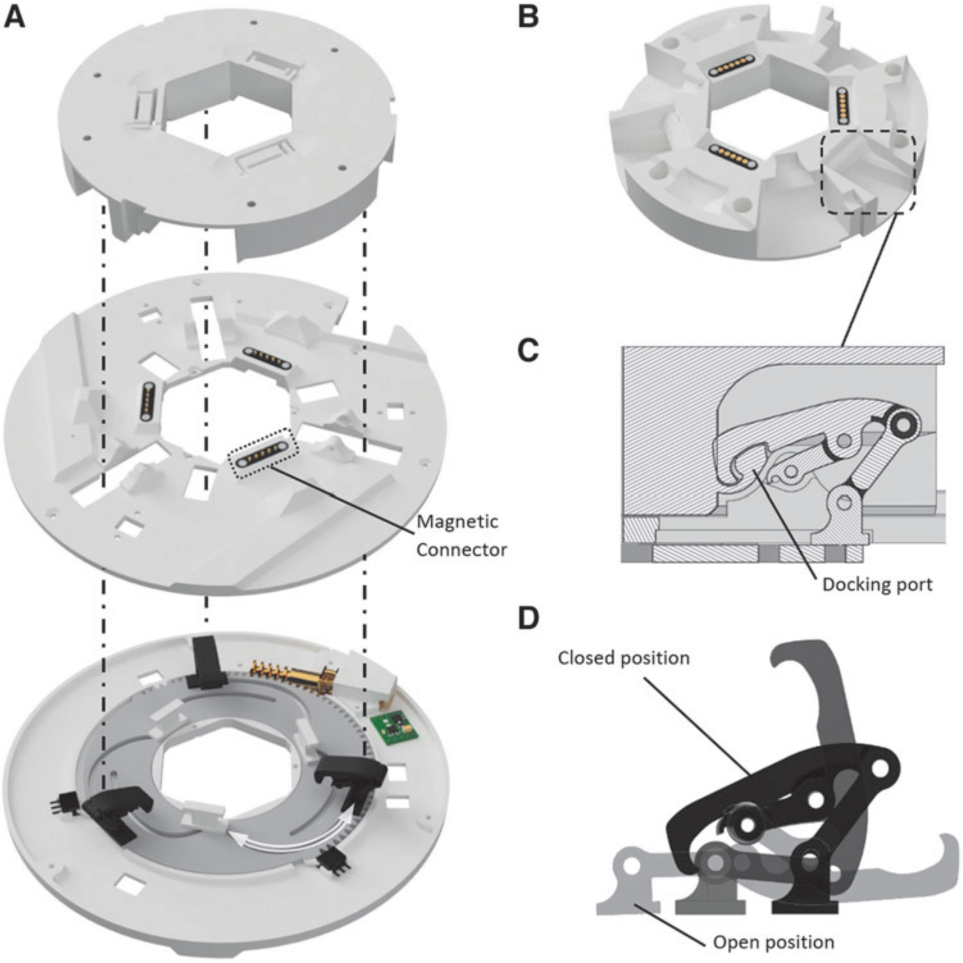

FIG. 5. **(A)** 3D CAD model of the soft continuum arm coupling mechanism installed at the tip of the arm. **(B)** 3D CAD model of the passive docking port. **(C)** Detailed view of the coupling between the active and passive ports. **(D)** Detailed view of the claws' range of movement in the coupling mechanism.

Table 1. Mechanical Properties of the Materials Tested for the 3D-Printed Racks

Material	*Mechanical properties*	*Test method*	*Typical values*
PLA Extrafill	Tensile strength at break	ASTM D882	53 MPa
	Elongation at break	ASTM D882	6%
	Flexural modulus	ASTM D790	3800 MPa
	Print temperature	—	190–210°C
Flexfill TPU 98A	Tensile strength at break	DIN 53504	53.7 MPa
	Tensile stress (10–300% elongation)	DIN 53504	12.1–37.8 MPa
	Elongation at break	DIN 53504	318%
	Hardness	ISO 7619–1	98 Shore A, 60 Shore D
	Print temperature	—	220–240°C
Ultimaker TPU 95A	Tensile (Young) modulus	ASTM D3039	(67, 67, 56)[a] MPa
	Tensile stress at break	ASTM D3039	(6.4, 23.7, 37.9)[a] MPa
	Elongation at break	ASTM D3039	(>560, >700, 84)[a] %
	Flexural modulus	ISO 178	(62.6, 55.1, 62.6)[a] MPa
	Hardness	ISO 7619–1	96 Shore A, 48 Shore D
	Print temperature	—	220–235°C

[a] Reported values for XY, YZ, and Z print orientations.

Data and power transmission is achieved, thanks to magnetic connectors embedded in both coupling interfaces. The docking maneuver takes place when the coupling head is close to a passive coupling port. The maneuver is carried out by closing the claws into the coupling port, as presented in Figure 5C and D. Here, the rotational movement of the crown gear translates into a linear motion of the base of the claw that causes the docking maneuver. Then, the second module is pulled into the robotic module by retracting the racks. Thanks to the rack and pinion design, the arm has high mass pulling force capabilities.

Material selection

Considering that the arm is fully 3D printed and will suffer bending and torsional forces, as this is part of its mechanical

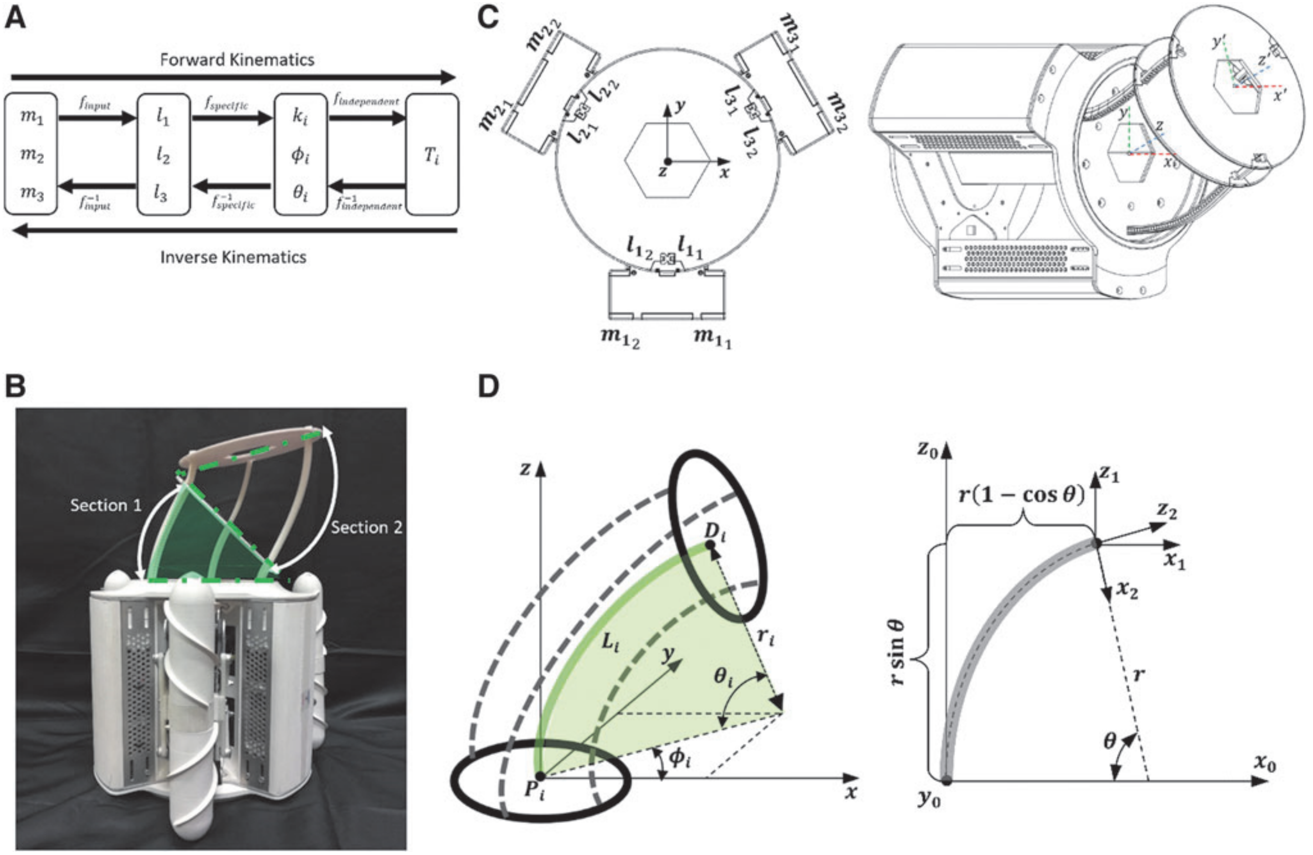

FIG. 6. **(A)** Kinematic modeling diagram for transforming motor input to coordinate position and orientation of the arm. **(B)** Constant curvature model for a single section of the presented soft continuum arm. **(C)** Motor, rack lengths, and coordinate frames convention for the arm direct kinematics model. **(D)** Constant curvature model for a single section of the presented soft continuum arm.

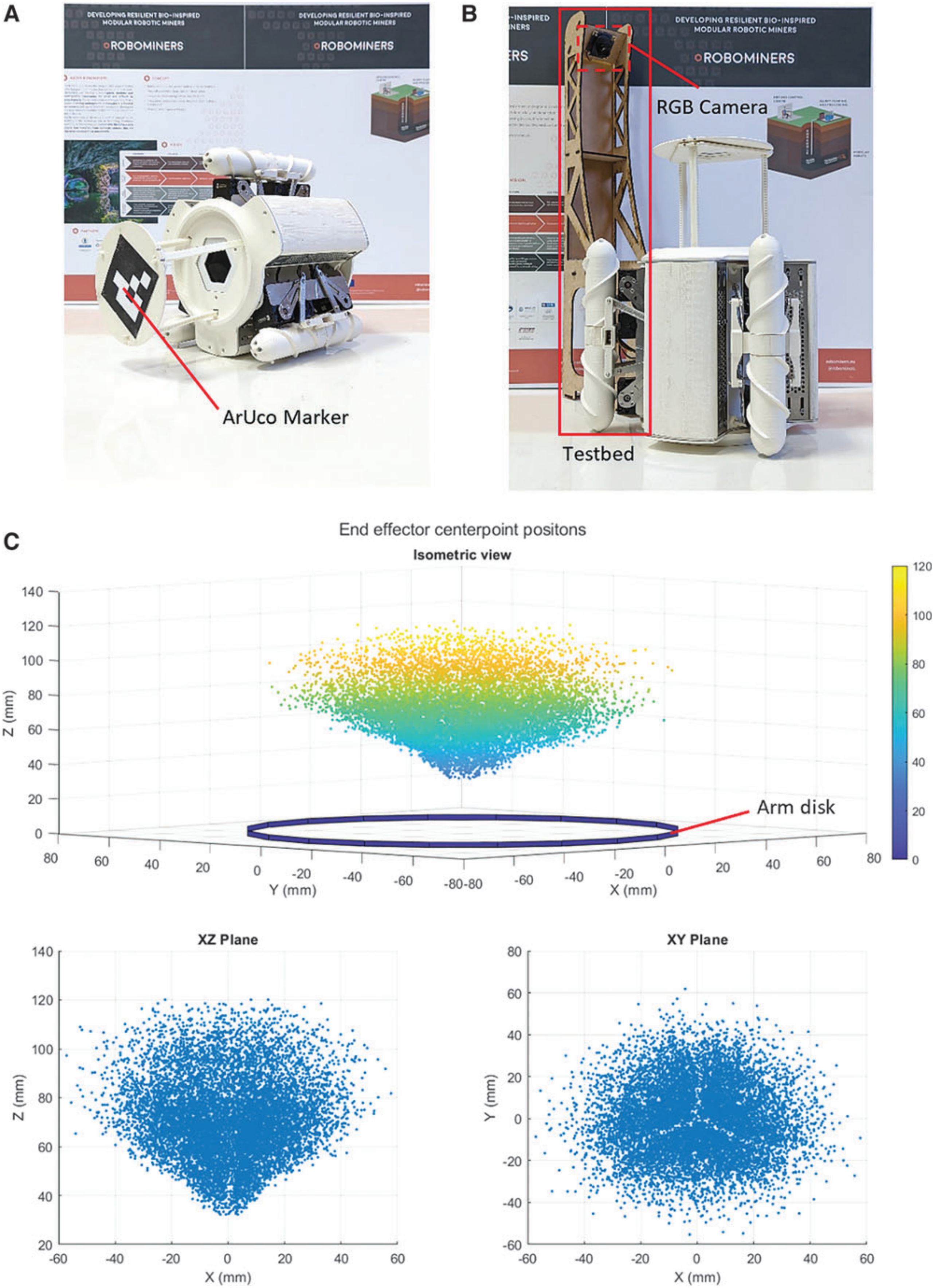

FIG. 7. **(A)** ArUco marker fixed to the arm tip for pose capturing. **(B)** Testbed to capture arm end disk position and orientation. **(C)** Safe workspace of the arm derived from captured data of the arm tip position.

principle, it is necessary to select materials that give us the capability to maintain the structural integrity of the arm while performing different maneuvers. For this reason, a material selection study was performed to identify the most suitable material for racks by testing three commercially available materials (PLA Extrafill, FLexfill TPU 98A, and Ultimaker TPU 95A) for bending and twisting. The mechanical properties of the material are presented in Table 1.

After evaluating the capabilities of the test racks for different materials, the most suitable material for this design resulted in Ultimaker TPU 95A, given its bending and twisting capabilities, while maintaining mechanical integrity. Polylactic acid (PLA) and TPU 98A were discarded because they suffered rigidity and mechanical integrity issues when tested. PLA was also considered as an option even though it is not particularly flexible (Table 1) since it was essential for the arm to extend until it reached the target, flexing minimally and pulling a mass of the target.

Kinematics Modeling

The kinematic modeling of soft continuum arms is a rather complex task[18] due to the inherent dexterity of the arm. As they are flexible, the continuous bending and torsional effects of the drive system, which introduce nonlinearities into the system, must be considered in the model. Soft continuum arm kinematic are commonly solved by model-based, data-driven, or hybrid approaches.[19] Generally, model-based approaches are implemented to solve forward kinematics, where virtual backbone parameterization, assuming constant curvature, is one of the most common approaches.[20] On the contrary, for the inverse kinematic problem, data-driven approaches are frequently used for approximating the models of flexible manipulators. This is due to its speed and effectiveness, where well-known architectures such as multilayer perceptron (MLP), K-nearest neighbors regression (KNNR), extreme learning machine (ELM), or Gaussian mixture regression are usually implemented.[21]

Bearing this in mind, two approaches are considered to solve the forward and inverse kinematics: the model-based method assuming constant curvature and independent bending between sections for the forward kinematics, and the data-driven model based on machine learning algorithms for the inverse kinematics.

Forward kinematics

A constant curvature model with independent untangled bending between sections is implemented to solve the kinematics of the arm, as shown in Figure 6B. The expression of the arm tip pose is determined by following three main steps (Fig. 6A). First, the raw motor input (m_{ij}) is converted to the extension of the rack (m_{ij}) following the principle of the rack and pinion mechanism. Here, i indicates the rack number and j the arm section, as presented in Figure 6C. Then, using the model from Webster and Jones,[22] the section's arc parameters (k_i, ϕ_i, θ_i) are obtained from the corresponding section rack lengths.

As shown in Figure 6D, k_i represents the backbone curvature, ϕ_i represents the orientation of the virtual backbone with respect to the xy plane, and θ_i represents the virtual backbone arc angle. Finally, the transformation matrix (T_i) of the distal point of the section (denoted as D_i in Fig. 6D) is determined by applying the robot-independent function described in the model. The notation considered is a Bishop frame,[22] where the z axis is tangent to the virtual backbone of the arm (L_i), and the coordinates x and y have the same orientation that the base reference frame (Fig. 6C), where $-y$ points to l_1.

Following the diagram of Figure 6A, motor input is converted into rack lengths by applying the rack-and-pinion mechanism relation. Here, D_P and m_i represent the gear primitive diameter measured in millimeters and each motor input angle measured by the encoder in degrees, respectively.

$$l_i = \frac{\mathrm{m}_i \pi D_P}{360} \tag{1}$$

Then, based on the model, the section's arc parameters are obtained.

$$k_i = \frac{1}{r_i} = \frac{2g_i}{3L_i d} \tag{2}$$

$$\phi_i = atan2\left(\frac{l_2 + l_3 - 2l_1}{\sqrt{3}(l_2 - l_3)}\right) \tag{3}$$

$$\theta_i = L_i k_i = \frac{2g_i}{3d} \tag{4}$$

where d represents the disk radius and:

$$L_i = \frac{(l_1 + l_2 + l_3)}{3} \tag{5}$$

$$g_i = \sqrt{{l_1}^2 + {l_2}^2 + {l_3}^2 - l_1 l_2 - l_1 l_3 - l_2 l_3} \tag{6}$$

The section's homogeneous transformation matrix is defined modeling the constant curvature section of the continuum arm. First, the arm is rotated in the z-axis with no translation by the angle ϕ. Then, another rotation is performed in the y-axis by the angle θ combined with a translation with the vector $p = [\,r(1 - \cos\theta) \quad 0 \quad r\sin\theta\,]$. Finally, a rotation in the z-axis that has no translation gives the resulting homogeneous transformation matrix. For compactness of notation, $\sin\phi$ and $\cos\phi$ are denoted s_ϕ and c_ϕ, respectively.

$$\begin{aligned} &T_i(r, \theta, \phi) \\ &= \begin{bmatrix} R_z(\phi) & 0 \\ 0 & 1 \end{bmatrix} \begin{bmatrix} 0 & p(r, \theta) \\ 0 & 1 \end{bmatrix} \begin{bmatrix} R_y(\theta) & 0 \\ 0 & 1 \end{bmatrix} \begin{bmatrix} R_z(-\phi) & 0 \\ 0 & 1 \end{bmatrix} \end{aligned} \tag{7a}$$

Table 2. Arm Safe Operating Range

DoF	*Units*	*Min*	*Max*
X	mm	–58	58
Y	mm	–55	61
Z	mm	0	120
Pitch	deg	–60	60
Roll	deg	–60	60

DoF, degrees of freedom; Max, maximum; Min, minimum.

Table 3. Comparison between the Three Considered Machine Learning Algorithms for the Inverse Kinematic Model of the Soft Continuum Arm

	ELM (N_hidden_neurons = 150)			*KNN (N_neighbors = 5)*			*MLP single layer (N_hidden_neurons = 400)*		
Rack extension	*MAE (mm)*	*RMSE (mm)*	*Time (ms)*	*MAE (mm)*	*RMSE (mm)*	*Time (ms)*	*MAE (mm)*	*RMSE (mm)*	*Time (ms)*
l_{11}	7.51	10.15	24.4	8.81	12.13	56.1	10.72	13.53	49.5
l_{21}	7.59	10.30		8.84	12.17		10.89	13.97	
l_{31}	7.48	10.06		9.01	12.53		10.51	13.41	
l_{12}	4.93	6.10		5.76	7.29		5.98	7.44	
l_{22}	4.84	5.96		5.87	7.41		5.96	7.31	
l_{32}	4.84	5.98		5.89	7.45		5.89	7.29	

ELM, extreme learning machine; KNN, K-nearest neighbors; MAE, mean absolute error; MLP, multilayer perceptron; RMSE, root mean squared error.

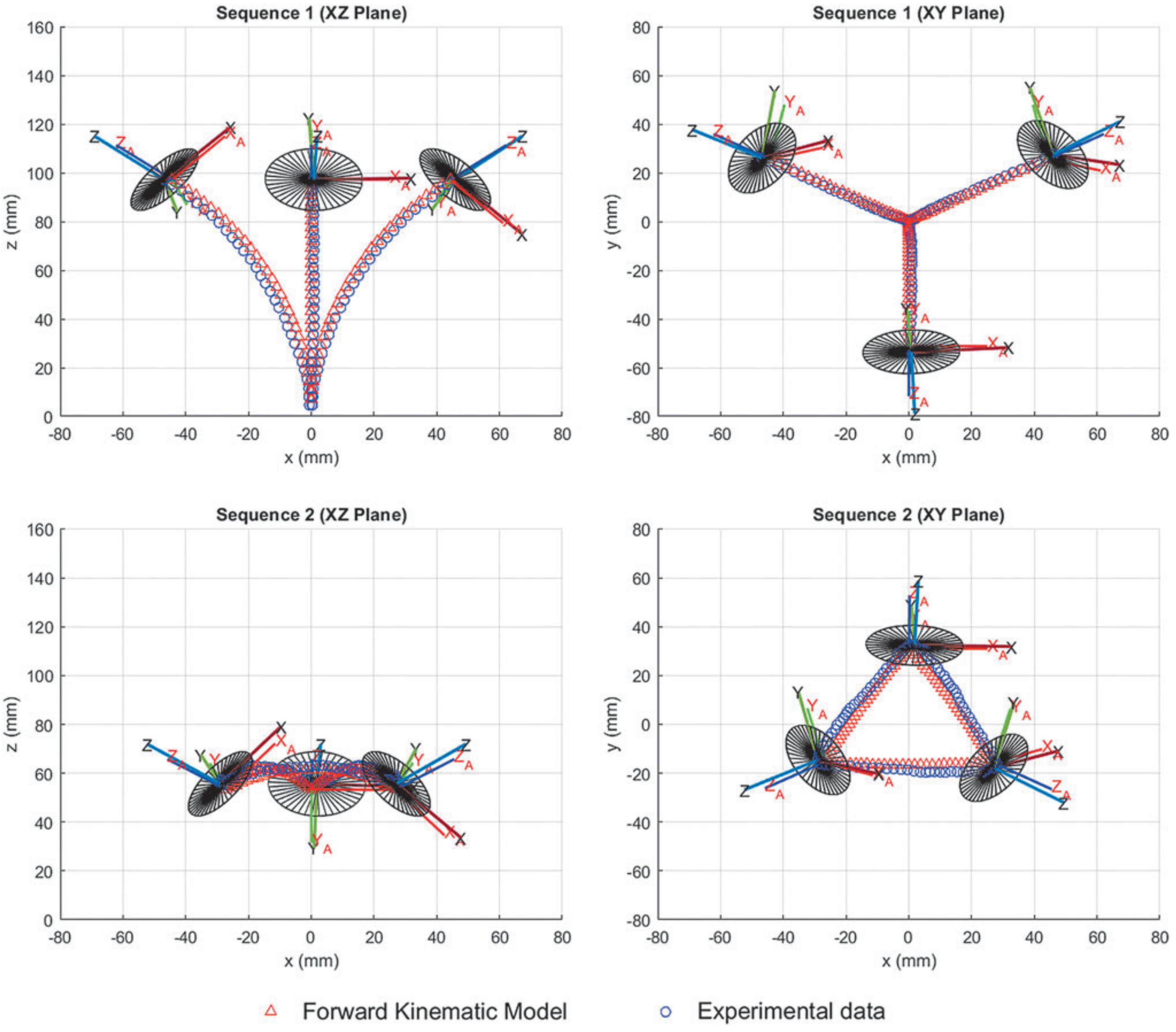

FIG. 8. Forward kinematics comparison for two different sequences. The XYZ frame represents the observed orientation of the disk, whereas X_A Y_A Z_A represents the resulting values obtained by the implemented forward kinematic model.

Table 4. Position Estimation Using the Forward Kinematic Model for the Evaluation Sequences

		Sequence 1			*Sequence 2*		
	Units	*X*	*Y*	*Z*	*X*	*Y*	*Z*
Max error	mm	2.76	2.72	3.13	4.00	3.87	2.87
MAE	mm	1.07	1.00	1.66	1.73	1.74	1.56
RMSE	mm	1.27	1.27	1.91	1.99	1.99	1.62

$$\mathrm{T}_i(r,\theta,\phi) = \begin{bmatrix} c_\phi^2 c_\theta + s_\phi^2 & c_\phi s_\phi (c_\theta - 1) & c_\phi s_\theta & r c_\phi (1 - c_\theta) \\ c_\phi s_\phi (c_\theta - 1) & s_\phi^2 c_\theta + c_\phi^2 & s_\phi s_\theta & r s_\phi (1 - c_\theta) \\ -c_\phi s_\theta & -s_\phi s_\theta & c_\theta & r s_\theta \\ 0 & 0 & 0 & 1 \end{bmatrix} \tag{7b}$$

Once the homogeneous transformation of the arm section is completely defined, the arm tip pose is determined by repeating the same procedure for the second section and multiplying the resulting homogeneous transformation matrices. Because independent untangled bending between sections is being considered, the rack length for the second section, that is, the distal section, needs to be calculated by subtracting its first section rack pair.

$$\vec{\mathrm{X}} = \mathrm{T}(r_1, \theta_1, \phi_1)\ \mathrm{T}(r_2, \theta_2, \phi_2) \tag{8}$$

$$l_{i,j} = l_{i,j} - l_{i,j-1} \tag{9}$$

Inverse kinematics

A data-driven approach based on machine learning algorithms is implemented to solve the inverse kinematics. This approach surpasses other iterative and model-based approaches by providing a faster and more adaptable solution. The modeling process is presented in two stages: data capture and network model selection.

Data capture. To capture arm data to train the networks, a test platform (Fig. 7B) was built with an integrated RGB camera at a fixed height to capture the pose of the arm tip, where a single ArUco marker was fixed, as shown in Figure 7A. Using the ArUco library,[23] the position and orientation of the marker are given as a translation vector in meters and a 3D rotation vector in radians, respectively. However, the orientation vector was converted to a quaternion form to reduce the number of variables and to optimize the computing speed for the learning process.

A routine was programmed in which motor babbling is given as an input for each servomotor with respect to the limits of the racks that are attached to them and the relationship that must be maintained between the racks that control each section. After the arm tip reaches the resulting position, the motor input values are recorded, and five captures of the ArUco code located at the tip of the arm are taken, averaged, and converted to their corresponding representation for position and orientation. Considering that the camera's field of view was limited to one third of the arm workspace, a data augmentation procedure was implemented. Since the arm has radial symmetry, the remaining positions were obtained through a ±120° rotation around the z-axis of the base and an inverse rotation with respect to the z-axis of the tip of the arm to compensate for the inability of the arm to rotate on its own axis. This process was repeated until a total of 10,503 different positions were obtained. It is worth noting that during the data capture procedure, neither gravity nor weight effects were considered since the experimental setup has the z-axis oriented upward, as shown in Figure 7B.

The resulting points that represent the arm workspace are presented in Figure 7C, where each point represents the midpoint of the arm tip. Table 2 presents the safe operating range of the arm without separation, taking into account the limitations imposed by the robot's length of 180 mm.

Network model selection. A comparative study was conducted to select the model that balances computational cost and accuracy. Three commonly used architectures, ELM, KNNR, and MLP, were considered based on previous studies.[24] ELM is a single-layer feedforward neural network with randomly assigned hidden-layer weights and learned output-layer weights.[25] The number of nodes in the hidden layer is a specified hyperparameter. KNNR is a nonparametric algorithm that finds the K-nearest neighbors using a distance metric and predicts based on their average.[26] The number of neighbors K is a specified hyperparameter. MLP is an artificial neural network with learned weights in its connections between input, hidden, and output layers.[27] The number of layers and nodes in each layer are specified hyperparameters.

Before comparing the algorithms, a sensitivity analysis determined the best-performing models for each algorithm, considering prediction time and accuracy using mean absolute error (MAE) and root mean squared error (RMSE) as evaluation metrics. The data captured at the arm tip was divided into training (80%) and test (20%) sets, and the processes were conducted on a 1.8 GHz AMD Ryzen 7 5700U with 16 GB RAM running a Python script.

Observing the results in Table 3, it was decided to use an ELM network to solve the arm inverse kinematics model due to its favorable time/performance ratio. With an average prediction time of 24.4 ms, the ELM network had a single hidden layer with 150 neurons using a hyperbolic tangent sigmoid transfer function. The input is the arm tip pose with the orientation of the end effector represented in quaternion

Table 5. Orientation Estimation Using the Forward Kinematic Model for the Evaluation Sequences

		Sequence 1			*Sequence 2*		
	Units	*Min*	*Mean*	*Max*	*Min*	*Mean*	*Max*
Angle $(\mathrm{W}, \mathrm{W}_{\mathrm{pred}})_{\max}$	deg	1.3115	2.3584	3.6857	1.2689	2.2516	4.3069
Dot $(\mathrm{W}, \mathrm{W}_{\mathrm{pred}})_{\min}$	—	0.9995	0.9998	—	0.9993	0.9998	—

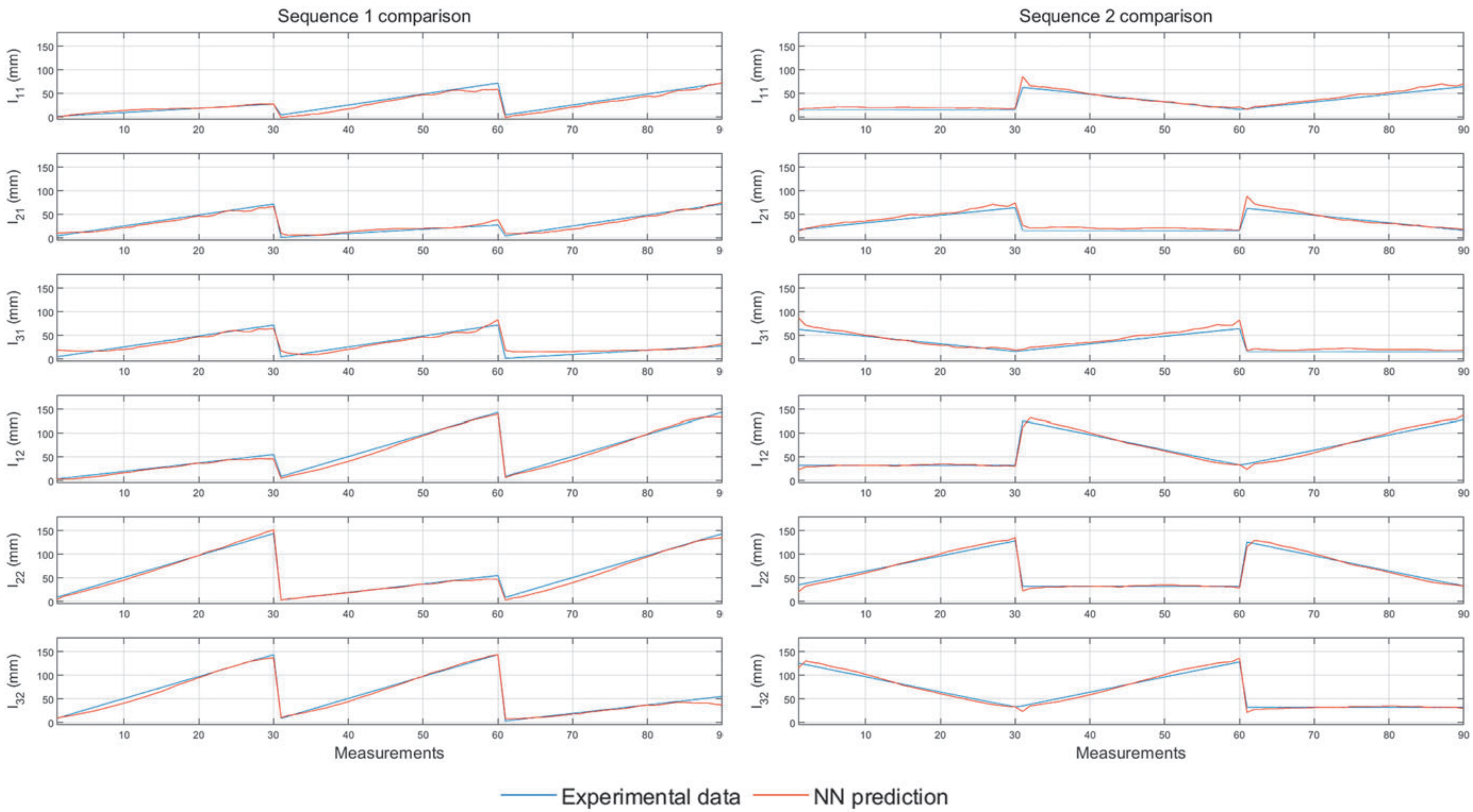

FIG. 9. Comparison graph for the inverse kinematic model based on a single-layer extreme learning machine network for two different evaluation sequences. l_{11}–l_{31} represent the rack extension for the first section and l_{12}–l_{32} for the second section. NN, neural network.

Table 6. Performance of the Inverse Kinematic Model in the Evaluation Sequences

		Sequence 1			*Sequence 2*		
	Rack extension	*Max error (mm)*	*MAE (mm)*	*RMSE (mm)*	*Max error (mm)*	*MAE (mm)*	*RMSE (mm)*
Section 1	l_1	12.95	4.18	5.07	22.80	3.57	4.59
	l_2	11.46	3.43	4.04	25.70	4.51	5.64
	l_3	16.96	4.57	5.72	24.84	4.69	5.88
Section 2	l_1	10.61	4.04	4.94	12.99	3.65	4.71
	l_2	11.12	3.81	5.06	14.82	3.62	4.54
	l_3	18.24	3.68	5.06	11.82	3.78	4.66

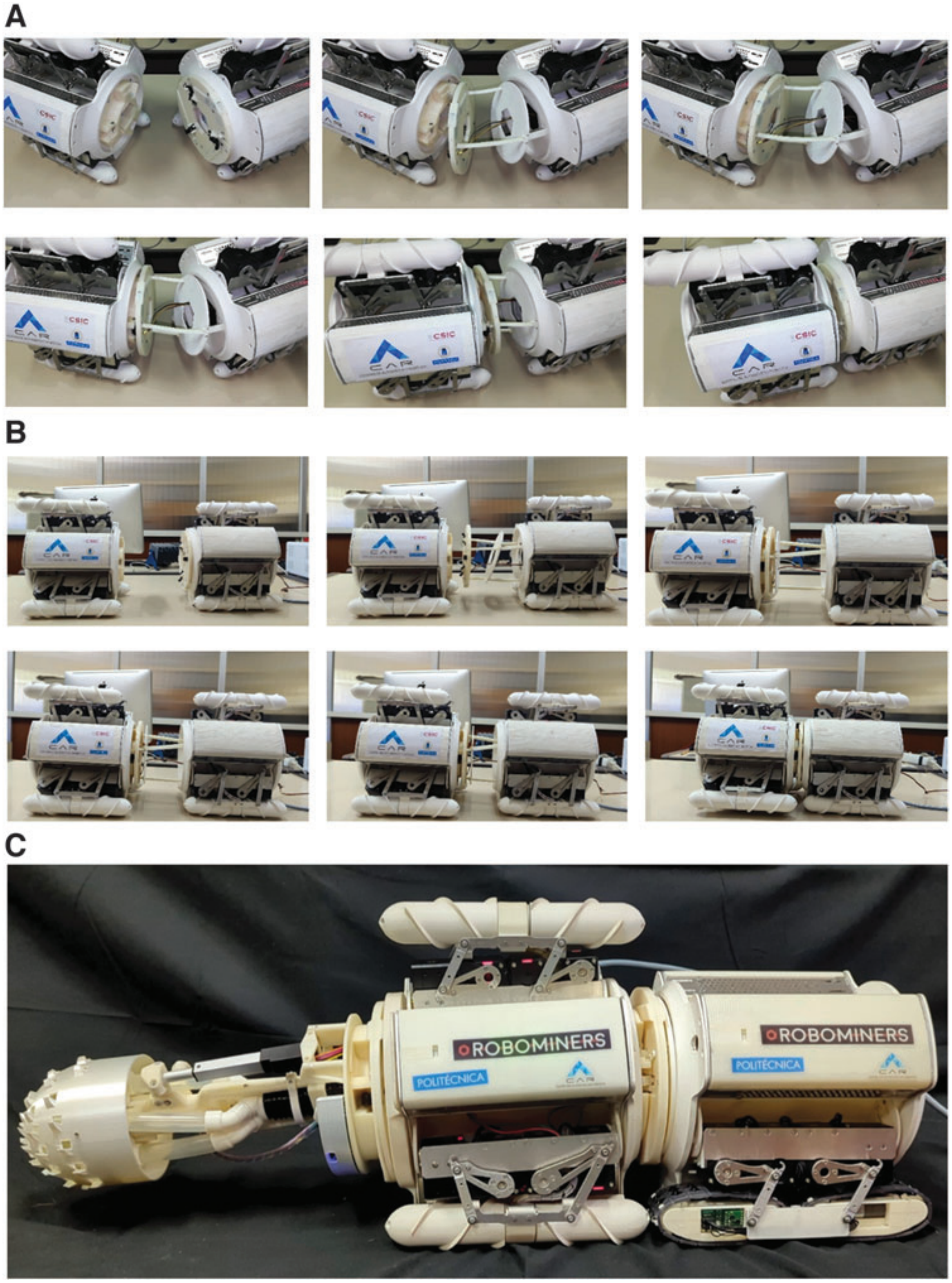

FIG. 10. **(A)** Continuum arm guided maneuver based on a curved trajectory to join two robotic modules together. **(B)** Continuum arm guided maneuver based on a straight trajectory to join two robotic modules together. **(C)** Robotic system composed of two robotic modules and a cutting head submodule.

form, and the output is the rack extension of each rack controlling the two sections of the arm.

Results and Discussion

Two different sequences were designed to test and validate both forward and inverse kinematic models. Each sequence is based on a maneuver repeated three times with different orientations at the base of the robot, where a total of 90 points that are contained in the robot workspace are evaluated. The first sequence represents the extension and bending of the arm from the home position, where the arm is retracted into the robot, to a desired final pose. The second sequence consists of a triangular trajectory at a fixed height.

Figure 8 shows the path followed by the arm tip and the prediction calculated using the forward kinematics model for both sequences. For position estimation, the maximum, average, and RMSEs are shown in Table 4. Then, to compare orientation in quaternion form, two metrics were considered. First, we calculate the dot product of the quaternions, which will be 1 if the quaternions are equivalent and –1 if they are negations of each other. If the dot product is 1, the quaternions represent the same orientation. In addition, we determine the minimum rotation angle that would be required to convert one quaternion to the other.

Analyzing the results from Table 4 and Figure 8, we observe that the model accurately predicts the position of the arm tip for the different points in the two sequences, with a maximum error lower than 4 mm and a deviation close to 2 mm. For orientation, Table 5 shows that the maximum rotation angle is 3.69° and 4.31°, and the minimum dot product of the quaternions is 0.9995 and 0.9993 for each sequence, respectively. Therefore, we can ensure that the orientation determined by the model is accurate and can be observed qualitatively in Figure 8, where the calculated orientation is quite close to the experimental measurements, with little to no deviation for the sequences tested.

On the contrary, for the inverse kinematic model, we evaluate the prediction of the ELM to observe how well it generalizes for new data, using the same recorded sequences as for the forward kinematics, but this time using the pose of the arm tip as inputs and the rack extensions as outputs. Looking at Figure 9 and Table 6, we observe that the model is capable of predicting the rack extension of both sections effectively with a maximum overall error of 18.24 mm for the first sequence and 25.7 mm for the second sequence. The MAE for both sequences is lower than 5 mm and the maximum RMSE is lower than 6 mm. It is worth noting that the accuracy of the prediction varies for each section, where the second section's rack generally presents a lower error than the first section for both evaluation sequences. In addition, the error is also affected by the effects of gravity and the weight of the arm, which were not considered in the modeling stage as commented in previous sections. However, the obtained results guarantee that the arm reaches the desired target with an acceptable range to successfully perform the coupling maneuver.

Implementation

Using the kinematics of the arm, coupling maneuvers have been performed to demonstrate the function and capabilities of the arm. Figure 10 shows an example of two different trajectories. In both maneuvers, the arm is guided into the docking port of the robotic module by bending and extending the sections. Next, it secures the module by performing the docking procedure described in previous sections and finally retracts the arm to complete the coupling between the modules. Considering that the weight of a robotic module is 4.5 kg, the arm demonstrates the high mass-pulling capabilities required, as well as the bending and extending capabilities. In Figure 10C, a potential arrangement of the robotic system is presented, where two different modules and a cutting head submodule are integrated. This integration yields a larger robot capable of exerting increased drilling force capacities. Both coupling maneuvers, as well as a demonstration of the arm's range of motion and docking mechanism, can be seen in the Supplementary Video S1.

Conclusions

In this work, we introduced a soft continuum arm featuring extensible sections capable of independent extension and bending. The arm is extrinsically actuated using a configuration of servomotors that drive flexible racks via a rack-and-pinion mechanism. The entire arm structure is fully 3D printed, utilizing PLA for section disks and TPU 95A for flexible racks.

Integrated into a modular robot, the arm serves as a mechanical interface that allows the docking of other robotic modules or tools. This is made possible by the docking interface incorporated into the arm's end effector. The docking mechanism is based on the car crane principle, where the arm reaches the docking port, secures the robotic module/submodule, and subsequently retracts, pulling the arm back into the robotic module.

To address the arm's kinematics, we employed both analytical and data-driven approaches. The forward kinematics was solved by implementing a constant curvature model with untangled independent bending between the sections. For the inverse kinematics, a machine learning algorithm was utilized.

Experimental validation was conducted for both kinematic models, achieving satisfactory results concerning position and orientation errors. The forward kinematics presented maximum position errors below 4 mm and an overall maximum rotation angle difference of 4.31°, confirming the accuracy of the predictions and validating the assumption that the arm's virtual backbone follows a quasi-constant curvature. Regarding the inverse kinematics model, the maximum error in rack extension was measured at 18.24 mm for the first sequence and 25.7 mm for the second sequence. The overall MAE and RMSE were found to be 4.69 and 5.88 mm, respectively. These results indicate a good prediction of the required extension for achieving the desired position and ensuring proper arm functionality. The errors primarily originate from nonlinearities resulting from irregular arm bending, as well as the influence of gravity and weight effects that were not considered in the kinematic modeling phase.

To validate the effectiveness of the proposed design and kinematic models, two different maneuvers were performed, demonstrating successful reaching and assembly capabilities.

Further developments can be made for enhancing the arm functionality, such as optimizing the design of the driving mechanism and increasing the number of racks to increase its stability and robustness by augmenting the change of stiffness of the arm. Future applications of this arm include the possibility of coupling different sensing and actuation modules such as active sensing devices or other measurement devices such as geophysical sensors that need to be precisely placed on the rock face.

Authors' Contributions

V.G.: Conceptualization (supporting), methodology (lead), formal analysis (lead), software (lead), investigation (supporting), validation (lead), writing—original draft (lead), review and editing (equal). M.H.: Conceptualization (lead), methodology (supporting), formal analysis (equal), writing—original draft (supporting), writing—review and editing (lead), supervision (lead). E.A.: Formal analysis (supporting), investigation (supporting), validation (equal), writing—review and editing (equal). D.B.: Conceptualization (supporting), software (equal), investigation (lead). C.R.: Writing—review and editing (equal), supervision (equal), funding acquisition (lead).

Author Disclosure Statement

No competing financial interests exist.

Funding Information

This research was supported by the European Commission Horizon 2020 Research and Innovation Program (ROBOMINERS, Grant No. 820971).

Supplementary Material

Supplementary Video S1

References

1. Zhang K, Kang L, Chen X, et al. A review of intelligent unmanned mining current situation and development trend. Energies 2022;15(2):513.
2. Dinelli C, Racette J, Escarcega M, et al. Configurations and applications of multi-agent hybrid drone/unmanned ground vehicle for underground environments: A review. Drones 2023;7(2):136.
3. Gomez V. Hernando M. Modular collaborative resilient robots for mining operations. EGU General Assembly 2022, Vienna, Austria, 23–27 May 2022, EGU22–2740; 2022; doi: 10.5194/egusphere-egu22-2740.
4. Saab W, Racioppo P, Ben-Tzvi P. A review of coupling mechanism designs for modular reconfigurable robots. Robotica 2019;37(2):378–403.
5. Qin G, Ji A, Cheng Y, et al. A snake-inspired layer-driven continuum robot. Soft Robot 2022;9(4):788–797.
6. Walker ID. Continuous Backbone ‘‘Continuum'' Robot Manipulators. ISRN Robot 2013;2013:1–19.
7. Matsuda R, Mavinkurve U, Kanada A, et al. A woodpecker's tongue-inspired, bendable and extendable robot manipulator with structural stiffness. IEEE Robot Autom Lett 2022;7(2):3334–3341.
8. Kanada A, Mashimo T. Mobile continuum robot with unlimited extensible sections. In: 2018 IEEE/RSJ International Conference on Intelligent Robots and Systems (IROS) Madrid, Spain; 2018; pp. 7117–7122; doi: 10.1109/IROS.2018.8594340.
9. Al-Ibadi A, Nefti-Meziani S, Davis S. Design, kinematics and controlling a novel soft robot arm with parallel motion. Robotics 2018;7(2):19.
10. Kim S, Laschi C, Trimmer B. Soft robotics: A bioinspired evolution in robotics. Trends Biotechnol 2013;31(5):287–294.
11. Giordano G, Carlotti M, Mazzolai B. A perspective on cephalopods mimicry and bioinspired technologies toward proprioceptive autonomous soft robots. Adv Mater Technol 2021;6(12):2100437.
12. Li S, Hao G. Current trends and prospects in compliant continuum robots: A survey. Actuators 2021;10(7):145.
13. Dou W, Zhong G, Cao J, et al. Soft robotic manipulators: Designs, actuation, stiffness tuning, and sensing. Adv Mater Technol 2021;6:2100018; doi: 10.1002/admt.202100018.
14. Marechal L, Balland P, Lindenroth L, et al. Toward a common framework and database of materials for soft robotics. Soft Robot 2021;8(3):284–297.
15. El-Atab N, Mishra RB, Al-Modaf F, et al. Soft actuators for soft robotic applications: A review. Adv Intell Syst 2020; 2(10):2000128.
16. Wallin TJ, Pikul J, Shepherd RF. 3D printing of soft robotic systems. Nat Rev Mater 2018;3:84–100; doi: 10.1038/s41578-018-0002-2.
17. Hernando M, Bajo D, Gomez V, et al. Mechanical actuation system for a soft robotic arm. ES2907801 (Patent) 2022.
18. George Thuruthel T, Falotico E, Manti M, et al. Learning closed loop kinematic controllers for continuum manipulators in unstructured environments. Soft Robot 2017;4(3):285–296.
19. George Thuruthel T, Ansari Y, Falotico E, Laschi C. Control strategies for soft robotic manipulators: A survey. Soft Robot 2018;5(2):149–163.
20. Rao P, Peyron Q, Lilge S, Burgner-Kahrs J. How to model tendon-driven continuum robots and benchmark modelling performance. Front Robot AI 2021;7:630245.
21. Xu W, Chen J, Lau HYK, Ren H. Data-driven methods towards learning the highly nonlinear inverse kinematics of tendon-driven surgical manipulators. Int J Med Robot 2017;13(3):e1774.
22. Webster RJ, Jones BA. Design and kinematic modeling of constant curvature continuum robots: A review. Int J Robot Res 2010;29(13):1661–1683.
23. Garrido-Jurado S, Muñoz-Salinas R, Madrid-Cuevas FJ, Marín-Jiménez MJ. Automatic generation and detection of highly reliable fiducial markers under occlusion. Pattern Recogn 2014;47(6):2280–2292.
24. Wang X, Li Y, Kwok KW. A survey for machine learning-based control of continuum robots. Front Robot AI 2021;8: 730330.
25. Huang GB, Zhu QY, Siew CK. Extreme learning machine: Theory and applications. Neurocomputing 2006;70(1–3): 489–501.
26. Kramer O. Dimensionality Reduction with Unsupervised Nearest Neighbors. Intelligent Systems Reference Library, Volume 51. Springer Berlin Heidelberg: Berlin, Heidelberg; 2013.
27. Haykin SS, Haykin SS. Neural Networks and Learning Machines, 3rd ed. Prentice Hall: New York, NY, USA; 2009; p. 906.

Address correspondence to:
Virgilio Gomez
Centre for Automation and Robotics UPM-CSIC
Universidad Politécnica de Madrid
Madrid 28006
Spain

E-mail: virgilio.gomez.lambo@upm.es

Publication III

Gomez, V., Remmas, W., Hernando, M., Ristolainen, A., Rossi, C., *"Bioinspired Whisker sensor for 3D mapping of underground mining environments,"* Biomimetics 2024, 9, 83. doi:10.3390/biomimetics9020083.

biomimetics

MDPI

Article

Bioinspired Whisker Sensor for 3D Mapping of Underground Mining Environments

Virgilio Gomez [1,*], Walid Remmas [2], Miguel Hernando [1], Asko Ristolainen [2] and Claudio Rossi [1]

[1] Centre for Automation and Robotics, Universidad Politécnica de Madrid—CSIC, 28006 Madrid, Spain; miguel.hernando@upm.es (M.H.); claudio.rossi@upm.es (C.R.)
[2] Centre for Biorobotics, Department of Computer Systems, School of Information Technologies, Tallinn University of Technology, 12618 Tallinn, Estonia; walid.remmas@taltech.ee (W.R.); asko.ristolainen@taltech.ee (A.R.)
* Corrrespondence: virgilio.gomez.lambo@upm.es

Abstract: Traversing through challenging, unstructured environments, particularly in mining scenarios characterized by dust concentration, darkness, and lack of communication presents formidable obstacles for traditional sensing technologies. Drawing inspiration from naked mole rats, characterized as being skilled subterranean navigators that depend heavily on touch to navigate their environment, this study introduces a new whisker-sensing disk designed for 3D mapping in unstructured environments. The disk comprises a circular array of 32 whisker sensors, each featuring a slender flexible plastic rod attached to a compliant base housing a 3D Hall-effect sensor. The whisker sensor is modeled using both analytical and data-driven approaches to predict rotation angles based on magnetic field measurements. The validation and comparison of both models are performed by evaluating data from other whisker sensors. Additionally, a series of experiments demonstrates the whisker disk's capability in performing 3D-mapping tasks, along with successful implementation on diverse robotic platforms, highlighting its future potential for effective 3D mapping in complex and unstructured subterranean environments.

Keywords: whisker sensor; 3D mapping; bioinspired design

check for updates

Citation: Gomez, V.; Remmas, W.; Hernando, M., Ristolainen, A.; Rossi, C. Bioinspired Whisker sensor for 3D mapping of underground mining environments . *Biomimetics* **2024**, *9*, 83. https://doi.org/10.3390/biomimetics9020083

Academic Editors: Swaminath Venkateswaran, Damien Chablat, Poramate Manoonpong and Julien R Serres

Received: 31 December 2023
Revised: 24 January 2024
Accepted: 29 January 2024
Published: 31 January 2024

1. Introduction

Navigating unstructured environments poses formidable challenges for autonomous robots, as they struggle with complexities, such as clutter, unpredictable terrain, and the limitations of traditional mapping technologies. This is particularly prevalent in mining environments, known for their extreme and unstructured nature, where dust concentrations and darkness create additional hurdles for traditional localization, sensing, and mapping methods that rely on Global Positioning Systems (GPS), cameras, and Light Detection and Ranging (LiDAR) systems [1]. Recognizing the need for innovative solutions, the development of alternative sensory approaches becomes critical for robots tasked with mapping and navigating these cluttered and difficult-to-access environments [2]. A promising approach involves the use of touch-based sensors to map the surface of the mine, with bioinspired mammalian sensors emerging as a viable alternative due to their demonstrated robustness, simplicity, and precision [3]. The versatility of such sensors is evident in their application for various purposes, ranging from object localization [4–6], contour and texture recognition [3,7,8], and even fluid flow direction and viscosity [9–11]. With particular emphasis on robot navigation and mapping, the integration of active and passive whiskers into the structure of mobile robots and robot manipulators [12–16] has shown great potential for obstacle avoidance and Simultaneous Localization and Mapping (SLAM) tasks [17,18]. However, not much effort has been put into point cloud generation for environment reconstruction. Mapping 3D spaces presents additional complications, as whisker-based sensors need to navigate and interpret spatial information effectively. Factors such as environmental variability, surface textures, and the need for real-time adaptability contribute to the intricacies faced in developing robust models for whisker-based sensors in 3D-mapping applications.

The ROBOMINERS project [1] strategically focuses on introducing innovative robotic concepts to overcome these challenges and improve mineral access in Europe, thus reshaping the mining ecosystem. A crucial objective is to enable robots to navigate and execute selective mining procedures by equipping them with the capability to map mining environments and dynamically adjust their paths for optimized mineral extraction. To address this challenge, prototypes that incorporate various alternative sensor technologies are currently in development and are undergoing testing. These prototypes explore a spectrum of options, from spectrometry-based sensors [19] to contact-based sensors. Drawing inspiration from the remarkable tactile abilities of the naked mole rat, a notable rodent species renowned for its navigation and contact detection capabilities in subterranean environments (Figure 1a) [20], an autonomous robotic miner (Figure 1c) could navigate challenging environments, addressing complex issues such as executing mining procedures and precise 3D-mapping tasks and navigating in subterranean areas [21]. Similar to the naked mole rat, which is heavily dependent on its somatosensory systems (touch) [22] and uses a series of sensitive sensory hairs to orient itself and navigate subterranean landscapes (Figure 1b), the robotic miner strives to replicate the efficiency of nature in overcoming obstacles in its quest for optimal performance and adaptability.

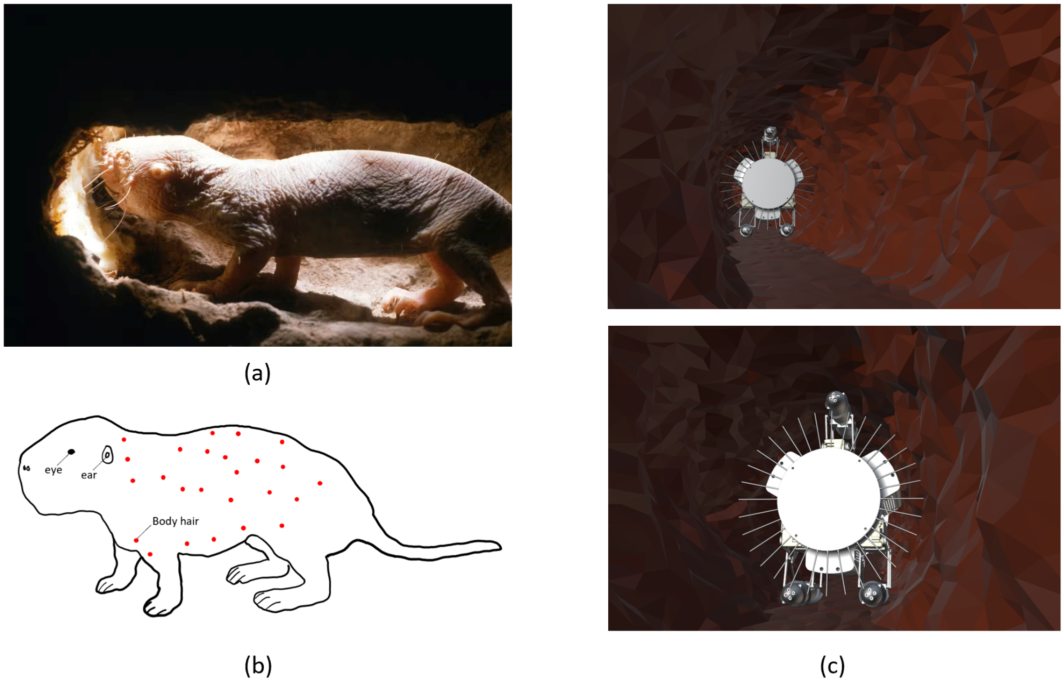

Figure 1. (**a**) Naked mole rat in subterranean environments (Picture taken by Neil Bromhall, Shutterstock). (**b**) Body hair location for an adult naked mole rat. Each body hair is represented by a small red dot. This rodent presents a systematic array of sensitive sensory hairs on its body, as described in [23], that help it navigate and orient itself in lightless subterranean environments. (**c**) Concept of robotic miner equipped with touch based sensor for navigation and mapping of unstructured 3D environments.

This study introduces a novel whisker-based disk that uses 3D Hall-effect sensors to map 3D unstructured environments. The disk design tries to approximate a section of the mole rat body, where the sensory hairs are approximately distributed in a ring-like pattern across the whole body. Compared to other designs, the whisker is housed in a non-permanent manner to the silicone rings, and the magnet holder features a spherical joint that serves as the pivot point to transmit the rotational movement of the whisker. The whisker is modeled following both analytical and data-driven approaches to determine the rotational angles of the whiskers, given the magnetic field felt by the sensor when the whisker makes contact with an object. In this paper, the whisker disk is installed on a serial manipulator to demonstrate the mapping of 3D surfaces. Furthermore, the design can be attached to a scaled-down robotic miner to give the robot the capability to map 3D environments during operation.

This article is structured as follows. In Section 2, we introduce the design and manufacturing process of the sensor. In Section 3, we present an approximation of an analytical model of the phenomena and propose an alternative sensor model based on a data-driven approach. In Section 4, we perform different experiments to compare and validate the rotational models presented. In Section 5, we carry out 3D-mapping experiments using the serial manipulator and showcase the adaptability of the presented solution to other robotic platforms. Finally, in Section 6, we draw conclusions from the results obtained in the study.

2. Sensor Design and Manufacture Process

The prototype presented (Figure 2a) is based on a circular array of 32 whiskers that can be attached to different robots to map non-structured environments. The main component of the disk is the whisker sensor, composed of a slender flexible polystyrene rod that is inserted at one end into a 3D-printed part called a "magnet holder", where a neodymium permanent magnet is affixed to the opposite end of this piece. The magnet possesses axial magnetization, aligning its magnetic field with the Hall effect sensor's x-axis. The magnet holder features a spherical contact that is housed inside a silicone structure composed of two rings that are attached to the disk, as shown in Figure 2b. The dimensions of the sphere are slightly larger with respect to the silicone structure to ensure the restriction of the magnet holder inside the rings. The silicone structure allows the magnet holder to rotate in two planes as the whisker makes contact with a surface.

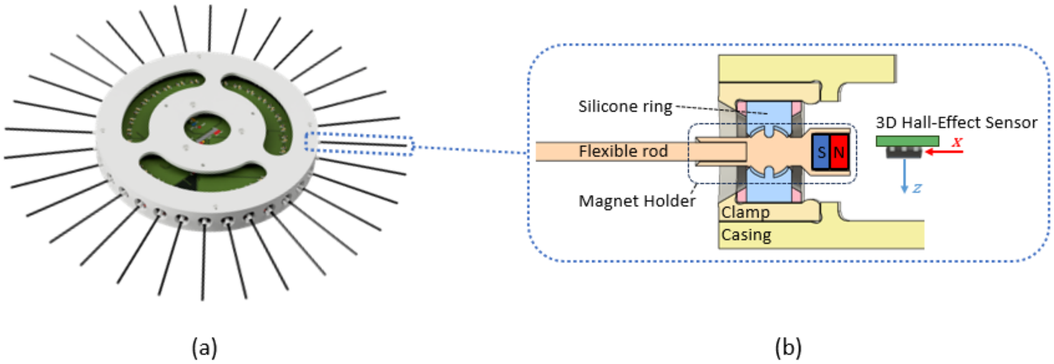

Figure 2. Whisker disk prototype. (**a**) The sensor comprises a circular array of 32 whiskers. (**b**) Detailed section view of a single whisker sensor.

Sensor Manufacturing Process

The whisker disk pieces were manufactured using a combination of fused deposition modeling (FDM) and stereolithography (SLA) printing. The disk structure was printed using an industrial grade FDM printer (Stratasys, Dimension Elite), while the molds for the inner cavity of the silicone structure and the magnet holder were printed with a high resolution SLA printer (Formlabs Form 3B) with a layer thickness of 50 µm.

To manufacture the silicone rings, we first prepared the mold pieces by applying a silicone release agent and secured them with a set of screws. During the mixing procedure, the silicone mixture (Zhermack Elite double 22) underwent a two-minute vacuum treatment to eliminate any potential bubble formation. Following degassing, the mixture was carefully injected into the mold. Finally, to guarantee the absence of bubbles within the silicone structure, the mold was reintroduced into the vacuum chamber and pressurized throughout the rest of the curing process. This step was repeated for the upper ring, ensuring uniformity and structural integrity.

Finally, to assemble the whisker disk (Figure 3), we first clamped the two rings with their respective silicone structure and secured the structure inside the casing that comprises the disk with a set of screws. To assemble the magnet holder, we glued the magnets to the rear part and attached the rods to the front part. The magnets used were N52 grade 4mm cylindrical neodymium magnets. The rods selected were 2 mm polystyrene rods. The magnet holder was then inserted into the silicone rings until the spherical housing occupied the silicone cavity. Lastly, a Printed Circuit Board (PCB) disk was installed where the Hall-effect sensors are mounted, ensuring that the corresponding sensor's X-axis was collinear to each whisker. It should be noted that since the presented prototype is made up of 32 whiskers and the selected Hall-effect sensors do not have enough configurable addresses, it was necessary to include four Inter-Integrated Circuit (I2C) multiplexors (PCA9548AD) in the PCB.

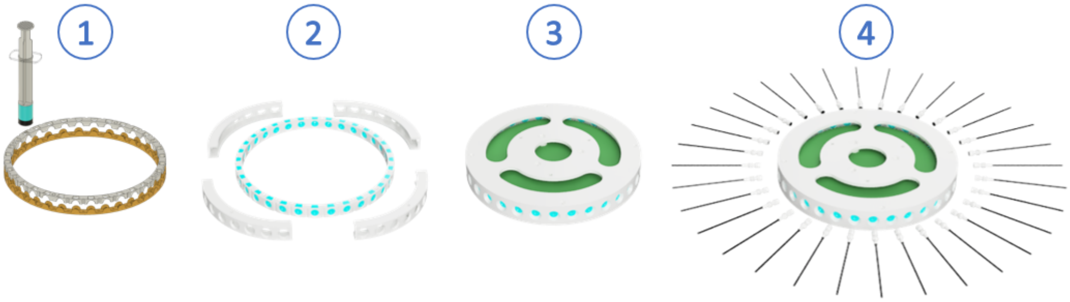

Figure 3. Whisker disk assembly procedure. First, the silicone base is prepared by injecting the mixture into the plastic rings. Next, the silicone rings are clamped and assembled into the disk structure with a set of screws. Finally, the PCB is installed, and the whiskers are inserted through the silicone ring until the spherical contact reaches its position.

3. Sensor Modeling

In order to determine the sensor model that correctly maps sensor measurements, (B_x, B_y, B_z) to rotation angles (θ_y, θ_z), we performed a comprehensive modeling procedure employing analytical and data-driven methodologies.

To collect the necessary data to train and validate both models, we designed and built a test platform featuring a Universal Robot (UR) UR3e manipulator. The manipulator gripped a single whisker at its tip and performed randomized movements within its workspace. The setup is presented in Figure 4, where the sequence of movements is based on performing pure rotations with respect to the pivot point of the whisker for both angles. Throughout this process, both the robot's rotation angles with respect to the whisker and the sensor measurements for each position were recorded. A demonstration of the data capture process is available in the Supplementary Video S1.

The whisker workspace was determined by establishing rotational limits for both possible angles, followed by generating a meshgrid that encompassed all attainable positions. To facilitate movement to these positions, a Python script was written using UR's RTDE python client library [24]. To read the sensor output, a microcontroller was utilized by running an Arduino routine that averaged the first 16 measurements and, upon request from the Python script, printed the averaged sensor data.

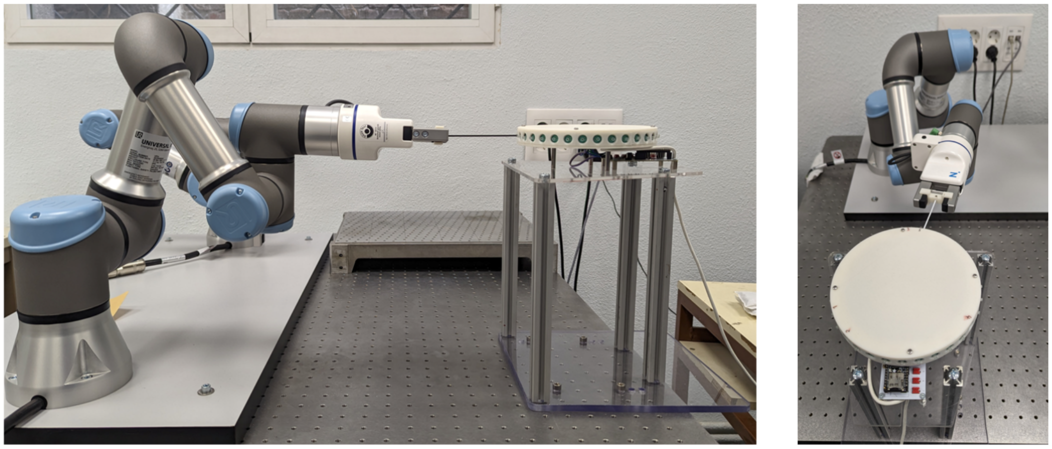

Figure 4. Testbed to capture whisker sensor data featuring a UR3e serial manipulator.

3.1. Whisker Rotation Model

To model the expected rotation of the whisker, given the magnetic field measurements, we considered the relationships provided by the manufacturer to estimate the linear and rotational movements of the magnet, considering an approximation of the relationship between the magnetic fluxes of each axis and the orientation of the magnet [25]. The description of the proposed model and references is presented in Figure 5, where the angles θ_y and θ_z represent the rotation on the y and z axes, O represents the pivot point, M is the center point of the magnet, and S is the center of the sensitive area of the sensor.

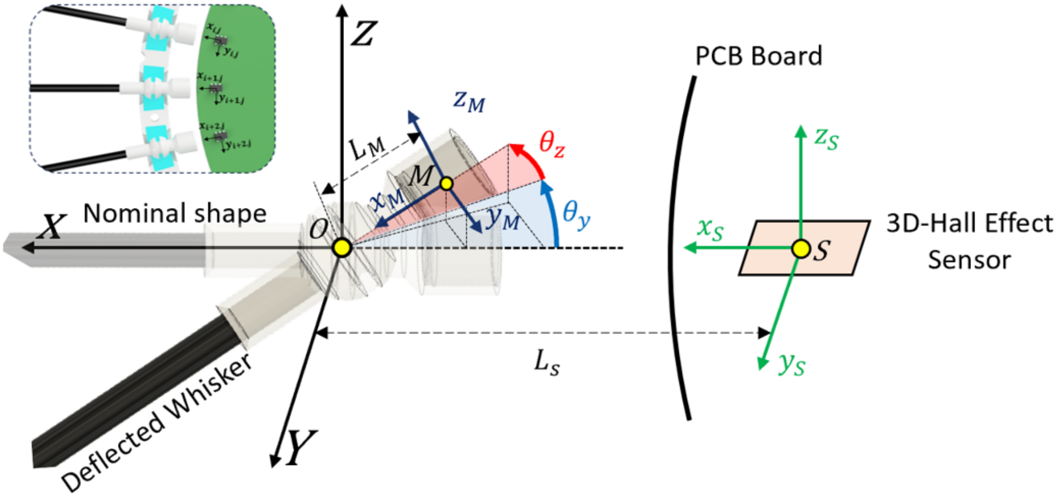

Figure 5. Whisker sensor rotational model description. The whisker can rotate in two different angles from the pivotal point generating the change in the position and orientation of the magnet and therefore of the magnetic field felt by the Hall-effect sensor.

The magnet position can be estimated considering the approximation presented in (1–3), where $\vec{B}$ represents the magnetic flux vector measured by the sensor, and sc_{θ_y}, b_{θ_z}, b_{θ_y} and b_{θ_z} represent the scaling and bias factors for both bending angles, respectively. Both scaling factors and biases are adjusted based on experimental data. It is worth noting that both the earth's magnetic field and neighboring magnets can affect the magnetic flux of the sensor, therefore changing the estimation of the magnet position. However, these effects resulted in a relatively small impact and were excluded from the model.

$$\vec{B} = \left\{ B_x \quad B_y \quad B_z \right\} \tag{1}$$

$$\theta_z = \frac{atan2\left(B_y, B_x\right)}{sc_{\theta_z}} - b_{\theta_z} \tag{2}$$

$$\theta_y = -\frac{atan2\left(B_z, \sqrt{B_x^2 + B_y^2}\right)}{sc_{\theta_y}} - b_{\theta_y} \tag{3}$$

Once the rotation angles are calculated, assuming that the point of contact between the whisker and the surface occurs at the tip of the whisker, we can determine an approximate location of the surface point. It should be noted that the error resulting from this consideration is acceptable for a mining scenario, where the whisker length with respect to the overall size of the robot is relatively small.

Data-Driven Approach

We decided to implement a data-driven approach based on machine learning algorithms to account for the nonlinearity, variability, and inconsistencies derived from the whisker sensor manufacturing process. This approach allows us to provide a more adaptable solution, with the drawback of reducing the explainability of the model.

To select the algorithm that best combines computational cost and accuracy, we carried out a comparative study. Four state-of-the-art algorithms, Extreme Learning Machine (ELM), Multilayer Perceptron (MLP), Support Vector Regressor (SVR), and K-Nearest Neighbors Regressor (KNN-R) were considered based on previous experience. ELM and MLP are both neural network architectures, but ELM is known for its simplicity and rapid training [26], while MLP typically involves deeper architectures and backpropagation [27]. SVR is based on the principles of support vector machines, where the model learns the importance of a variable to characterize the relationship between input and output [28]. The aim is to find a hyperplane that best fits the data, considering a margin around the predicted values. KNN-R is a non-neural network method that relies on instance similarity [29].

To compare the algorithms, a sensitivity analysis was performed first to identify the models that perform the best for each algorithm. The prediction time and precision were evaluated using the mean absolute error (MAE) and the root mean square error (RMSE) as the main comparison metrics. A total of 900 points were recorded for a single whisker, where the rotations for both angles varied between -20° and 20°. The data were divided in an 85/15 split for training/testing sets, and the algorithms were run on a 1.8 GHz AMD Ryzen 7 5700U computer with 16 GB RAM, running a Python script.

Observing the results in Table 1, it can be seen that the best balance between the computational cost and precision is obtained by the ELM. The four models are capable of predicting the behavior of the whisker given the sensor input. However, the ELM is ranked the highest in speed and the second in terms of precision, only surpassed by the KNN-R algorithm. Recognizing the importance of a rapid and lightweight model is essential to maintain a satisfactory sensing frequency.

Table 1. Machine learning algorithms comparison.

Whisker Rotation	ELM (N_hidden_neurons = 30)			SVR (C = 8, Epsilon = 0.11)			MLP Single Layer (N_hidden_neurons = 100)			KNN-R (N_neighbors = 3)		
	MAE [rad]	RMSE [rad]	Time [ms]	MAE [rad]	RMSE [rad]	Time [ms]	MAE [rad]	RMSE [rad]	Time [ms]	MAE [rad]	RMSE [rad]	Time [ms]
θ_z	0.0221	0.0273	0.1	0.0453	0.0529	1.14	0.0286	0.0364	0.37	0.0155	0.0205	1.05
θ_y	0.0364	0.0465		0.0512	0.0609		0.0447	0.0609		0.0230	0.0315	

4. Results and Discussion

Six whiskers were randomly selected and evaluated in terms of the accuracy and computational cost for both models. The analytical model was fine-tuned with respect to scaling and bias factors through an optimization procedure using the nonlinear least squares method, while the data trained a specific ELM neural network algorithm. For each whisker, a test set of 200 points each was evaluated.

Although both models exhibited highly accurate performance across nearly all whiskers considered, the data-driven approach outperformed the analytical method in terms of efficiency. Analyzing Tables 2 and 3, we observe that the predictions of the ELM model are not only more precise but also faster than those of the analytical model. This efficiency gain can be explained based on the approximations of the analytical model, where there are no considerations for imperfection, misalignment, and tolerances in the sensor's mechanical design, which introduces challenging-to-model nonlinearities.

Table 2. Calibration for the analytical whisker rotational model.

Whisker	Model Parameters				θ_z			θ_y			Time [ms]
	sc_{θ_z}	b_{θ_z} [rad]	sc_{θ_y}	b_{θ_y} [rad]	MAE [rad]	RMSE [rad]	R^2	MAE [rad]	RMSE [rad]	R^2	
w_1	2.24	−0.0533	1.66	−0.0228	0.036	0.0489	0.945	0.0514	0.0723	0.8801	0.85
w_2	2.44	0.001	1.9	−0.04	0.0352	0.0469	0.9513	0.0577	0.0736	0.8681	0.72
w_3	2.27	−0.0321	1.56	0.01	0.0355	0.0477	0.949	0.052	0.0676	0.8973	0.64
w_4	2.65	0.054	2.12	0.05	0.0507	0.0702	0.8914	0.0818	0.1057	0.765	0.72
w_5	2.54	0.02	2	−0.01	0.0457	0.063	0.9157	0.0593	0.0829	0.8464	0.73
w_6	1.97	0.0476	1.5	−0.0834	0.036	0.0489	0.9468	0.0417	0.0557	0.931	0.73

Table 3. Calibration for the data driven whisker rotational model.

Whisker	θ_z			θ_y			Time [ms]
	MAE [rad]	RMSE [rad]	R^2	MAE [rad]	RMSE [rad]	R^2	
w_1	0.040	0.055	0.93	0.024	0.033	0.97	0.46
w_2	0.037	0.048	0.94	0.028	0.036	0.97	0.28
w_3	0.034	0.042	0.96	0.024	0.030	0.98	0.40
w_4	0.048	0.060	0.92	0.028	0.039	0.97	0.47
w_5	0.049	0.064	0.91	0.029	0.038	0.97	0.35
w_6	0.035	0.046	0.95	0.026	0.033	0.98	0.39

As shown in Figure 6, a comparison is drawn between a finely-tuned analytical model and a specific ELM applied to a single-whisker dataset. The figure highlights the precision of these models within the robot's captured workspace, presenting MAE and RMSE values for each cell. Upon observation, it becomes evident that the ELM performs well across the entire range of the whisker sensor, while the analytical model exhibits higher errors at higher rotational values. These findings affirm that the analytical model encounters challenges in predicting higher rotational angles, as nonlinearities are more likely to impact precision in this context.

In order to extend the model to cover the remaining whiskers, we opted to create a comprehensive general model for simplicity. This involved combining all the recorded whisker data into a single dataset. We then tuned and evaluated both analytical and data-driven models using these unified models. For the analytical model, we determined both bias and scaling factors by averaging the results presented in Table 2. Regarding the ELM model, we trained the new model using the combined whisker dataset. This time, we adopted a 70/30 split for training the ELM, where the total size of the dataset comprises 2094 recordings.

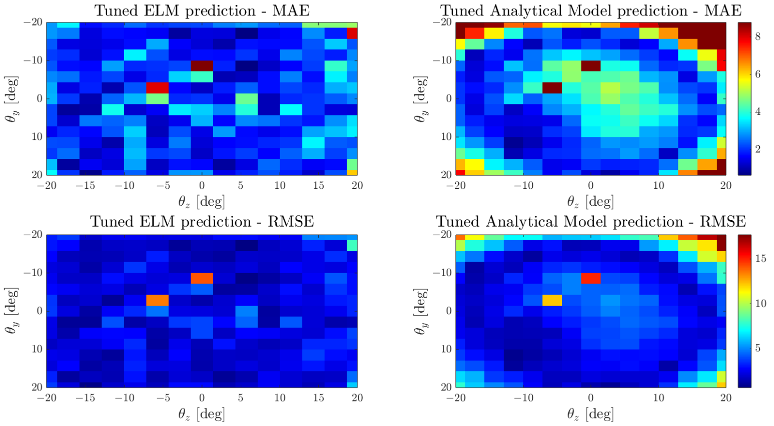

Figure 6. Mean average error and root mean square error comparison between the ELM and analytical models tuned for a single whisker.

To validate these models, we again compared the prediction and speed of both models in the test set to ensure that the ELM was not trained with them. Table 4 and Figure 7 present the comparison of both models for the representation of the whisker workspace. As expected, the ELM model results in a more suitable model, since it presents lower errors and deviation across the combined whiskers workspace.

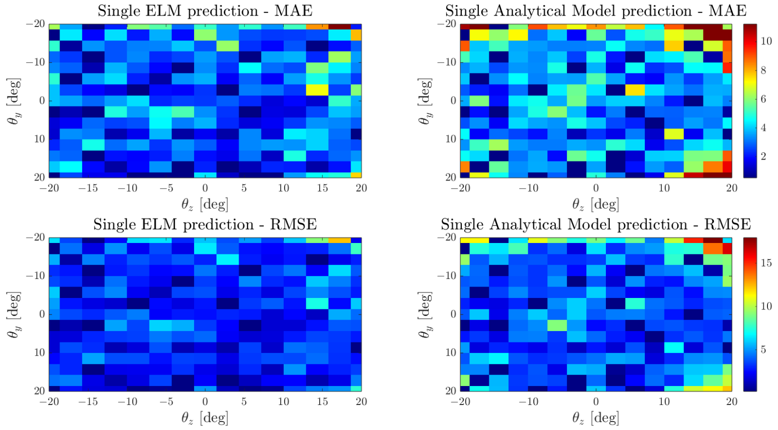

Figure 7. Mean average error and root mean square error comparison between the ELM and analytical models for the combined whisker dataset.

Consequently, the data-driven approach was chosen to ensure a faster sensor response given its superior precision and speed. The use of the same neural network trained with data from the collection of whiskers, along with appropriately scaled input values from other whiskers, was determined to yield relatively accurate results. However, to improve the accuracy and reliability of the model, each whisker sensor must undergo a specific tuning process to address imperfections that arise from the manufacturing process.

Table 4. Whisker rotation model comparison for general models for the combined whisker dataset.

Whisker Rotation Angles	**Single ELM (N_hidden_neurons = 30)**				**Single Analytical Model (sc_{θ_z} = 2.37, sc_{θ_y} = 1.75 b_{θ_z} = −0.01, b_{θ_y} = −0.02)**			
	MAE [rad]	**RMSE [rad]**	R^2	**Time [ms]**	**MAE [rad]**	**RMSE [rad]**	R^2	**Time [ms]**
θ_z	0.0352	0.0464	0.95	0.18	0.0505	0.0665	0.90	0.87
θ_y	0.0388	0.0537	0.94		0.0589	0.0833	0.84	

5. 3D-Mapping Implementation

After successfully validating the whisker model, we proceeded to implement it for a 3D-mapping scenario. In this occasion, the test platform, shown in Figure 8, incorporates the whisker disk as the end effector of the Universal Robots UR3e manipulator, while a rectangular box structure is securely attached to a technical table to mimic the basic geometry of a mine.

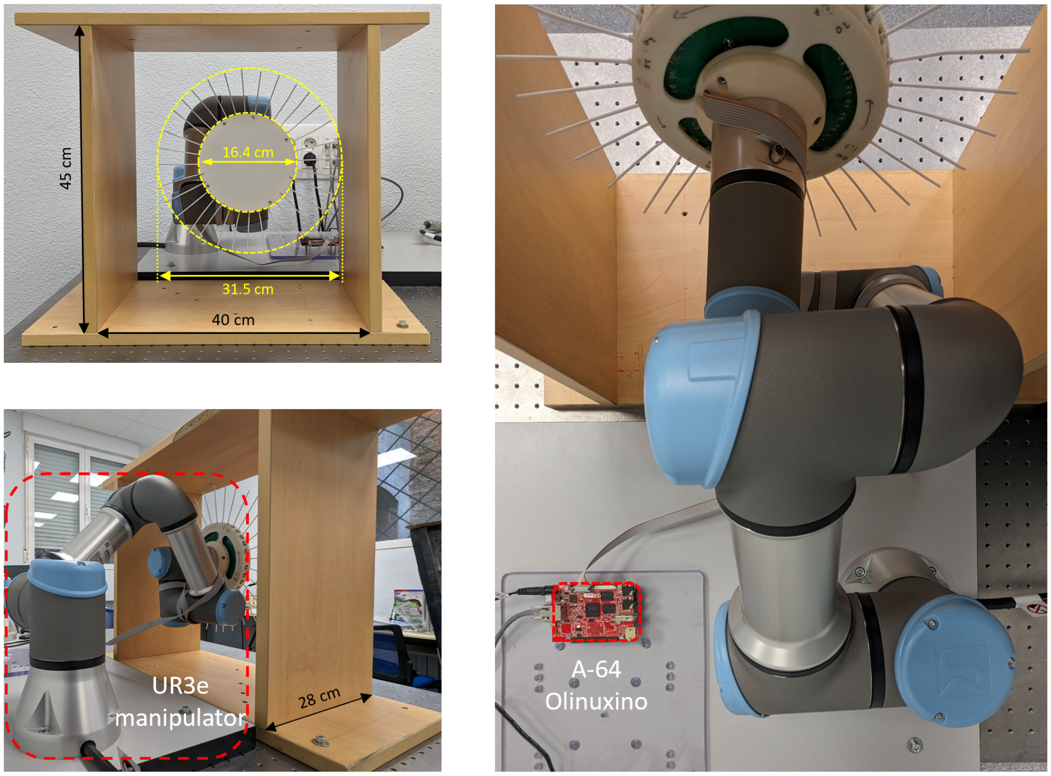

Figure 8. 3D mapping testbed for environment reconstruction. The wood structure represents a simple section of a mining environment. The surfaces to be mapped are the inner faces of the wooden box.

In order to visualize the point cloud produced by the whisker disk, we developed an application utilizing UR's ROS2 driver package [30] and Rviz for visualization purposes. The disk was attached to the UR3e arm to determine its position and orientation in space. The whiskers were represented using a rigid bar featuring two rotational joints at the pivot point of the whisker, with each rotation angle determined by the whisker rotational model.

For reading the 3D Hall-effect sensors, an Olimex A64 computer running an Ubuntu image was programed to execute a routine that verified the proper performance of each sensor and then published the readings in an ROS2 topic. A custom message was created to transmit all 32 magnetic field measurements in a single packet. The topic publishing rate was fixed at 10 Hz.

To generate the point cloud, a node was written to receive the custom whisker message and convert it into the spatial position of the whisker tip. Before publishing the point cloud, a condition to filter out non-deflected whiskers was implemented. The condition specified that the sum of the squares of the rotation angles of the whisker must exceed a threshold to be included in the point cloud. The threshold was empirically determined as 0.09, which yielded the best results.

3D-Mapping Experiment

The mapping experiment was carried out by teleoperating the robot arm to ensure that the whiskers were in contact with the surface being mapped. Figure 9 and Video S1 highlight the generation of the point cloud based on deflected whiskers. This approach demonstrated good performance in determining the shape and approximate geometry of the environment.

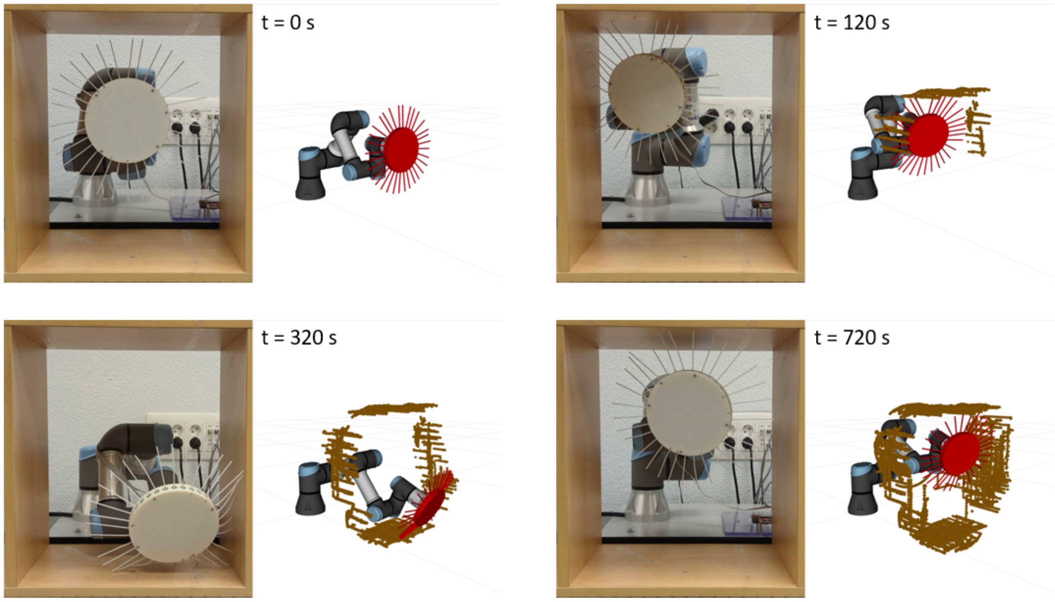

Figure 9. Environment reconstruction from the 3D-mapping experiment.

The generated point cloud is shown in Figure 10. It reveals an accurate representation of the box geometry, even though it presents minor errors observed in the central section of the box. These errors may arise from deflections in the whiskers, causing them to bend to such a degree that they do not fully return to their nominal shape and are captured by the point cloud.

To quantify the accuracy of the 3D geometry prediction, we performed additional mapping experiments and exported and processed the resulting point cloud by applying a clustering algorithm and implementing a filter based on the Mahalanobis distance to eliminate outliers. The results of the refined point cloud are presented in Figure 11 and

Table 5, which confirms the reliability of the proposed method with average errors close to millimeter precision on almost all surfaces. To obtain the distance difference from each surface, we projected the captured points onto the closest neighboring surface of the box and measured the Euclidean distance for each pair of points. Our analysis revealed that the predicted dimensions of the box measure 42.74 cm × 46.42 cm × 29.11 cm, showing a good approximation from the actual dimensions of the box (40 cm × 45 cm × 28 cm).

Table 5. Maximum and average errors derived from the post-processed point cloud and the projected points onto the adjacent box surface.

Box Inner Surface	Max Error [m]	Mean Error [m]
Left	0.0339	0.0149
Right	0.0394	0.0132
Top	0.022	0.0052
Bottom	0.0593	0.0123

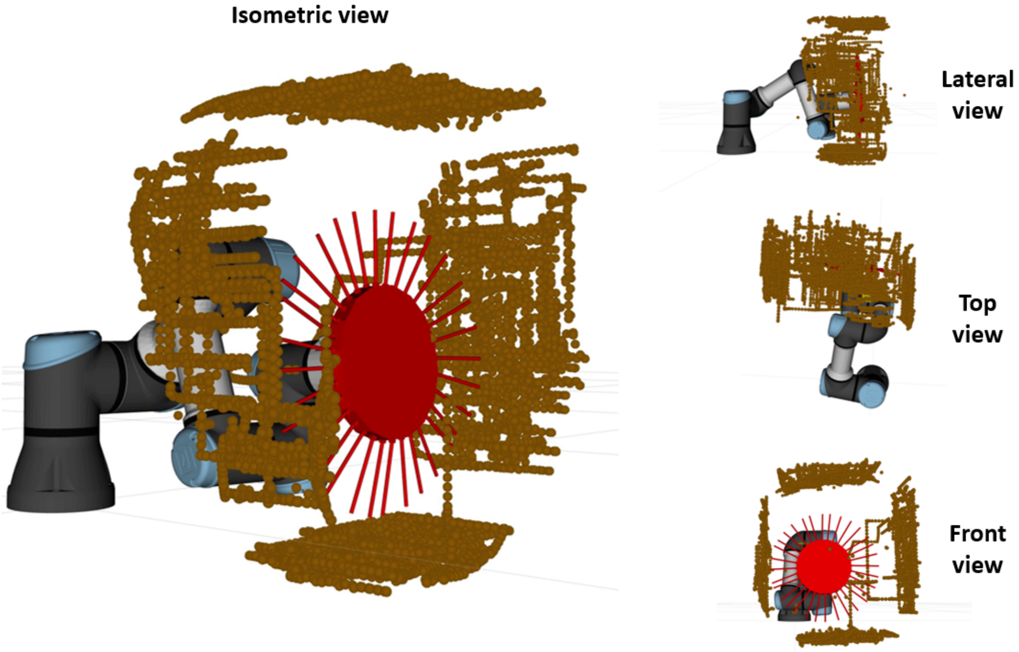

Figure 10. Orthographic views of the generated 3D pointcloud resulting from the mapping experiment.

Finally, it should be noted that the presented solution has been designed to work as a robotic module that can be adapted to the scaled-down version of the robominer platform [21], to give the robot the ability to map unstructured environments while operating. However, this concept can be easily adapted to larger mine-ready platforms.

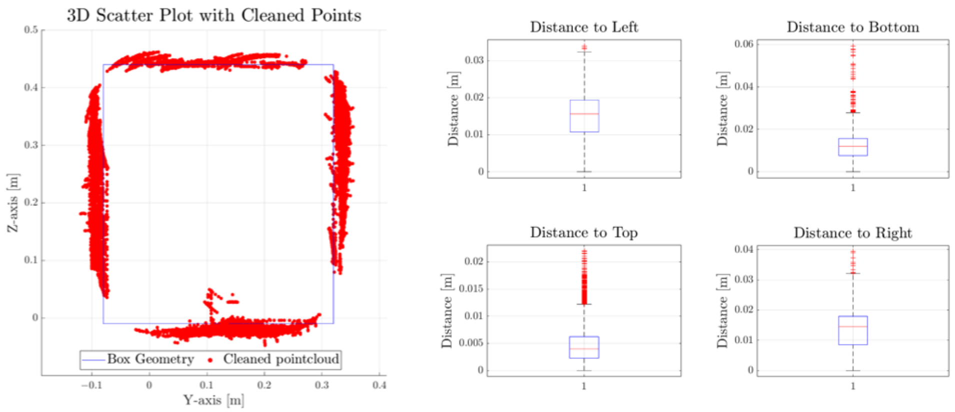

Figure 11. Three-dimensional point cloud comparison and error estimation between the ground truth and the prediction of each surface.

6. Conclusions

This study presented the design, modeling, and implementation of a sensor disk composed of a circular array of 32 whisker sensors for 3D mapping in unstructured environments. The design of the whisker comprises a plastic piece called a magnet holder, where a polystyrene rod and N52 permanent magnet are attached, and a 3D Hall-effect sensor that measures the magnetic flux generated by the magnet. The magnet holder features a spherical contact that acts as a ball joint. Each magnet holder is housed inside a silicone structure, and the magnetic sensors are installed on a single PCB.

The whisker was modeled following both analytical and data-driven approaches. For the analytical model, a series of relationships between the rotation angles and the magnetic flux measurements were derived based on the sensor manufacturer recommendations. To account for misalignment and variability from whisker to whisker, scaling and bias factors were included into the model and tuned based on experimental data, following a nonlinear least squares method. For the data collection process, a testbed featuring a UR3e robot was built to record the rotations of the whisker and the sensor measurements of the magnetic sensor.

For the data-driven approach, first a model selection process determined which algorithm resulted in the best performance considering both the precision and prediction time. Four widely used algorithms were considered, and we finally selected the ELM, as it presented the best balance between speed and accuracy.

To evaluate the performance of the models on the different sensors, six different whiskers were evaluated for both models. When comparing the results of the models, it was determined that the data-driven approach resulted in a more robust and faster performance than the analytical model, since it can account for nonlinearities that are not present in the analytical model. To account for the remaining sensors, a general model was developed and tested for both approaches, where the data captured from the recorded whiskers were merged into a single dataset. After tuning and evaluating the model, it was determined that the data-driven approach resulted in a more precise and robust solution. In addition, it was observed that the analytical model had difficulties estimating the rotational angles for large deflections of the whisker sensor, due to the appearance of difficult-to-model nonlinearities that are not considered. It is worth noting that to achieve optimal performance, each whisker must undergo an individual tuning process.

Once the whisker model was validated, the sensor disk was mounted in a serial manipulator to perform 3D-mapping experiments. A second testbed included a UR3e manipulator and a rectangular wood box that resembles a simple section of a mine geometry. The robot arm was teleoperated to map the inner surface of the rectangular box, resulting in a successful mapping of the geometry, thus validating the sensor capacity to reconstruct 3D environments. Although the sensing device was tested on a robot manipulator, the simple and easily adaptable design can be mounted on different robotic platforms, including mobile robots.

Recommendations for future developments include improvements to the mechanical design of the whisker to ensure its return to its nominal shape after bending as well as the design of new shapes of the whisker sensor to mimic the mole rat snout to improve the mapping performance in tight corners. Further advancements should also focus on refining the model to accurately identify contact points along the whisker, particularly in scenarios involving complex surface interactions, thus enhancing the overall accuracy and applicability of the system. Other studies can be carried out to generate a smart autonomous mapping algorithm that optimizes the mapping procedure.

Supplementary Materials: The following supporting information can be downloaded at: https://zenodo.org/records/10447310 (accessed on 31 December 2023), Video S1: whisker_demo.mp4.

Author Contributions: Conceptualization, V.G. and M.H.; Formal analysis, W.R. and M.H.; Funding acquisition, C.R.; Investigation, V.G. and M.H.; Methodology, V.G., W.R., and A.R.; Project administration, C.R.; Software, V.G. and W.R.; Supervision, M.H., A.R., and C.R.; Visualization, W.R.; Writing—original draft, V.G.; Writing—review and editing, W.R., M.H., A.R., and C.R.; All authors have read and agreed to the published version of the manuscript.

Funding: This research was funded by the European Commission's Horizon 2020 research and innovation program (ROBOMINERS, grant no. 820971).

Data Availability Statement: The data captured for the whisker sensors are available in the following repo: https://github.com/virgilio96upm/whisker-modeling/tree/main (accessed on 31 December 2023).

Acknowledgments: We would like to thank Oscar Rudek, Roza Gkliva, and Jaan Rebane for their collaboration in the project.

Conflicts of Interest: The authors declare no conflicts of interest. Funding institutions had no role in the design of the study; in the collection, analyses, or interpretation of data; in the writing of the manuscript; or in the decision to publish the results.

References

1. Lopes, L.; Bodo, B.; Rossi, C.; Henley, S.; Žibret, G.; Kot-Niewiadomska, A.; Correia, V. ROBOMINERS—Developing a bio-inspired modular robot-miner for difficult to access mineral deposits. *Adv. Geosci.* **2020**, *54*, 99–108. [CrossRef]
2. Pearson, M.J.; Mitchinson, B.; Sullivan, J.C.; Pipe, A.G.; Prescott, T.J. Biomimetic vibrissal sensing for robots. *Philos. Trans. R. Soc. B Biol. Sci.* **2011**, *366*, 3085–3096. [CrossRef]
3. Solomon, J.H.; Hartmann, M.J.Z. Extracting Object Contours with the Sweep of a Robotic Whisker Using Torque Information. *Int. J. Robot. Res.* **2010**, *29*, 1233–1245. [CrossRef]
4. Zhao, C.; Zhang, S.; Xie, T.; Zeng, L. A novel whisker sensor with variable detection range for object positioning. *Rev. Sci. Instruments* **2022**, *93*, 035007. [CrossRef] [PubMed]
5. Lin, M.A.; Reyes, E.; Bohg, J.; Cutkosky, M.R. Whisker-Inspired Tactile Sensing for Contact Localization on Robot Manipulators. In Proceedings of the 2022 IEEE/RSJ International Conference on Intelligent Robots and Systems (IROS), Kyoto, Japan, 23–27 October 2022; pp. 7817–7824. [CrossRef]
6. Pearson, M.J.; Salman, M. Active Whisker Placement and Exploration For Rapid Object Recognition. In Proceedings of the 2019 IEEE/RSJ International Conference on Intelligent Robots and Systems (IROS), Macau, China, 3–8 November 2019; pp. 672–677. [CrossRef]
7. Zeng, L.; Zhang, S.; Xie, T.; Zhao, C. Contour recognition method of Hall-effect-based whisker sensor. *Meas. Sci. Technol.* **2022**, *33*, 065104. [CrossRef]
8. Jiang, Q.; Wei, G.; Zhao, C. Fiber Bragg grating-based biomimetic whisker for shape and texture recognition. *J. Instrum.* **2018**, *13*, P11013. [CrossRef]
9. Miersch, L.; Hanke, W.; Wieskotten, S.; Hanke, F.D.; Oeffner, J.; Leder, A.; Brede, M.; Witte, M.; Dehnhardt, G. Flow Sensing by Pinniped Whiskers. *Philos. Trans. R. Soc. Lond. B Biol. Sci.* **2011**, *366*, 3077–3084. [CrossRef] [PubMed]
10. Ju, F.; Ling, S.F. Sensing fluid viscosity and density through mechanical impedance measurement using a whisker transducer. *Meas. Sci. Technol.* **2013**, *24*, 055105. [CrossRef]
11. Zheng, X.; Kamat, A.M.; Harish, V.S.; Cao, M.; Kottapalli, A.G.P. Optimizing Harbor Seal Whisker Morphology for Developing 3D-Printed Flow Sensor. In Proceedings of the 2021 21st International Conference on Solid-State Sensors, Actuators and Microsystems (Transducers), Orlando, FL, USA, 20–24 June 2021; pp. 1271–1274. [CrossRef]

12. Fox, C.; Evans, M.; Pearson, M.; Prescott, T. Tactile SLAM with a biomimetic whiskered robot. In Proceedings of the 2012 IEEE International Conference on Robotics and Automation, Saint Paul, MN, USA, 14–18 May 2012; pp. 4925–4930. [CrossRef]
13. Xu, P.; Wang, X.; Wang, S.; Chen, T.; Liu, J.; Zheng, J.; Li, W.; Xu, M.; Tao, J.; Xie, G. A Triboelectric-Based Artificial Whisker for Reactive Obstacle Avoidance and Local Mapping. *Research* **2021**, *2021*, 9864967. [CrossRef]
14. Jung, D.; Zelinsky, A. Whisker based mobile robot navigation. In Proceedings of the IEEE/RSJ International Conference on Intelligent Robots and Systems. IROS'96, Osaka, Japan, 8 November 1996; Volume 2, pp. 497–504. [CrossRef]
15. Brown, L.; Carrasco, J.; Watson, S.; Lennox, B. Elbow Detection in Pipes for Autonomous Navigation of Inspection Robots. *J. Intell. Robot. Syst.* **2019**, *95*, 527–541. [CrossRef]
16. Wei, Z.; Shi, Q.; Li, C.; Yan, S.; Jia, G.; Zeng, Z.; Huang, Q.; Fukuda, T. Development of an MEMS based biomimetic whisker sensor for tactile sensing. In Proceedings of the 2019 IEEE International Conference on Cyborg and Bionic Systems (CBS), Munich, Germany, 18–20 September 2019; pp. 222–227. [CrossRef]
17. Milford, M.; Wyeth, G.; Prasser, D. RatSLAM: A hippocampal model for simultaneous localization and mapping. In Proceedings of the IEEE International Conference on Robotics and Automation, 2004. Proceedings. ICRA'04. 2004, New Orleans, LA, USA, 26 April–1 May 2004; Volume 1, pp. 403–408. [CrossRef]
18. Salman, M.; Pearson, M.J. Advancing whisker based navigation through the implementation of Bio-Inspired whisking strategies. In Proceedings of the 2016 IEEE International Conference on Robotics and Biomimetics (ROBIO), Qingdao, China, 3–7 December 2016; pp. 767–773. [CrossRef]
19. Burlet, C.; Stasi, G.; Godon, S.; Gkliva, R.; Piho, L.; Ristolainen, A. ROBOMINERS resilient reflectance/fluorescence spectrometers. In Proceedings of the EGU General Assembly 2023, Vienna, Austria, 24–28 April 2023. [CrossRef]
20. Boublil, B.L.; Diebold, C.A.; Moss, C.F. Mechanosensory Hairs and Hair-like Structures in the Animal Kingdom: Specializations and Shared Functions Serve to Inspire Technology Applications. *Sensors* **2021**, *21*, 6375. [CrossRef]
21. Gomez, V.; Hernando, M.; Aguado, E.; Sanz, R.; Rossi, C. ROBOMINER: Development of a Highly Configurable and Modular Scaled-Down Prototype of a Mining Robot. *Machines* **2023**, *11*, 809. [CrossRef]
22. Park, T.; Lewin, G.; Buffenstein, R. Naked Mole Rats: Their Extraordinary Sensory World. In *Encyclopedia of Animal Behavior*; Breed, M.D., Moore, J., Eds.; Academic Press: Oxford, UK, 2010; pp. 505–512. [CrossRef]
23. Crish, S.D.; Rice, F.L.; Park, T.J.; Comer, C.M. Somatosensory organization and behavior in naked mole-rats I: Vibrissa-like body hairs comprise a sensory array that mediates orientation to tactile stimuli. *Brain. Behav. Evol.* **2003**, *62*, 141–151. [CrossRef] [PubMed]
24. Universal Robots. RTDE Client Library-Python. Available online: https://github.com/UniversalRobots/RTDE_Python_Client_Library (accessed on 31 December 2023).
25. Infineon Technologies. TLV493D-A1B6. Available online: https://www.infineon.com/cms/en/product/sensor/magnetic-sensors/magnetic-position-sensors/3d-magnetics/tlv493d-a1b6/ (accessed on 25 November 2023).
26. Huang, G.B.; Zhu, Q.Y.; Siew, C.K. Extreme learning machine: A new learning scheme of feedforward neural networks. In Proceedings of the 2004 IEEE International Joint Conference on Neural Networks (IEEE Cat. No.04CH37541), Budapest, Hungary, 25–29 July 2004; Volume 2, pp. 985–990. [CrossRef]
27. Murtagh, F. Multilayer perceptrons for classification and regression. *Neurocomputing* **1991**, *2*, 183–197. [CrossRef]
28. Zhang, F.; O'Donnell, L.J. Chapter 7—Support vector regression. In *Machine Learning*; Mechelli, A., Vieira, S., Eds.; Academic Press: Cambridge, MA, USA, 2020; pp. 123–140. [CrossRef]
29. Kramer, O., K-Nearest Neighbors. In *Dimensionality Reduction with Unsupervised Nearest Neighbors*; Springer: Berlin/Heidelberg, Germany, 2013; pp. 13–23. [CrossRef]
30. Universal Robots. Universal Robots ROS2 Driver. Available online: https://github.com/UniversalRobots/Universal_Robots_ROS2_Driver (accessed on 31 December 2023).

Appendices

Appendix A

Scientific Dissemination

A.1 Journal Publications

Gomez, V., Hernando, M., Aguado, E., Sanz, R., & Rossi, C. (2023). *ROBOMINER: Development of a Highly Configurable and Modular Scaled-Down Prototype of a Mining Robot.* Machines, 11(8), 809. doi.org/10.3390/machines11080809

Gomez, V., Hernando, M., Aguado, E., Bajo, D., & Rossi, C. (2023). *Design and Kinematic Modeling of a Soft Continuum Telescopic Arm for the Self-Assembly Mechanism of a Modular Robot.* Soft Robotics. doi.org/10.1089/soro.2023.0020

Gomez, V., Remmas, W., Hernando, M., Ristolainen, A., & Rossi C.(2024) *Bioinspired Whisker Sensor for 3D Mapping of Underground Mining Environments.* Biomimetics., 9(2):83. doi.org/10.3390/biomimetics9020083

Aguado, E., **Gomez, V.**, Hernando, M., Rossi, C. & Sanz, R. (2024). *A Survey of Ontology-Enabled Processes for Dependable Robot Autonomy.* Frontiers in Robotics and AI. 11:1377897. doi.org/10.3389/frobt.2024.1377897

A.2 Conferences

Gomez, V., Bajo, D., Aguado, E., Hernando, M.,Sanz, R., & Rossi, C. (2022) *Desarrollo de robots modulares altamente configurares con capacidades de auto-ensamblado* In Jornadas de Robótica, Educación y Bioingeniería 2022: Libro de actas. Retrieved from: https://oa.upm.es/82672/

Gomez, V., Hernando, M., Aguado, E., Bajo, D., Sanz, R., & Rossi, C. (2023) *Robominer: Robot modular resiliente para operaciones mineras* In Jornadas Nacionales de Robótica y Bioingeniería 2023: Libro de actas. Fundación General de la Universidad Politécnica de Madrid. 10.20868/UPM.book.74896

Gomez, V., & Hernando, M. (2022). *Modular collaborative resilient robots for mining operations*. In EGU General Assembly 2022, Vienna, Austria, 23–27 May 2022. https://doi.org/10.5194/egusphere-egu22-2740

Aguado, E., **Gomez, V**., Hernando, M., Rossi, C. & Sanz, R. (2024). Category Theory for Autonomous Robots: The Marathon 2 Use Case. In: Marques, L., Santos, C., Lima, J.L., Tardioli, D., Ferre, M. (eds) Robot 2023: Sixth Iberian Robotics Conference. ROBOT 2023. Lecture Notes in Networks and Systems, vol 976. Springer, Cham. https://doi.org/10.1007/978-3-031-58676-7_4

Aguado, E., **Gomez, V.**, Hernando, M., Rossi, C., & Sanz, R. (2023, June). *Category Theory for Autonomous Robots: The Sys-Self Model*. In Compositional Robotics: Mathematics and Tools (ICRA 2023 Workshop), London, UK. Retrieved from https://ethz.ch/content/dam/ethz/special-interest/mavt/dynamic-systems-n-control/idsc-dam/Research_Frazzoli/workshops/ICRA2023CRMT_paper_3.pdf

A.3 Patents

Hernando, M., Bajo, D., **Gomez, V.**, Aguado, E., & Rossi, C.(2022). Sistema mecánico de actuación para un brazo robótico flexible. Patent Nº ES2907801. Retrieved from: https://www.oepm.es/pdf/ES/0000/000/02/90/78/ES-2907801_A1.pdf

Appendix B

Unpublished results

Following the development of the coupling mechanism for the RM2 module and the whisker sensor disk, further progress has been made, including the implementation of a vision system module to perform self-assembly maneuvers (**P.II**) as well as an active sensing mechanism combining the soft continuum arm (**P.II**) with the whisker sensor disk (**P.III**). These developments are additional results that demonstrate the possibility of performing fully autonomous coupling maneuvers, as well as exploring another application of the coupling arm, while confirming the modularity of the proposed sensing disk.

B.1 Vision system for self-assembly mechanism

To autonomously identify the position of a robotic module's passive interface relative to another module's active interface, a vision system was developed. This vision system features an ESP32CAM, a compact package that includes an ESP32 microcontroller with Wi-Fi and Bluetooth connectivity, an integrated camera, and a microSD card slot. The camera can function independently, without the need for the module's main control board to perform any tasks. Given the PCB's size constraints, the decision was made to develop the vision system as an auxiliary module that can be attached to the mobile module's leg mechanism.

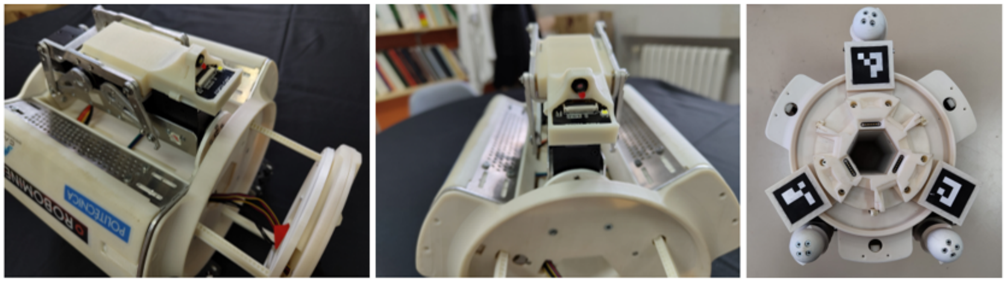

Figure B.1: Vision sytem for self-assembly mechanism. The camera module is installed in the leg of a mobile module, while the passive interface integrates a set of three equally distant ArUco codes.

The passive interface includes three distinct ArUco codes to help determine the pose of the code from various angles and orientations. Given that the positions of these codes in relation to the center is known, the location of the center of the 'passive' module relative to the center of the 'active' module can be computed. The final version of the vision system is shown in Figure B.1.

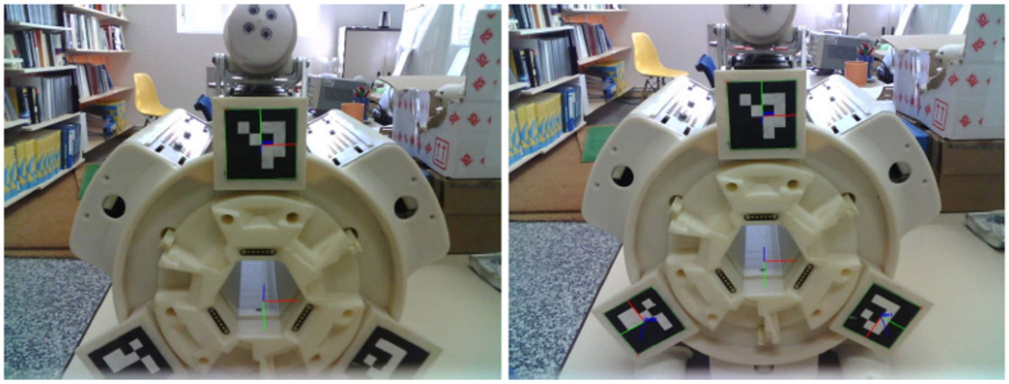

Figure B.2: Graphical representation of the passive port frame calculation as a function of the ArUco codes detected. A single code is enough to determine the position of the passive port pose.

To determine the pose of the passive port with respect to the camera module, the main board microcontroller sends a message through I2C to trigger the camera module. Next, the module captures an image of the passive port and sends it by WiFi using a TCP protocol to the main control, in this case a PC. The computer then runs a single script using OpenCV and ArUco libraries to determine the pose of the passive port with respect to the camera frame as shown in Figure B.2. Finally, using the mobile module kinematic model, the camera frame is transformed to the coupling mechanism frame to provide the desired point that the mechanism needs to reach. At this point, the inverse kinematic model of the arm calculates the rack extension for each section to drive the arm to the position. It is important to note that the model had to be re-trained with a new set of data that considered weight and gravity effects of the end effector.

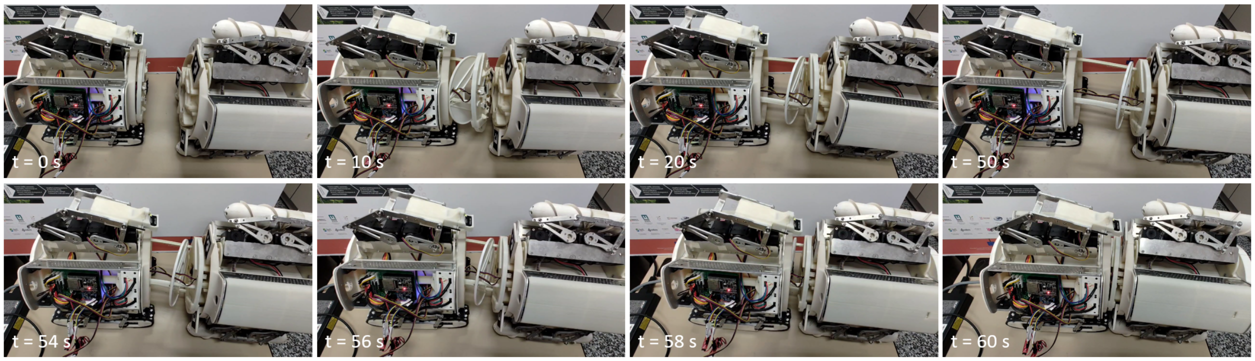

Figure B.3: Self-assembly coupling maneuver between two mobile modules.

Once the new model was validated, a sequence of coupling operations was conducted to assess the vision system and the arm model's performance. To carry out the self-assembly operation, a coupling message is initially sent from the central control station to the mobile module. Following this, the ESP32CAM module begins to capture and transmit images to the control station. The control station then processes the images to determine the current position of the passive interface relative to the coupling head and computes the required rack extension to reach the target point. This cycle continues until the coupling interface is close enough to the threshold of the coupling interface, triggering the initiation of the docking maneuver. Once the claws and T-profiles secure the connection with the module, it is retracted to the first module to finalize the coupling operation. An example of the coupling maneuver is presented in Figure B.3.

B.2 Active sensing mechanism

The active sensing mechanism allows the RM2 robotic system (**P.I**) to perform mapping tasks, integrating the soft continuum arm (**P.II**) with the whisker disk sensing module (**P.III**), seamlessly linked to the robot through an integrated coupling interface within the arm. In this case, the soft telescopic continuum arm is utilized as a 5 DoF (X, Y, Z, Pitch, & Roll) manipulator to guide the disk to the desired position.

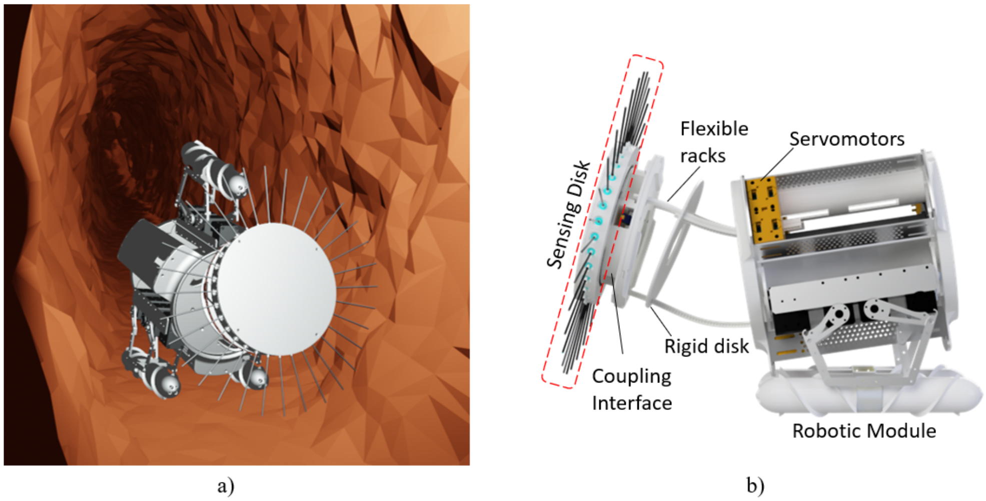

a)

b)

Figure B.4: Active Sensing Mechanism description. (a) The active sensing mechanism can improve the navigation capabilities of the modular platforms in underground mine environments. (b) The mechanism comprises a soft robotic arm embedded into the structure of a robotic module with an integrated sensing disk as the end effector

B.2.1 Mechanism modeling

To model the active mechanism, a data-driven approach was chosen. This contrasts with the model-based method used in **P.II**, which assumes a constant curvature in the arm's virtual backbone. This model is generally accurate when the effects of weight and gravity on the arm's behavior are minimal. However, when extra weight is added to the arm's tip, the bending effects on the racks become more significant, leading to different curvatures in various sections of the arm. To address these complex nonlinearities, a machine learning algorithm was employed to solve the direct kinematic problem, enabling the determination of the disk's position in 3D space. This section details the approach taken, explaining the data collection and modeling process used to solve the kinematic problem for the active sensing prototype.

B.2.1.1 Data capture procedure

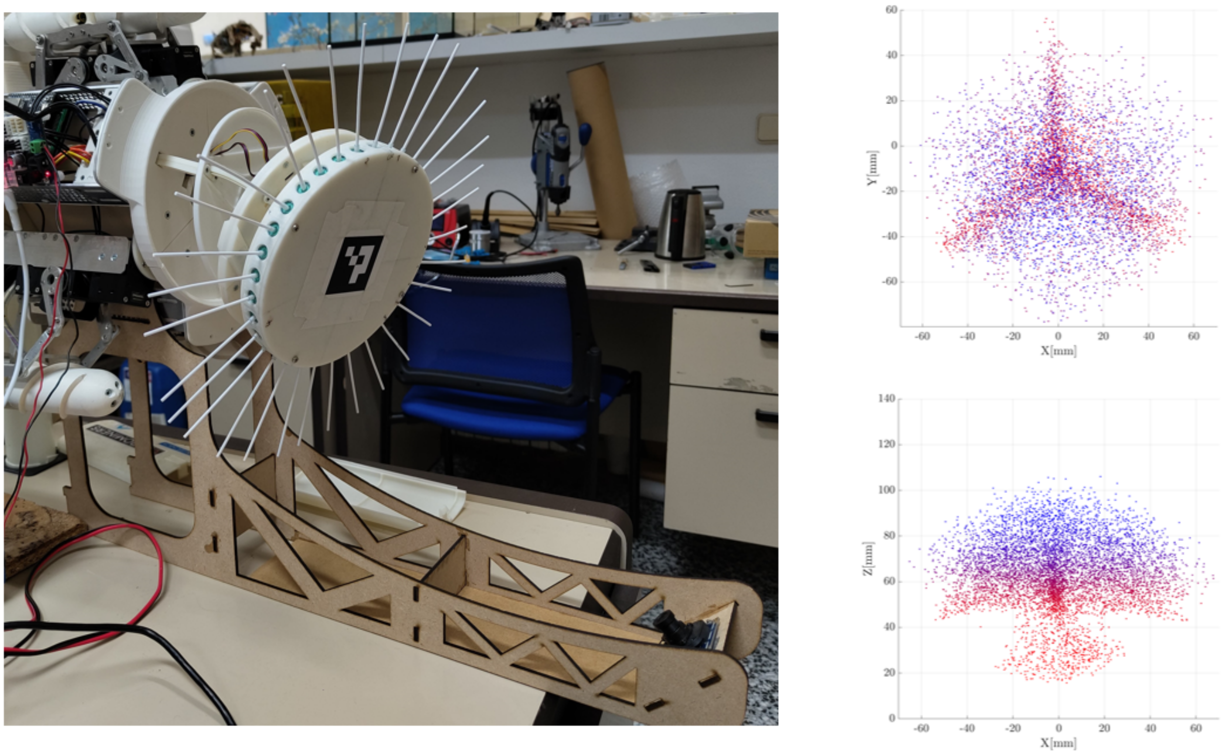

Figure B.5: (**Left**) Data collection testbed affixed to the robotic module to capture the position and orientation of the tip of the Active Sensing Mechanism. (**Right**) Active sensing mechanism workspace derived from the data capture procedure. The top view is the XY plane, while the bottom shows the XZ plane. Each point represents the midpoint of the whisker disk.

For the data collection process, a similar process was followed to the one described in Publication **P.II**, where an RGB camera was mounted on an external structure affixed to the robot side (Figure B.5 Left). However, in this occasion, the pose of the disk is captured considering the effect of gravity. This arrangement facilitated the camera's positioning towards the area accessible by the soft arm's end effector, enabling the capture of its position and orientation using ArUco codes. Orientation was represented using quaternions in radians, while position was captured as a 3D vector in meters. In addition, the rack extensions were recorded in millimeters based on input from motor encoders. The resulting workspace, derived from the collected data (6660 points), is shown in Figure B.5 right.

B.2.1.2 Arm modeling

After gathering and pre-processing all the data, a thorough model selection process was undertaken, comparing various machine learning algorithms. Drawing from prior experience, the selection encompassed a Multilayer Perceptron (MLP), an Extreme Learning Machine (ELM), and a K-Nearest Neighbors Regressor (K-NNR) algorithm. To ensure the identification of the best-performing model, each algorithm was fine-tuned to achieve optimal accuracy and speed. The evaluation metrics used were the root mean square error (RMSE), mean absolute error (MAE), and average prediction time (Δt). Examining the outcomes from comparison Table B.1, it is evident that the MLP model surpasses the other methods in accuracy. Despite not being the quickest in terms of speed, the MLP model lags only 13.7% behind the fastest model (ELM). Thus, the MLP was chosen as the final model for the mechanism..

Table B.1: Comparison of machine learning algorithms. Each algorithm was evaluated using the same test set.

	Single layer MLP (150 neurons)			ELM (250 neurons)			K-NNR (8 neighbors)		
	RMSE	MAE	time [ms]	RMSE	MAE	time [ms]	RMSE	MAE	time [ms]
angle[deg]	0.94	0.89	11.6	2.04	4.12	10.2	4.42	19.52	97.4
X [mm]	1.21	0.95		2.33	1.80		5.04	3.85	
Y [mm]	1.65	1.03		2.56	1.84		5.15	3.82	
Z [mm]	1.45	0.97		2.95	2.11		2.72	2.07	

B.2.1.3 Validation

Following the selection of the machine learning algorithm, a validation test was conducted. This test consisted of comparing a series of movements with the predictions made by the algorithm. The assessed maneuver involved vertical movements, with the positional data for this specific series being compared to the neural network's output as illustrated in Figure B.6. The corresponding data is also presented in Table B.2, where the machine learning algorithm demonstrates precise predictions of the arm tip's position and orientation, showing a maximum average deviation of 3.5 mm in all dimensions and an average angular deviation of 6 degrees.

Table B.2: Results for the validation of the NN

	Angle [deg]	X[mm]	Y[mm]	Z[mm]
RMSE	2.50	2.80	3.50	1.20
MAE	6.24	2.30	3.30	1.00

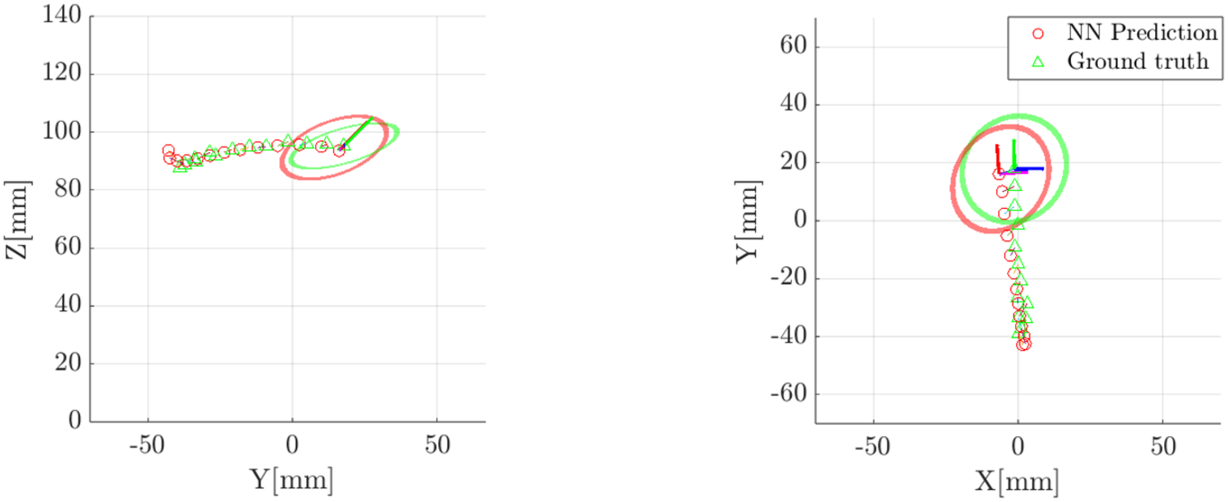

Figure B.6: Validation test for the Forward Kinematics comparing the position of the center of the disk (green triangle) against the data predicted by the NN (red circles).

B.2.2 3D Mapping experiments

To test the mapping capabilities of the mechanism a simple geometric feature, a 45 degree corner of a hollow box, was selected. The testbed is presented in Fig. B.7, where the robot is fixed on a stand and the active-sensing mechanism is controlled through a pre-programmed sequence. To visualize the resulting pointcloud, first the position of the whisker disk is published by writing a ros node that reads the arm servomotors and converts the rack extensions into positions using the developed neural network. In parallel, the whisker data are published in a topic using an olimex computer. Lastly, a ROS package subscribes to both topics, maps the input of the whiskers to the resulting bending angle of each whisker following the approach in Section 4.3, where the pointcloud is captured when the whisker experiences a bending angle larger than an empirically determined threshold value. This measure is used to filter noisy data, with the drawback of affecting the responsiveness of the whisker.

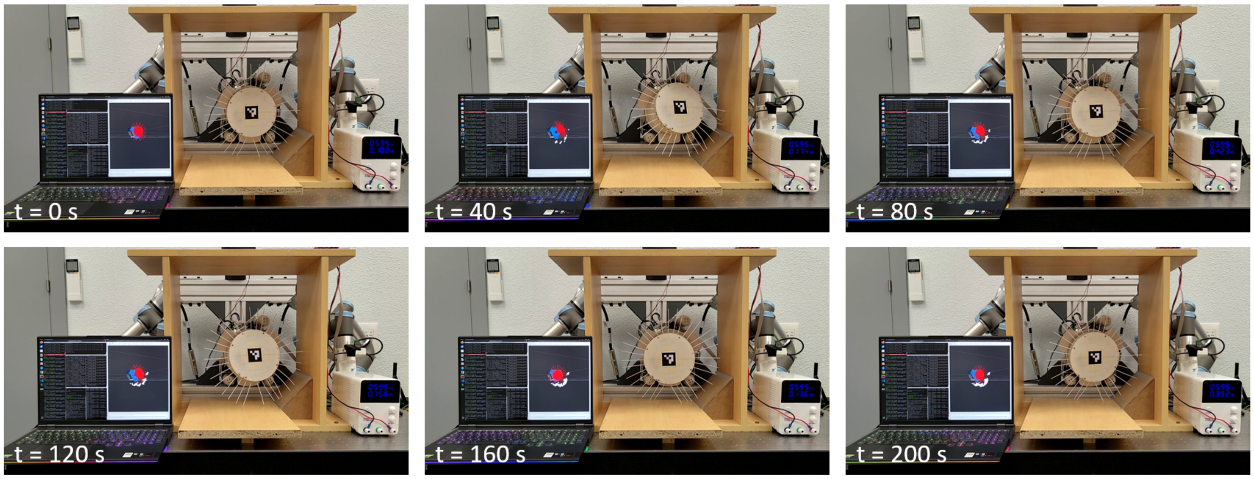

Figure B.7: 3D mapping testbed setup and mapping experiment. The active sensing mechanism is guided towards the lower right corner of the box to perform environment reconstruction tasks.

Figures B.8, B.9 and Table B.3 show the results of the filtered point cloud, validating the accuracy of the proposed method with average errors around one centimeter level on most surfaces. To calculate the distance discrepancies for each surface, points were projected onto the nearest surface of the box, and the Euclidean distances between point pairs were computed. Compared to the results presented in 4.5, it can be seen that the performance is similar, validating the functionality of the soft robot arm as a manipulator to drive the sensing disk.

Table B.3: Maximum and average errors derived from the post-processed point cloud of the active mechanism and the projected points onto the adjacent box surface.

Box Inner Surface	Max Error [mm]	Mean Error [mm]
Right	3.59	1.34
Inclined	32.98	11.87
Bottom	47.22	19.26

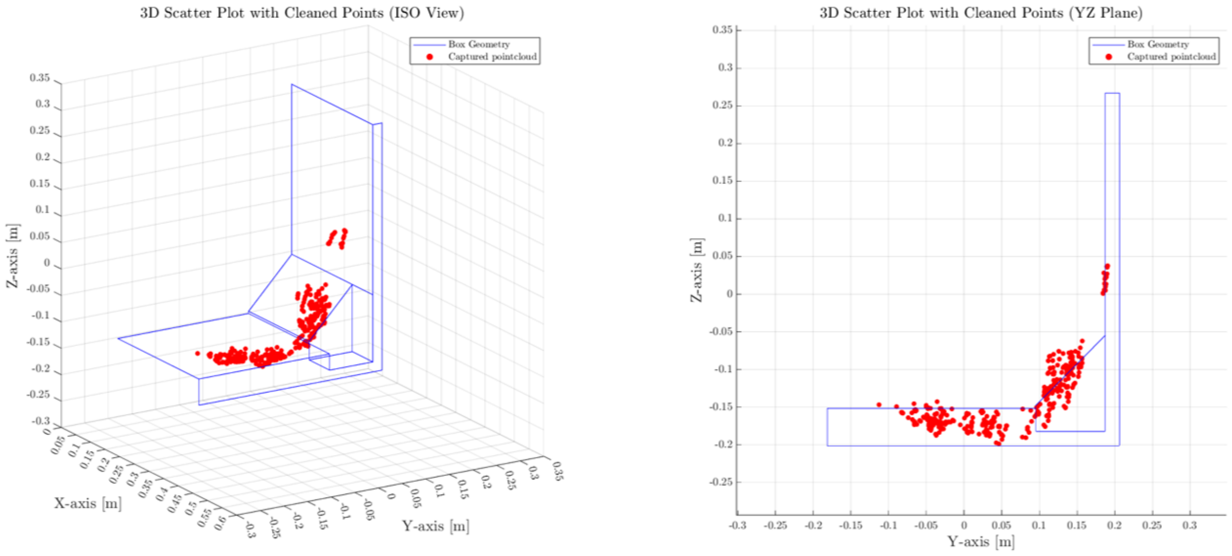

Figure B.8: Resulting pointcloud from mapped corner. The left view present an ISO view of the pointcloud, while the right subfigure presents a frontal view of the resultint pointcloud.

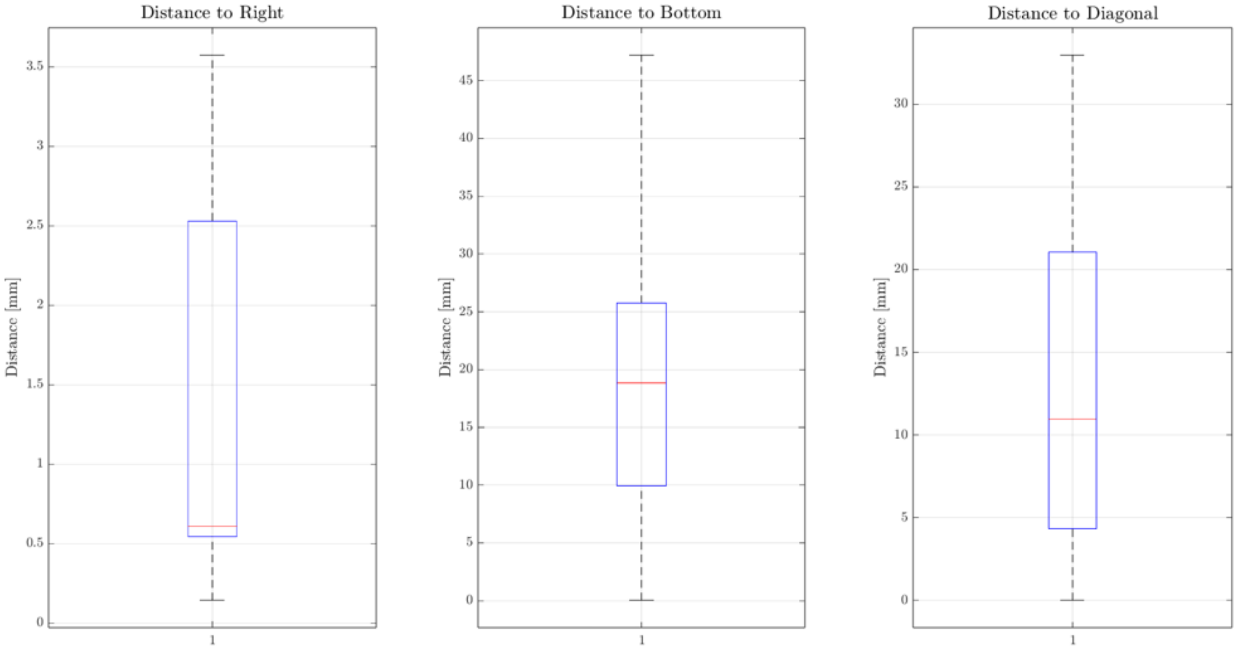

Figure B.9: Distance between bottom, inclined and horizontal planes and the clustered point located within this planes. The error metric is the projected distance from the point and the plane.

References

Agha, A., Otsu, K., Morrell, B., Fan, D. D., Thakker, R., Santamaria-Navarro, A., Kim, S.-K., Bouman, A., Lei, X., Edlund, J., Fadhil Ginting, M., Ebadi, K., Anderson, M., Pailevanian, T., Terry, E., Wolf, M., Tagliabue, A., Stegun Vaquero, T., Palieri, M., … Burdick, J. (2021). NeBula: Quest for Robotic Autonomy in Challenging Environments; TEAM CoSTAR at the DARPA Subterranean Challenge. *arXiv e-prints*, Article arXiv:2103.11470, arXiv:2103.11470. https://doi.org/10.48550/arXiv.2103.11470

Aguado, E., Milosevic, Z., Hernández, C., Sanz, R., Garzon, M., Bozhinoski, D., & Rossi, C. (2021). Functional self-awareness and metacontrol for underwater robot autonomy. *Sensors*, *21*(4). https://doi.org/10.3390/s21041210

Ahmadzadeh, H., Masehian, E., & Asadpour, M. (2015). Modular robotic systems: Characteristics and applications. *Journal of Intelligent & Robotic Systems*, *81*, 317–357.

Alexis, K. (2019). Resilient autonomous exploration and mapping of underground mines using aerial robots. *2019 19th International Conference on Advanced Robotics (ICAR)*, 1–8. https://doi.org/10.1109/ICAR46387.2019.8981545

Azpúrua, H., Rezende, A., Potje, G., da Cruz Júnior, G. P., Fernandes, R., Miranda, V., de Resende Filho, L. W., Domingues, J., Rocha, F., de Sousa, F. L. M., de Barros, L. G. D., Nascimento, E. R., Macharet, D. G., Pessin, G., & Freitas, G. M. (2021). Towards semi-autonomous robotic inspection and mapping in confined spaces with the espeleorobô. *Journal of Intelligent & Robotic Systems*, *101*(4), 69. https://doi.org/10.1007/s10846-021-01321-5

Baker, C., Omohundro, Z., Thayer, S., Whittaker, W., Montemerlo, M., & Thrun, S. (2006). A case study in robotic mapping of abandoned mines. In S. Yuta, H. Asama, E. Prassler, T. Tsubouchi, & S. Thrun (Eds.), *Field and service robotics: Recent advances in reserch and applications* (pp. 487–495). Springer Berlin Heidelberg. https://doi.org/10.1007/10991459_47

Biggie, H., Rush, E., Riley, D., Ahmad, S., Ohradzansky, M., Harlow, K., Miles, M., Torres, D., McGuire, S., Frew, E., Heckman, C., & Humbert, J. (2023). Flexible supervised autonomy for exploration in subterranean environments. *Field Robotics*, *3*(1), 125–189. https://doi.org/10.55417/fr.2023004

Bołoz, Ł., & Biały, W. (2020). Automation and robotization of underground mining in poland. *Applied Sciences*, *10*(20). https://doi.org/10.3390/app10207221

Brown, H., Vande Weghe, J., Bererton, C., & Khosla, P. (2002). Millibot trains for enhanced mobility. *IEEE/ASME Transactions on Mechatronics*, *7*(4), 452–461. https://doi.org/10.1109/TMECH.2002.806226

Brunete, A., Ranganath, A., Segovia, S., de Frutos, J. P., Hernando, M., & Gambao, E. (2017). Current trends in reconfigurable modular robots design. *International Journal of Advanced Robotic Systems*, *14*(3), 1729881417710457. https://doi.org/10.1177/1729881417710457

Bruzzone, L., & Quaglia, G. (2012). Review article: Locomotion systems for ground mobile robots in unstructured environments. *Mechanical Sciences*, *3*(2), 49–62. https://doi.org/10.5194/ms-3-49-2012

Callow, D. S. (2018). *Mine rescue robotics: Gemini scout.* (tech. rep.). Sandia National Lab.(SNL-NM), Albuquerque, NM (United States).

Cao, C., Nogueira, L., Zhu, H., Keller, J., Best, G., Garg, R., Kohanbash, D., Maier, J., Zhao, S., Yang, F., Cujic, K., Darnley, R., DeBortoli, R., Drozd, B., Sun, P., Higgins, I., Willits, S., Armstrong, G., Zhang, J., & Scherer, S. (2023). Exploring the most sectors at the darpa subterranean challenge finals. *Field Robotics*, *3*, 801–836. https://doi.org/10.55417/fr.2023025

Carreras, M., Candela, C., Ribas, D., Mallios, A., Magí, L., Vidal, E., Palomeras, N., & Ridao, P. (2013). Sparus ii, design of a lightweight hovering auv. *Martech 2013 5th International Workshop on Marine Technology*.

Carreras, M., Hernández, J. D., Vidal, E., Palomeras, N., Ribas, D., & Ridao, P. (2018). Sparus ii auv—a hovering vehicle for seabed inspection. *IEEE Journal of Oceanic Engineering*, *43*(2), 344–355. https://doi.org/10.1109/JOE.2018.2792278

Champeny-Bares, L., Coppersmith, S., & Dowling, K. (1991, May). *The terregator mobile robot* (tech. rep. No. CMU-RI-TR-93-03). Pittsburgh, PA.

Chung, T. H., Orekhov, V., & Maio, A. (2023). Into the robotic depths: Analysis and insights from the darpa subterranean challenge. *Annual Review of Control, Robotics, and Autonomous Systems*, *6*(Volume 6, 2023), 477–502. https://doi.org/https://doi.org/10.1146/annurev-control-062722-100728

Chung, W., & Iagnemma, K. (2016, January). Wheeled robots [Publisher Copyright: © Springer-Verlag Berlin Heidelberg 2016.]. In *Springer handbook of robotics* (pp. 575–593). Springer International Publishing. https://doi.org/10.1007/978-3-319-32552-1_24

Cucuzza, J. (2021). The status and future of mining automation: An overview. *IEEE Industrial Electronics Magazine*, *15*(3), 6–12. https://doi.org/10.1109/MIE.2020.3039736

Darling, P., Society for Mining, M., & (U.S.), E. (2011). *Sme mining engineering handbook, third edition*. Society for Mining, Metallurgy, Exploration.

Dodge, H. D. (2020). Gemini case study. https://doi.org/10.2172/1616233

Dokuyucu, H. I., & Özmen, N. G. (2023). Achievements and future directions in self-reconfigurable modular robotic systems. *Journal of Field Robotics*, *40*(3), 701–746. https://doi.org/10.1002/rob.22139

Dorigo, M., Trianni, V., Sahin, E., Groß, R., Labella, T. H., Baldassarre, G., Nolfi, S., Mondada, F., Deneubourg, J.-L., Floreano, D., & Gambardella, L. M. (2004). Evolving self-organizing behaviors for a swarm-bot. *Autonomous Robots*, *17*(2-3), 223–245. https://doi.org/10.1023/B:AURO.0000033973.24945.f3

Dorigo, M., Tuci, E., Trianni, V., Groß, R., Nouyan, S., Ampatzis, C., Labella, T. H., O'Grady, R., Bonani, M., & Mondada, F. (2006). Swarm-bot: Design and implementation of colonies of self-assembling robots. In G. Y. Yen & D. B. Fogel (Eds.), *Computational intelligence: Principles and practice* (pp. 103–136). IEEE Computational Intelligence Society.

Ebadi, K., Bernreiter, L., Biggie, H., Catt, G., Chang, Y., Chatterjee, A., Denniston, C. E., Deschênes, S.-P., Harlow, K., Khattak, S., Nogueira, L., Palieri, M., Petráček, P., Petrlík, M., Reinke, A., Krátký, V., Zhao, S., Agha-mohammadi, A.-a., Alexis, K., . . . Carlone, L. (2024). Present and future of slam in extreme environments: The darpa subt challenge. *IEEE Transactions on Robotics*, *40*, 936–959. https://doi.org/10.1109/TRO.2023.3323938

Fan, D. D., Thakker, R., Bartlett, T., Miled, M. B., Kim, L., Theodorou, E., & Agha-mohammadi, A.-a. (2019). Autonomous hybrid ground/aerial mobility in unknown environments. *2019 IEEE/RSJ International Conference on Intelligent Robots and Systems (IROS)*, 3070–3077. https://doi.org/10.1109/IROS40897.2019.8968276

Forouhar, M., Čížek, P., & Faigl, J. (2021). Scarab ii: A small versatile six-legged walking robot. *5th Full-Day Workshop on Legged Robots at IEEE International Conference on Robotics and Automation (ICRA)*, 1–2.

Fujiwara, A., Nakatake, T., Tadami, N., Isaka, K., Yamada, Y., Sawada, H., Nakarnura, T., & Kubota, T. (2018). Development of both-ends supported flexible auger for lunar earthworm-type excavation robot leavo. *2018 IEEE/ASME International Conference on Advanced Intelligent Mechatronics (AIM)*, 924–929. https://doi.org/10.1109/AIM.2018.8452676

Fukuda, T., & Nakagawa, S. (1988). Approach to the dynamically reconfigurable robotic system. *Journal of Intelligent and Robotic Systems*, *1*, 55–72.

Gausemeier, J., & Moehringer, S. (2002). Vdi 2206- a new guideline for the design of mechatronic systems [2nd IFAC Conference on Mechatronic Systems, Berkeley, CA, USA, 9-11 December]. *IFAC Proceedings Volumes*, *35*(2), 785–790. https://doi.org/https://doi.org/10.1016/S1474-6670(17)34035-1

Gbadegeshin, S. A., Natsheh, A. A., Ghafel, K., Mohammed, O., Koskela, A., Rimpiläinen, A., Tikkanen, J., & Kuoppala, A. (2022). Overcoming the valley of death: A new model for high technology startups. *Sustainable Futures*, *4*, 100077. https://doi.org/https://doi.org/10.1016/j.sftr.2022.100077

George Thuruthel, T., Ansari, Y., Falotico, E., & Laschi, C. (2018). Control strategies for soft robotic manipulators: A survey [PMID: 29297756]. *Soft Robotics*, *5*(2), 149–163. https://doi.org/10.1089/soro.2017.0007

George Thuruthel, T., Falotico, E., Manti, M., Pratesi, A., Cianchetti, M., & Laschi, C. (2017). Learning closed loop kinematic controllers for continuum manipulators in unstructured environments [PMID: 29182085]. *Soft Robotics*, *4*(3), 285–296. https://doi.org/10.1089/soro.2016.0051

Gomez, V., Hernando, M., Aguado, E., Sanz, R., & Rossi, C. (2023, July). Robominer_tests. https://doi.org/10.5281/zenodo.8119182

Gomez, V., Walid, R., HERNANDO GUTIERREZ, M., Asko, R., & Claudio, R. (2023, December). Whisker_demo. https://doi.org/10.5281/zenodo.10447310

Grehl, S., Donner, M., Ferber, M., Dietze, A., Mischo, H., & Jung, B. (2015). Mining-rox–mobile robots in underground mining. *Proceedings of the Third International Future Mining Conference, Sydney, Australia*, 4–6.

Grohol, M., & Veeh, C. (2023). *Study on the critical raw materials for the eu*. https://ec.europa.eu/docsroom/documents/54114/attachments/1/translations/en/renditions/native

Gross, R., Bonani, M., Mondada, F., & Dorigo, M. (2006). Autonomous self-assembly in swarm-bots. *IEEE Transactions on Robotics*, *22*(6), 1115–1130. https://doi.org/10.1109/TRO.2006.882919

Guanghua, Z., Zhicheng, D., & Wei, W. (2006). Realization of a modular reconfigurable robot for rough terrain. *2006 International Conference on Mechatronics and Automation*, 289–294. https://doi.org/10.1109/ICMA.2006.257529

Hakonen, K., Friman, E., Salomaa, T., & Aaltonen, J. (2023). *Robominers deliverable 7.1: Robominer prototype* (tech. rep.). ROBOMINERS.

Hartman, H. L., & Mutmansky, J. M. (2002). *Introductory mining engineering* (2nd). John Wiley & Sons.

He, B., Ji, X., Li, G., & Cheng, B. (2024). Key technologies and applications of uavs in underground space: A review. *IEEE Transactions on Cognitive Communications and Networking*, 1–1. https://doi.org/10.1109/TCCN.2024.3358545

Héder, M. (2017). From nasa to eu: The evolution of the trl scale in public sector innovation. *THE INNOVATION JOURNAL*, *22*(2), 1–23.

Hernando, M., Bajo, D., Gomez, V., Aguado, E., & Rossi, C. (2022). *Sistema mecánico de actuación para un brazo robótico flexible* (Patent No. ES2907801).

Hirshorn, S., & Jefferies, S. (2016). *Final report of the nasa technology readiness assessment (tra) study team* (tech. rep.).

Hongyu, W., Zhang, Y., Zhang, T., Guan, Y., Xu, K., Ding, X., & PANG, Y. (2021). Review on bioinspired planetary regolith-burrowing robots. *Space Science Reviews*, *217*(8). https://doi.org/10.1007/s11214-021-00863-2

Hudson, N., Talbot, F., Cox, M., Williams, J., Hines, T., Pitt, A., Wood, B., Frousheger, D., Lo Surdo, K., Molnar, T., Steindl, R., Wildie, M., Sa, I., Kottege, N., Stepanas, K., Hernández, E., Catt, G., Docherty, W., Tidd, B., & Arkin, R. (2022). Heterogeneous ground and air platforms, homogeneous sensing: Team csiro data61's approach to the darpa subterranean challenge. *Field Robotics*, *2*, 595–636. https://doi.org/10.55417/fr.2022021

Hutter, M., Gehring, C., Jud, D., Lauber, A., Bellicoso, C. D., Tsounis, V., Hwangbo, J., Bodie, K., Fankhauser, P., Bloesch, M., Diethelm, R., Bachmann, S., Melzer, A., & Hoepflinger, M. (2016). Anymal - a highly mobile and dynamic quadrupedal robot. *2016 IEEE/RSJ International Conference on Intelligent Robots and Systems (IROS)*, 38–44. https://doi.org/10.1109/IROS.2016.7758092

International Organization for Standardization. (2013). *Space systems — Definition of the Technology Readiness Levels (TRLs) and their criteria of assessment* (tech. rep. No. ISO 16290:2013). International Organization for Standardization.

Isaka, K., Tsumura, K., Watanabe, T., Toyama, W., Sugesawa, M., Yamada, Y., Yoshida, H., & Nakamura, T. (2019). Development of underwater drilling robot based on earthworm locomotion. *IEEE Access*, *7*, 103127–103141. https://doi.org/10.1109/ACCESS.2019.2930994

Kalantari, A., Touma, T., Kim, L., Jitosho, R., Strickland, K., Lopez, B. T., & Agha-Mohammadi, A.-A. (2020). Drivocopter: A concept hybrid aerial/ground vehicle for long-endurance mobility. *2020 IEEE Aerospace Conference*, 1–10. https://doi.org/10.1109/AERO47225.2020.9172782

Kasprzyczak, L., Szwejkowski, P., & Cader, M. (2016). Robotics in mining exemplified by mobile inspection platform. *Mining–Informatics, Automation and Electrical Engineering*, *54*(2), 23–28.

Kasprzyczak, L., Trenszek, S., & Cader, M. (2012). Robot for monitoring hazardous environments as a mechatronic product. *Journal of Automation, Mobile Robotics and Intelligent Systems*, *6*(4), 57–64.

Kim, H., & Choi, Y. (2023). Development of autonomous driving patrol robot for improving underground mine safety. *Applied Sciences*, *13*(6). https://doi.org/10.3390/app13063717

Kotay, K., Rus, D., Vona, M., & McGray, C. (1998). The self-reconfiguring robotic molecule. *Proceedings. 1998 IEEE International Conference on Robotics and Automation*, *1*, 424–431 vol.1. https://doi.org/10.1109/ROBOT.1998.676452

Lee, J., Lim, H., Song, S., & Myung, H. (2019). Concept design for mole-like excavate robot and its localization method. *2019 7th International Conference on Robot Intelligence Technology and Applications (RiTA)*, 56–60. https://doi.org/10.1109/RITAPP.2019.8932732

Lee, J., Tirtawardhana, C., & Myung, H. (2020). Development and analysis of digging and soil removing mechanisms for mole-bot: Bio-inspired mole-like drilling robot. *2020 IEEE/RSJ International Conference on Intelligent Robots and Systems (IROS)*, 7792–7799. https://doi.org/10.1109/IROS45743.2020.9341230

Lee, J., Tirtawardhana, C., & Myung, H. (2023). Performance verification of biomimetic mole robot (mole-bot) for efficient underground exploration. In J. Jo, H.-L. Choi, M. Helbig, H. Oh, J. Hwangbo, C.-H. Lee, & B. Stantic (Eds.), *Robot intelligence technology and applications 7* (pp. 321–330). Springer International Publishing.

Li, D., Zhao, Y., Zhu, S., & Luan, H. (2019). A conceptual scale model of mobile drilling robot. *Assembly Automation*, *40*. https://doi.org/10.1108/AA-10-2018-0171

Li, H., Wang, H., Cui, L., Li, J., Wei, Q., & Xia, J. (2022). Design and experiments of a compact self-assembling mobile modular robot with joint actuation and onboard visual-based perception. *Applied Sciences*, *12*(6). https://doi.org/10.3390/app12063050

Li, Y., Li, M., Zhu, H., Hu, E., Tang, C., Li, P., & You, S. (2020). Development and applications of rescue robots for explosion accidents in coal mines. *Journal of Field Robotics*, *37*(3), 466–489. https://doi.org/https://doi.org/10.1002/rob.21920

Lin, M. A., Reyes, E., Bohg, J., & Cutkosky, M. R. (2022). Whisker-inspired tactile sensing for contact localization on robot manipulators. *2022 IEEE/RSJ International Conference on Intelligent Robots and Systems (IROS)*, 7817–7824. https://doi.org/10.1109/IROS47612.2022.9982122

Liu, J., Li, P., & Zuo, S. (2023). Actuation and design innovations in earthworm-inspired soft robots: A review. *Frontiers in Bioengineering and Biotechnology*, *11*. https://doi.org/10.3389/fbioe.2023.1088105

Liu, J., Zhang, X., & Hao, G. (2016). Survey on research and development of reconfigurable modular robots. *Advances in Mechanical Engineering*, *8*(8). https://doi.org/10.1177/1687814016659597

Lopes, L., Bodo, B., Rossi, C., Henley, S., Žibret, G., Kot-Niewiadomska, A., & Correia, V. (2020). Robominers – developing a bio-inspired modular robot-miner for difficult to access mineral deposits. *Advances in Geosciences*, *54*, 99–108. https://doi.org/10.5194/adgeo-54-99-2020

Maity, A., & Majumder, S. (2014). Design of an amphibian exploring robot. *IOP Conference Series: Materials Science and Engineering*, *65*(1), 012015. https://doi.org/10.1088/1757-899X/65/1/012015

Mallios, A., Ridao, P., Ribas, D., Carreras, M., & Camilli, R. (2016). Toward autonomous exploration in confined underwater environments. *Journal of Field Robotics*, *33*(7), 994–1012. https://doi.org/https://doi.org/10.1002/rob.21640

Marshall, J. A., Bonchis, A., Nebot, E., & Scheding, S. (2016). Robotics in mining. In B. Siciliano & O. Khatib (Eds.), *Springer handbook of robotics* (pp. 1549–1576). Springer International Publishing. https://doi.org/10.1007/978-3-319-32552-1_59

Martinez, B., Lima, R. R., Samarakoon, K., Rathjen, J., Gross, J. N., & Pereira, G. A. S. (2023). Oxpecker: A tethered uav for inspection of stone-mine pillars. *Drones*, *7*(2). https://doi.org/10.3390/drones7020073

Martins, A., Almeida, J., Almeida, C., Dias, A., Dias, N., Aaltonen, J., Heininen, A., Koskinen, K. T., Rossi, C., Dominguez, S., Vörös, C., Henley, S., McLoughlin, M., van Moerkerk, H., Tweedie, J., Bodo, B., Zajzon, N., & Silva, E. (2018). Ux 1 system design - a robotic system for underwater mining exploration. *2018 IEEE/RSJ International Conference on Intelligent Robots and Systems (IROS)*, 1494–1500. https://doi.org/10.1109/IROS.2018.8593999

Martins, A., Almeida, J., Almeida, C., Pereira, R., Sytnyk, D., Soares, E., Matias, B., Pereira, T., & Silva, E. (2020). Mara - a modular underwater robot for confined spaces exploration. *Global Oceans 2020: Singapore – U.S. Gulf Coast*, 1–6. https://doi.org/10.1109/IEEECONF38699.2020.9388981

Martz, J., Al-Sabban, W., & Smith, R. N. (2020). Survey of unmanned subterranean exploration, navigation, and localisation. *IET Cyber-Systems and Robotics*, *2*(1), 1–13. https://doi.org/https://doi.org/10.1049/iet-csr.2019.0043

Milford, M., Wyeth, G., & Prasser, D. (2004). Ratslam: A hippocampal model for simultaneous localization and mapping. *IEEE International Conference on Robotics and Automation, 2004. Proceedings. ICRA '04. 2004*, *1*, 403–408 Vol.1. https://doi.org/10.1109/ROBOT.2004.1307183

Molyneaux, L. (2016). *Development of an underground mine scout robot* [Master's thesis, Victoria University of Wellington]. https://doi.org/10.26686/wgtn.17019014.v1

Molyneaux, L., Carnegie, D. A., & Chitty, C. (2015). Hades: An underground mine disaster scouting robot. *2015 IEEE International Symposium on Safety, Security, and Rescue Robotics (SSRR)*, 1–6. https://doi.org/10.1109/SSRR.2015.7443019

Mondada, F., Pettinaro, G., Guignard, A., Kwee, I., Floreano, D., Deneubourg, J., Nolfi, S., Gambardella, L., & Dorigo, M. (2004). Swarm-bot: A new distributed robotic concept. *AUTONOMOUS ROBOTS*, *17*(2-3), 193–221. https://doi.org/10.1023/B:AURO.0000033972.50769.1c

Morris, A., Ferguson, D., Omohundro, Z., Bradley, D., Silver, D., Baker, C., Thayer, S., Whittaker, C., & Whittaker, W. (2006). Recent developments in subterranean robotics. *Journal of Field Robotics*, *23*(1), 35–57. https://doi.org/https://doi.org/10.1002/rob.20106

Moubarak, P., & Ben-Tzvi, P. (2012). Modular and reconfigurable mobile robotics. *Robotics and Autonomous Systems*, *60*(12), 1648–1663. https://doi.org/https://doi.org/10.1016/j.robot.2012.09.002

Murata, S., Yoshida, E., Kurokawa, H., Tomita, K., & Kokaji, S. (2001). Self-repairing mechanical systems. *Auton. Robots*, *10*, 7–21. https://doi.org/10.1023/A:1026540318188

Nakamura, T., Kato, T., Iwanaga, T., & Muranaka, Y. (2006). Peristaltic crawling robot based on the locomotion mechanism of earthworms [4th IFAC Symposium on Mechatronic Systems]. *IFAC Proceedings Volumes*, *39*(16), 139–144. https://doi.org/https://doi.org/10.3182/20060912-3-DE-2911.00027

Novák, P., Kot, T., Babjak, J., Konečný, Z., Moczulski, W., & Rodriguez López, Á. (2018). Implementation of explosion safety regulations in design of a mobile robot for coal mines. *Applied Sciences*, *8*(11). https://doi.org/10.3390/app8112300

Ohradzansky, M., Rush, E., Riley, D., Mills, A., Ahmad, S., McGuire, S., Biggie, H., Harlow, K., Miles, M., Frew, E., Heckman, C., & Humbert, J. (2022). Multi-agent autonomy: Advancements and challenges in subterranean exploration. *Field Robotics*, *2*, 1068–1104. https://doi.org/10.55417/fr.2022035

Park, T., Lewin, G., & Buffenstein, R. (2010). Naked mole rats: Their extraordinary sensory world. In M. D. Breed & J. Moore (Eds.), *Encyclopedia of animal behavior* (pp. 505–512). Academic Press. https://doi.org/10.1016/B978-0-08-045337-8.00152-2

Pearson, M. J., Fox, C., Sullivan, J. C., Prescott, T. J., Pipe, T., & Mitchinson, B. (2013). Simultaneous localisation and mapping on a multi-degree of freedom biomimetic whiskered robot. *2013 IEEE International Conference on Robotics and Automation*, 586–592. https://doi.org/10.1109/ICRA.2013.6630633

Pearson, M. J., Mitchinson, B., Sullivan, J. C., Pipe, A. G., & Prescott, T. J. (2011). Biomimetic vibrissal sensing for robots. *Philosophical Transactions of the Royal Society B: Biological Sciences*, *366*(1581), 3085–3096. https://doi.org/10.1098/rstb.2011.0164

Pearson, M. J., Mitchinson, B., Welsby, J., Pipe, T., & Prescott, T. J. (2010). Scratchbot: Active tactile sensing in a whiskered mobile robot. In S. Doncieux, B. Girard, A. Guillot, J. Hallam, J.-A. Meyer, & J.-B. Mouret (Eds.), *From animals to animats 11* (pp. 93–103). Springer Berlin Heidelberg.

Pearson, M. J., Pipe, A. G., Melhuish, C., Mitchinson, B., & Prescott, T. J. (2007). Whiskerbot: A robotic active touch system modeled on the rat whisker sensory system. *Adaptive Behavior*, *15*(3), 223–240. https://doi.org/10.1177/1059712307082089

Pearson, M. J., & Salman, M. (2019). Active whisker placement and exploration for rapid object recognition. *2019 IEEE/RSJ International Conference on Intelligent Robots and Systems (IROS)*, 672–677. https://doi.org/10.1109/IROS40897.2019.8968517

Piho, L., Gkliva, R., Remmas, W., Godon, S., Ristolainen, A., Burlet, C., Stasi, G., Hakonen, K., Gomez, V., Aguado, E., Milanov, M., van Moerkerk, H., Nikolov, K., Milosevic, Z., & Sanz, R. (2023). *Robominers deliverable 4.2: Report on perception, sensor-fusion software and navigation software* (tech. rep.). ROBOMINERS.

Pinkse, T., Quensel, R., John, S., Müller, B., Berner, M., Henley, S., Morrish, C., Tweedie, J., & Milanov, M. (2022). *Robominers deliverable 5.4: Mining analogues & upstream/downstream mining processes* (tech. rep.). ROBOMINERS.

Pinto, M. T., Žibret, G., Lopes, L., Bodo, B., & Zajzon, N. (2020). Unexup: Robot-based exploration technology for underground flooded mines. *Advances in Geosciences*, *54*, 109–117. https://doi.org/10.5194/adgeo-54-109-2020

Plotnikov, N. S., Kolokoltseva, E. U., & Volkova, Y. V. (2020). Technical review of robotic complexes for underground mining. *IOP Conference Series: Earth and Environmental Science*, *459*(4), 042025. https://doi.org/10.1088/1755-1315/459/4/042025

Prescott, T. J., Pearson, M. J., Mitchinson, B., Sullivan, J. W., & Pipe, A. G. (2009). Whisking with robots. *IEEE Robotics & Automation Magazine*, *16*(3), 42–50. https://doi.org/10.1109/MRA.2009.933624

Ralston, J. C., & Hainsworth, D. W. (1998). The numbat: A remotely controlled mine emergency response vehicle. In A. Zelinsky (Ed.), *Field and service robotics* (pp. 53–59). Springer London.

Ramezani, M., Khosoussi, K., Catt, G., Moghadam, P., Williams, J., Borges, P., Pauling, F., & Kottege, N. (2022). Wildcat: Online continuous-time 3d lidar-inertial slam.

Reddy, A. H., Kalyan, B., & Murthy, C. S. (2015). Mine rescue robot system – a review [Global Challenges, Policy Framework & Sustainable Development for Mining of Mineral and Fossil Energy Resources (GCPF:2015–20)]. *Procedia Earth and Planetary Science*, *11*, 457–462. https://doi.org/https://doi.org/10.1016/j.proeps.2015.06.045

Rogers, W. P., Kahraman, M. M., Drews, F. A., Powell, K., Haight, J. M., Wang, Y., Baxla, K., & Sobalkar, M. (2019). Automation in the mining industry: Review of technology, systems, human factors, and political risk. *Min. Metall. Explor.*, *36*, 607–631. https://doi.org/10.1007/s42461-019-0094-2

Rouček, T., Pecka, M., Čížek, P., Petříček, T., Bayer, J., Šalanský, V., Heřt, D., Petrlík, M., Báča, T., Spurný, V., Pomerleau, F., Kubelka, V., Faigl, J., Zimmermann, K., Saska, M., Svoboda, T., & Krajník, T. (2020a). Darpa subterranean challenge: Multi-robotic exploration of underground environments. In J. Mazal, A. Fagiolini, & P. Vasik (Eds.), *Modelling and simulation for autonomous systems* (pp. 274–290). Springer International Publishing.

Rouček, T., Pecka, M., Čížek, P., Petříček, T., Bayer, J., Šalanský, V., Heřt, D., Petrlík, M., Báča, T., Spurný, V., Pomerleau, F., Kubelka, V., Faigl, J., Zimmermann, K., Saska, M., Svoboda, T., & Krajník, T. (2020b). Darpa subterranean challenge: Multi-robotic exploration of underground environments. In J. Mazal, A. Fagiolini, & P. Vasik (Eds.), *Modelling and simulation for autonomous systems* (pp. 274–290). Springer International Publishing.

Saab, W., Racioppo, P., & Ben-Tzvi, P. (2019). A review of coupling mechanism designs for modular reconfigurable robots. *Robotica*, *37*(2), 378–403. https://doi.org/10.1017/S0263574718001066

Sadin, S. R., Povinelli, F. P., & Rosen, R. (1989). The nasa technology push towards future space mission systems. *Acta Astronautica*, *20*, 73–77. https://doi.org/https://doi.org/10.1016/0094-5765(89)90054-4

Salman, M., & Pearson, M. J. (2016a). Advancing whisker based navigation through the implementation of bio-inspired whisking strategies. *2016 IEEE International Conference on Robotics and Biomimetics (ROBIO)*, 767–773. https://doi.org/10.1109/ROBIO.2016.7866416

Salman, M., & Pearson, M. J. (2016b). Advancing whisker based navigation through the implementation of bio-inspired whisking strategies. *2016 IEEE International Conference on Robotics and Biomimetics (ROBIO)*, 767–773. https://doi.org/10.1109/ROBIO.2016.7866416

Salman, M., & Pearson, M. J. (2018). Whisker-ratslam applied to 6d object identification and spatial localisation. In V. Vouloutsi, J. Halloy, A. Mura, M. Mangan, N. Lepora, T. J. Prescott, & P. F. Verschure (Eds.), *Biomimetic and biohybrid systems* (pp. 403–414). Springer International Publishing.

Sayed, M. E., Roberts, J. O., Donaldson, K., Mahon, S. T., Iqbal, F., Li, B., Franco Aixela, S., Mastorakis, G., Jonasson, E. T., Nemitz, M. P., Bernardini, S., & Stokes, A. A. (2022). Modular robots for enabling operations in unstructured extreme environments. *Advanced Intelligent Systems*, *4*(5). https://doi.org/10.1002/aisy.202000227

Scherer, S. A., Agrawal, V., Best, G., Cao, C., Cujic, K., Darnley, R., DeBortoli, R., Dexheimer, E., Drozd, B., Garg, R., Higgins, I., Keller, J., Kohanbash, D., Nogueira, L., Pradhan, R., Tatum, M., Viswanathan, V. K., Willits, S. M., Zhao, S., … Travers, M. J. (2022). Resilient and modular subterranean exploration with a team of roving and flying robots. *Field Robotics*, *2*, 678–734. https://doi.org/10.55417/fr.2022023

Solomon, J. H., & Hartmann, M. J. Z. (2010). Extracting object contours with the sweep of a robotic whisker using torque information. *The International Journal of Robotics Research*, *29*(9), 1233–1245. https://doi.org/10.1177/0278364908104468

Stein, A., & Correia, V. (2023). *Robominers deliverable 10.8: Report of public outreach actions.* (tech. rep.). ROBOMINERS.

Steindl, R., Molnar, T., Talbot, F., Hudson, N., Tam, B., Murrell, S., & Kottege, N. (2020). Bruce – design and development of a dynamic hexapod robot.

Tatsch, C., Bredu, J. A., Covell, D., Tulu, I. B., & Gu, Y. (2023). Rhino: An autonomous robot for mapping underground mine environments. *2023 IEEE/ASME International Conference on Advanced Intelligent Mechatronics (AIM)*, 1166–1173. https://doi.org/10.1109/AIM46323.2023.10196202

Thrun, S., Thayer, S., Whittaker, W., Baker, C., Burgard, W., Ferguson, D., Hahnel, D., Montemerlo, D., Morris, A., Omohundro, Z., Reverte, C., & W, W. (2004). Autonomous exploration and mapping of abandoned mines. *IEEE Robotics & Automation Magazine*, *11*(4), 79–91. https://doi.org/10.1109/MRA.2004.1371614

Tomita, K., Murata, S., Kurokawa, H., Yoshida, E., & Kokaji, S. (1999). Self-assembly and self-repair method for a distributed mechanical system. *IEEE Transactions on Robotics and Automation*, *15*(6), 1035–1045. https://doi.org/10.1109/70.817668

Tranzatto, M., Mascarich, F., Bernreiter, L., Godinho, C., Camurri, M., Khattak, S., Dang, T., Reijgwart, V., Loeje, J., Wisth, D., Zimmermann, S., Nguyen, H., Fehr, M., Solanka, L., Buchanan, R., Bjelonic, M., Khedekar, N., Valceschini, M., Jenelten, F., … Alexis, K. (2022). Cerberus: Autonomous legged and aerial robotic exploration in the tunnel and urban circuits of the darpa subterranean challenge. *Field Robotics*, *2*, 274–324. https://doi.org/10.3929/ethz-b-000489726

Tranzatto, M., Miki, T., Dharmadhikari, M., Bernreiter, L., Kulkarni, M., Mascarich, F., Andersson, O., Khattak, S., Hutter, M., Siegwart, R., & Alexis, K. (2022). Cerberus in the darpa subterranean challenge. *Science Robotics*, *7*(66), eabp9742. https://doi.org/10.1126/scirobotics.abp9742

Ugenti, A., Galati, R., Mantriota, G., & Reina, G. (2023). Analysis of an all-terrain tracked robot with innovative suspension system. *Mechanism and Machine Theory*, *182*, 105237. https://doi.org/https://doi.org/10.1016/j.mechmachtheory.2023.105237

Universal Robots. (2023). Universal Robots ROS2 Driver.

Vartholomeos, P., Marantos, P., Karras, G., Menendez, E., Rodriguez, M., Martinez, S., & Balaguer, C. (2021). Modeling, gait sequence design, and control architecture of badger underground robot. *IEEE Robotics and Automation Letters*, *6*(2), 1160–1167. https://doi.org/10.1109/LRA.2021.3056068

Villarroel, J. L., Lera, F., Tardioli, D., Riazuelo, L., & Montano, L. (2024). Roboboat: A robotic boat for 3d mapping of partially flooded underground sites. *Journal of Field Robotics*, *n/a*(n/a). https://doi.org/https://doi.org/10.1002/rob.22303

Vu, L. A. T., Bi, Z., Mueller, D., & Younis, N. (2023). Modular self-configurable robots—the state of the art. *Actuators*, *12*(9). https://doi.org/10.3390/act12090361

Wang, W., Yu, W., & Zhang, H. (2010). Jl-2: A mobile multi-robot system with docking and manipulating capabilities. *International Journal of Advanced Robotic Systems*, *7*(1), 9. https://doi.org/10.5772/7256

Wang, W., Gao, W., Zhao, S., Cao, W., & Du, Z. (2017). Robot protection in the hazardous environments. In H. Canbolat (Ed.), *Robots operating in hazardous environments*. IntechOpen. https://doi.org/10.5772/intechopen.69619

Wang, Y., Tian, P., Zhou, Y., & Chen, Q. (2018). The encountered problems and solutions in the development of coal mine rescue robot. *Journal of Robotics*, *2018*, 1–11. https://doi.org/10.1155/2018/8471503

WATANABE, T., FUJIWARA, A., TADAMI, N., ISAKA, K., BARTHELEMY, M., OKUI, M., SAWADA, H., KUBOTA, T., & NAKAMURA, T. (2021). Development of front-actuation-type excavating unit for lunar excavating exploration robot "leavo". *TRANSACTIONS OF THE JAPAN SOCIETY FOR AERONAUTICAL AND SPACE SCIENCES, AEROSPACE TECHNOLOGY JAPAN*, *19*(2), 211–216. https://doi.org/10.2322/tastj.19.211

Wong, J., & Huang, W. (2006). “wheels vs. tracks” – a fundamental evaluation from the traction perspective. *Journal of Terramechanics*, *43*(1), 27–42. https://doi.org/https://doi.org/10.1016/j.jterra.2004.08.003

Xu, W., Chen, J., Lau, H. Y., & Ren, H. (2017). Data-driven methods towards learning the highly nonlinear inverse kinematics of tendon-driven surgical manipulators [e1774 RCS-16-0056.R1]. *The International Journal of Medical Robotics and Computer Assisted Surgery*, *13*(3), e1774. https://doi.org/https://doi.org/10.1002/rcs.1774

Yim, M., White, P., Park, M., & Sastra, J. (2009). Modular self-reconfigurable robots. In R. A. Meyers (Ed.), *Encyclopedia of complexity and systems science* (pp. 5618–5631). Springer New York. https://doi.org/10.1007/978-0-387-30440-3_334

Zajzon, N., Topa, B. A., Papp, R. Z., Aaltonen, J., Almeida, J. M., Almeida, C., Martins, A., Bodó, B., Henley, S., Pinto, M. T., & Žibret, G. (2023). Underwater measurements with ux robots; a new and available tool developed by unexup. *Advances in Geosciences*, *62*, 1–10. https://doi.org/10.5194/adgeo-62-1-2023

Zhang, C., Zhu, P., Lin, Y., Jiao, Z., & Zou, J. (2020). Modular soft robotics: Modular units, connection mechanisms, and applications. *Advanced Intelligent Systems*, *2*(6), 1900166. https://doi.org/https://doi.org/10.1002/aisy.201900166

Zhao, C., Zhang, S., Xie, T., & Zeng, L. (2022). A novel whisker sensor with variable detection range for object positioning. *Review of Scientific Instruments*, *93*(3), 035007. https://doi.org/10.1063/5.0080873

Zhao, J., Gao, J., Zhao, F., & Liu, Y. (2017). A search-and-rescue robot system for remotely sensing the underground coal mine environment. *Sensors*, *17*(10). https://doi.org/10.3390/s17102426